
Combined thickness and permittivity measurement of layers using an open-ended coaxial probe



Andreas Soto Peterson

*A thesis submitted for the degree of Master in Measurement
Technology and Instrumentation*

May 2018

**Department of Physics and Technology
Faculty of Mathematics and Natural Sciences**

“Essentially, all models are wrong, but some are useful”

George Box

Abstract

The purpose of this thesis is to develop a method for estimating both the thickness and permittivity of layers simultaneously utilizing an open-ended coaxial probe. One possible application of this method is the detection and characterization of deposits inside pipelines; examples are gas hydrate deposits in multiphase petroleum transportation. The hydrates forming can result in deposits on the interior surface of the piping and may restrict the flow of the production, it is thus necessary to monitor the layer thickness of the deposits to prevent any obstruction of flow, and the permittivity can tell us something about the composition of the deposits. The open-ended coaxial probe is a coaxial line that is a cut-off section of the transmission line. Permittivity measurements with the open-ended coaxial probe rely on analyzing the reflection of the electromagnetic wave from the probe-sample boundary. The open-ended coaxial probe is known to become radiating at high frequencies when the probe dimensions are comparable to the wavelength in the material under test. When measuring on samples with a finite thickness, this may result in additional reflections from the sample boundary interfering with the main reflection. If the applied permittivity model assumes an infinite thickness, the additional reflection may result in artifacts in the measured permittivity. Typically, this effect will be stronger at some frequencies due to resonance effects, which is seen as an unwanted measurement error. The resonance amplitude and frequency depend on the layer thickness, the permittivity of the layer/backing material and the probe dimensions. This thesis shows that by comparing the measured permittivity spectra with a matrix of finite element simulation, we can estimate both the layer thickness and material by comparing the measured data against the simulations. The simulations were verified by measuring liquids with known dielectric properties. The unwanted resonances manifest as artifacts in the permittivity spectra and increase the accuracy of the comparison. With the methods proposed in the thesis, we can also determine when the resonances occur for a given material, layer thickness, and frequency.

Acknowledgements

This thesis is written in collaboration with Christian Michelsen Research (CMR) and University of Bergen (UoB), Department of Physics and Technology, and was submitted for the M.Sc. degree in measurement technology and instrumentation.

I would first like to thank my co-supervisors Kjetil Folgerø at CMR and Bjørn Tore Hjertaker at UoB. The door to senior scientist Folgerø's office was always open whenever I had a question about my research or writing, and he pushed me in the right direction when needed. Moreover, Professor Hjertaker for giving me the support, the practical tools and software required to complete this thesis

I would also like to thank scientist Kjetil Haukalid and Jan Kocbach for sharing their knowledge, tools, equipment and clarifying discussions about dielectric spectroscopy.

Finally, I would like to thank my family and my dear Eldrid Gaukstad for motivating me and supporting me to finish this work. Without her, this thesis would not be possible.

Contents

Abstract	ii
Acknowledgements	iii
1 Introduction	1
1.1 Motivation	1
1.2 Background	1
1.3 Objective	3
1.4 Approach	3
1.5 Outline	4
2 Theory	5
2.1 Dielectric theory	5
2.1.1 Dielectric material and polarization	5
2.1.2 Permittivity and relaxation	6
2.1.3 Dielectric mechanisms	9
2.1.4 Debye equation	10
2.1.5 Cole-Cole equation and other distributions	11
2.2 Wave propagation and transmission line	12
2.2.1 Transmission line and reflection method	14
2.2.2 Loss-less transmission lines and special cases	16
2.2.3 Pure Travelling Wave	16
2.2.4 Pure Standing Wave	17
2.2.5 Mixed wave	17
2.3 Permittivity measurements	17
2.3.1 Non-resonant methods	18
2.3.2 Resonant methods	18
2.3.3 Vector network analyzer and scattering parameters	19
2.3.4 Error Correction Technique	21
2.3.5 Short, Open, Load and Thru (SOLT)	22
2.3.6 Open-ended coaxial probe	23
2.3.7 Equivalent circuit and bilinear calibration procedure	25

2.3.8	Resonance Frequency	26
2.3.9	Near-and far field	27
3	FE-modeling of sensor	29
3.1	Introduction to COMSOL®	30
3.1.1	Finite Element method	30
3.1.2	Boundary Conditions, Perfect Electric Conductor and Perfectly Matched Layer	31
3.1.3	Port	32
3.1.4	Impedance boundary condition	32
3.1.5	Mesh and Degrees of Freedom	33
3.1.6	Symmetry	34
3.2	COMSOL model of the experiment	35
3.2.1	Model geometry	35
3.2.2	Material	36
3.2.3	Boundary Conditions	38
3.2.4	Mesh	40
3.3	Simulation	43
4	Experiment	45
4.1	Experimental setup	45
4.1.1	Preparation of fluids	46
4.1.2	Reducing uncertainty of the experimental setup	48
4.2	Measurements	48
4.2.1	Measurement uncertainty of layer thickness	49
4.3	Interpolation	51
4.3.1	Conclusion	52
5	Results and discussion	54
5.1	Estimating material and layer thicknesses using FEM simulations	54
5.1.1	Comparison of permittivity (ϵ^*)	54
5.1.2	Comparison of reflection coefficient (S_{11})	58
5.1.3	ϵ^* and S_{11} comparison	62
5.1.4	Layer thicknesses larger than the probe sensitivity	65
5.2	Resonances	67
5.2.1	Simplified model of the reflection coefficient	71
5.2.2	Comparison of theoretical model vs simulation	72
5.3	Permittivity and depth limitations	76
5.3.1	Low-permittivity layers with water as backing material	80

5.3.2	Permittivity and depth limitations for ethanol/water mixtures	81
6	Summary and conclusions	86
6.1	Future work	88
6.1.1	Conductivity and salinity	88
6.1.2	Regarding level steps in contour plots	88
6.1.3	Limitation of the simulations	88
6.1.4	Other probe geometries	89
	References	90
A	Permittivity spectra	94
B	Paper	100

List of Figures

1.1	Illustration showing reflections from probe-layer boundary and layer-backing boundary.	2
2.1	Vector diagram of complex permittivity. Redrawn from [11].	8
2.2	Frequency response of dielectric mechanisms [11].	10
2.3	Debye model of distilled water at $T = 20^\circ C$, showing both the real and the imaginary part of the permittivity. Constants: $\epsilon_s = 80.21$, $\epsilon_\infty = 5.6$, $\tau = 9.36[ps]$ and $\sigma = 0$ [14].	11
2.4	Reflected and transmitted signal. Redrawn and modified from [11]. .	13
2.5	Transmission line with load.	15
2.6	Two-port network with forward and reverse traveling waves. Redrawn from [12, p. 121].	19
2.7	Open-ended coaxial probe as one-port network. Redrawn and modified from [7].	21
2.8	Two-port error model. Redrawn from [12][6].	22
2.9	Sketch of open-ended coaxial probe with effective depth sensitivity with a sample with a layer of permittivity ϵ_1 and backing material with permittivity ϵ_2	24
2.10	A open-ended probe connected with a test sample with backing layer.	25
2.11	Near-and far-field of antenna showing the different regions [30]. . . .	28
3.1	Two open-ended coaxial probes used in previous experiments [1]. . .	29
3.2	Modeling domain of an antenna in free space [35].	32
3.3	Block and layout information about geometrical model.	36
3.4	Cross-section view of the coaxial probe.	37
3.5	Transparent 3D visualization of the simulation from a 2D axisymmetric model, rotated from 0° to 270°	38
3.6	Boundary conditions of the simulations.	39
3.7	Magnitude of physics controlled mesh and user controlled mesh . . .	42
3.8	Phase of physics controlled mesh and user controlled mesh	42
3.9	Finalized tetrahedral mesh of the simulation model.	43
4.1	Model of experimental setup.	46

4.2	Photo of the experimental setup with the probe inserted in the center of the flange.	47
4.3	Steps of experimental procedure.	48
4.4	Spline interpolation method showing 55 simulated points fitted to 1001 experimental points for water with a layer thickness of $d = 50$ mm at $T = 20^{\circ}C$	52
4.5	Spline interpolation of magnitude and phase, showing 55 simulated points fitted to 1001 experimental points for water with a layer thickness of $d = 50mm$ at $T = 20^{\circ}C$	53
4.6	Spline interpolation method showing 1001 experimental points fitted to 54 simulation points for water with a layer thickness of $d = 40mm$ at $T = 20^{\circ}C$	53
5.1	Flowchart of the process for evaluating material and layer thickness using permittivity for comparison.	55
5.2	Comparison of simulation and experimental result of water with a layer thickness of 5mm and air as backing material.	57
5.3	Contour plot of experimental result of water with a layer thickness of 5mm and air as backing material with respect to simulations.	58
5.4	Flowchart of the process for evaluating material and layer thickness using the reflection coefficient for comparison.	59
5.5	Contour plot of experimental result of water with a layer thickness of 5mm and air as backing material with respect to simulations using S_{11}	61
5.6	Contour plot of experimental result of $\chi_e = 0.76$ with a layer thickness of 5mm and air as backing material with respect to simulations.	62
5.7	S_{11} and contour plot of experimental result of ethanol/water mixture, $\chi_e = 0.76$ with a layer thickness of 5mm and air as backing material with respect to simulations.	64
5.8	Contour plot of experimental result of water with a layer thickness of 13mm and air as backing material with respect to simulations.	65
5.9	Zoomed response from figure 5.8	66
5.10	Contour plot of experimental result of $\chi_e = 0.54$ with a layer thickness of 13mm and air as backing material with respect to simulations.	66
5.11	Simulated response of water and loss-less water ($\epsilon^* = 80.21$) with 12 mm layer thickness and air as backing material.	67
5.12	Permittivity and reflection coefficient for simulated mixtures of ethanol/water mixtures as layer and air as backing material.	69

5.13	Permittivity and reflection coefficient for simulated mixtures of ethanol/water mixtures as backing material and air as layer.	70
5.14	Simplified model of electromagnetic wave propagating in free space hitting a layer with thickness d and permittivity ϵ_1 , and a backing material of infinite length with permittivity ϵ_2	71
5.15	Theoretical model for reflection coefficient using the Debye relaxation model vs. simulation for a 5 mm water layer with air as backing material.	72
5.16	Theoretical model for reflection coefficient vs. simulation for a 5 mm loss-less water layer with air as backing material.	73
5.17	Theoretical model for reflection coefficient vs. simulation for a 5 mm loss-less medium layer with a complex permittivity of 20, and with air as backing material.	74
5.18	Theoretical model for reflection coefficient vs. simulation for a 5 mm loss-less layer with a complex permittivity of $80.21 - i20$, and with air as backing material.	75
5.19	Theoretical model for reflection coefficient vs. simulation for a 5 mm layer with a permittivity of $\epsilon^* = 20 - i5$, and with air as backing material.	75
5.20	Contour plot of the relative error, with $\epsilon^* = 10$ as layer and air as backing material with respect to layer thickness and frequency.	77
5.21	Contour plot of the relative error, with $\epsilon^* = 10$ to $\epsilon^* = 80$ as layer and air as backing material with respect to layer thickness.	78
5.22	Contour plot of the relative error with changed limits, with $\epsilon^* = 10$ to $\epsilon^* = 80$ as layer and air as backing material with respect to layer thickness.	79
5.23	Contour plot of the relative error, with $\epsilon^* = 10 - 5i$ to $\epsilon^* = 80 - 5i$ as layer and air as backing material with respect to layer thickness.	79
5.24	Contour plot of the relative error, with $\epsilon^* = 2$ to $\epsilon^* = 10$ as layer and water as backing material with respect to layer thickness.	80
5.25	Reference model, effective and simulated permittivity for a 1 mm thick layer with a molar fraction of $\chi_e = 0.54$, and with air as backing material.	82
5.26	Contour plot of the relative error, with different mole fractions of ethanol/water mixtures as layer and air as backing material with respect to layer thickness.	83

5.27	Reference model, effective. and simulated permittivity for a 50 mm thick layer with a molar fraction of $\chi_e = 0.22$, and with air as backing material.	84
5.28	Reference model, effective, and simulated permittivity for a 50 mm thick layer with water, and with air as backing material.	84
5.29	Corrected contour plot of the relative error, with different mole fractions of ethanol/water mixtures as layer and air as backing material with respect to layer thickness.	85
A.1	Real and imaginary permittivity of simulated ethanol/water mixture with mole fraction $\chi_e = 0$ and air as backing material	94
A.2	Real and imaginary permittivity of simulated ethanol/water mixture with mole fraction $\chi_e = 0.22$ and air as backing material	95
A.3	Real and imaginary permittivity of simulated ethanol/water mixture with mole fraction $\chi_e = 0.36$ and air as backing material	96
A.4	Real and imaginary permittivity of simulated ethanol/water mixture with mole fraction $\chi_e = 0.54$ and air as backing material	97
A.5	Real and imaginary permittivity of simulated ethanol/water mixture with mole fraction $\chi_e = 0.76$ and air as backing material	98
A.6	Real and imaginary permittivity of simulated ethanol/water mixture with mole fraction $\chi_e = 1.0$ and air as backing material	99

List of Tables

3.1	Comparison of an experiment versus a simulation environment [39]	34
3.2	Parameter expression used to designing the geometry.	37
3.3	Block definition of the geometry in the model.	38
3.4	Material definitions used in the model.	38
3.5	Default parameters of the physics controlled mesh of the simulation model	40
3.6	Dispersion step $\Delta\varepsilon$, high frequency permittivity ε_∞ , relaxation time τ and conductivity σ for different ethanol/water mixtures at different mole fractions χ_e of ethanol at temperature $T = 20^\circ C$	44
3.7	Different slab thicknesses for simulation purposes	44
4.1	Equipment and materials used	46
4.2	Dilution table for creating different ethanol/water mixtures.	47
4.3	Parameters set in the VNA	49
4.4	Equipment to used measure diameter and generate layer thicknesses of appropriate heights with rectangular and normalized uncertainties	50
5.1	Calibration fluids for transformation from reflection coefficient S_{11} to permittivity ε . for simulated and experimental data	56
5.2	Layer and backing material for simulations to map the the use-full range of the probe	76

List of Abbreviations

FEM	Finite Element Method
TE	Transverse Electric
TM	Transverse Magnetic
TEM	Transverse ElectroMagnetic
MUT	Material Under Test
FEA	Finite Element Analysis
PDE	Partial Differential Equations
VNA	Vector Network Analyzer
BST	Bilinear S-parameter Transformation
SOLT	Short Open Load Thru
PEC	Perfect Electric Conductor
PML	Perfectly Matched Layer
IBC	Impedance Boundary Condition
AMR	Adaptive Mesh Refinement
DOF	Degrees Of Freedom
BCP	Bilinear Calibration Procedure
RSD	Root Square Deviation

List of Symbols

ε_0	permittivity of vacuum
ε_s	static permittivity
$\Delta\varepsilon$	dispersion step
ε_∞	high frequency permittivity
ε'	Relative dielectric constant
ε''	Loss factor
ε^*	complex permittivity
ε_r^*	relative complex permittivity
ε_{eff}^*	effective permittivity
μ	permeability
τ	relaxation time
σ	conductivity
χ_e	electric susceptibility/ molar fraction ethanol/water mixture
ρ_b	bound charge density
σ_b	bound surface charge
$\hat{\mathbf{n}}$	normal vector
ρ	charge density
$\tan \delta$	loss tangent
P	polarization
E	electrical field
D	electrical displacement
H	magnetic field
B	magnetic flux density
J	current density
f	frequency
f_{ss}	frequency step size
f_{start}	start frequency
f_{stopp}	stopp frequency
$\#p$	number of stepped measurements
ω	angular frequency
α	attenuation constant/empirical constant

β	phase change coefficient
λ	wavelength
c	speed of light in vacuum
k	wave number
γ	propagation constant
θ_I	incident angle
θ_R	reflection angle
θ_T	transmitted angle
η	index of refraction
Z_0	transmission line impedance
Z_i	input impedance
Z_L	load impedance
V	voltage
V_i	incident voltage
V_r	reflected voltage
Γ	reflection coefficient
Γ_i	input reflection coefficient
Γ_L	load reflection coefficient
S_{11}, S_{22}	scattering reflection coefficients
S_{12}, S_{21}	scattering transmission coefficients
S_{11}^M	measurement plane reflection coefficient
S_{11}^R	reference plane reflection coefficient
E_{11}	directivity
E_{21}	forward reflection tracking
E_{12}	backward reflection tracking
E_{22}	source match
$\tilde{A}, \tilde{B}, \tilde{C}$	calibration coefficients
C	capacitance
L	inductance
Y	admittance
G	conductance
R	magnitude
θ	phase angle
$\tilde{\kappa}$	complex gain factor

In loving memory of Bjørn Terje Jakobsen

Chapter 1

Introduction

1.1 Motivation

The purpose of this thesis is to develop a method for estimating both the thickness and permittivity of layers simultaneously using an open-ended coaxial probe. One possible application of this method is the detection and characterization of deposits inside pipelines; examples are gas hydrate deposits in multiphase petroleum transportation [1][2]. Alternatively, during the production of oil and gas from a reservoir, formation water may be produced increasingly, as the natural pressure within the formation decreases. The decrease in temperature and pressure allow the solutes within the formation water to precipitate creating scale [3]. Both cases can result in deposits on the interior surface of the piping and may restrict the flow of the production, it is thus necessary to monitor the layer thickness of the deposits to prevent any obstruction of flow, and the permittivity can tell us something about the composition of the deposits.

1.2 Background

The dielectric properties of materials, namely permittivity, is a measure of the extent that the electrical distribution in the material can be distorted or polarized by an electrical field. The permittivity is normally given as a complex quantity, divided into a real and an imaginary part. The real part is a measure of how much energy from an external electric field is stored in a material and the imaginary part is a measure of how dissipative the material is to the field. Measuring the dielectric properties as a function of frequency is known as dielectric spectroscopy [4, p. 52]. There are several ways to perform dielectric spectroscopy, but open-ended sensors have proved to be a useful way to measure the dielectric properties of the materials

[5] and to estimate layer thickness in work done by Kjetil Folgerø [6]. The open-ended coaxial probe is a coaxial line that is a cut-off section of the transmission line. Permittivity measurements with the open-ended coaxial probe rely on analyzing the reflection of the electromagnetic wave from the probe-sample boundary. The open-ended coaxial probe is known to become radiating at high frequencies when the probe dimensions are comparable to the wavelength in the material under test. When measuring on samples with a finite thickness, this may result in additional reflections from the sample boundary interfering with the main reflection from the probe-sample boundary, as shown in figure 1.1. If the applied permittivity model assumes an infinite thickness, the additional reflection may result in artifacts in the measured permittivity. This effect will be stronger at some frequencies due to resonance effects. The amplitude of these resonances and the resonance frequency depends on the layer thickness, the permittivity of the layer and backing material, and the probe dimensions. The radiating properties of a coaxial probe have

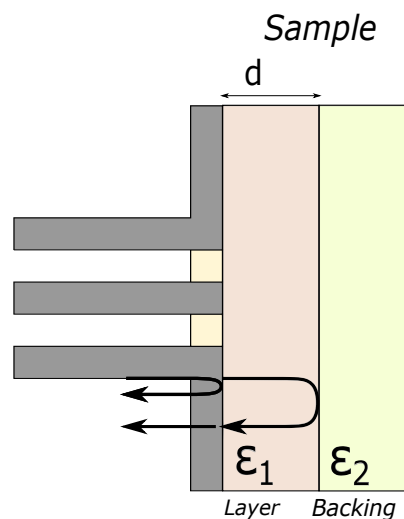


FIGURE 1.1: Illustration showing reflections from probe-layer boundary and layer-backing boundary.

been demonstrated for thickness measurements by comparing the experimental data with a matrix of finite element modeling (FEM) - simulations. Kjetil Haukalid briefly evaluated this method in his Ph.D. thesis [7], but it required additional work to be applicable. The work by Haukalid in his Ph.D. thesis and combined with previous work done by Folgerø resulted in a patent [8]. This thesis is a continuation of the work initiated by Haukalid and Folgerø, and therefore a result of several discussions regarding dielectric spectroscopy and methods of approach with people at CMR. The primary focus of this thesis has been on the radiating properties of

the probe and how to estimate both the material composition and thickness of the measurements conducted.

1.3 Objective

Usually, the layer thickness and permittivity estimation have a limited range when the probe is non-radiating, which means that only samples in close vicinity to the probe will affect the measured reflection coefficient and the measured permittivity at low frequencies. This also means that the permittivity of the back-layer does not influence the measured permittivity when the thickness of the layer is larger than the limited range [6]. The objective of this thesis is to investigate how to characterize layer thickness and permittivity simultaneously using simulations. It will also be investigated whether the useful information in the occurring resonances can be used to estimate thicker layers, which will extend the usefulness of the probe. Radiation from open-ended coaxial probes and subsequent reflections from layer boundaries can be studied analytically using full-wave electromagnetic models. However, such models typically assume an ideal representation of the measurement setup, which can lead to additional uncertainty in the estimated layer thickness. Analytic models taking the real measurement set-up into account typically becomes very complicated and are difficult to derive. By FEM, non-ideal measurement situations, e.g. mechanical sensor implementation can be taken into account. The validity of the simulations will be verified by measuring on liquids layer with known dielectric properties, to span out other materials and layer thicknesses.

1.4 Approach

The method presented in this thesis is based on a comparison of measured permittivity spectra with a matrix of FEM simulations. The FEM simulation software COMSOL Multiphysics has been used in this work. A two-dimensional axisymmetric model of an open-ended coaxial probe is used to build the simulation matrix. The simulation matrix spans the appropriate layer thickness, and layer permittivity ranges. The resonances occur in the GHz region for the specific probe. The density of the simulated frequencies must consequently be relatively high in this region as compared to the MHz region. After all the simulations are completed, the reflection coefficient matrix is transformed to a complex permittivity matrix using the bilinear calibration procedure. By using this data, it is possible to produce contour plots,

which indicates the uncertainty of the layer and material compared to the FEM simulation matrix. The permittivity and thickness of the layer is found by the best fit from the comparison.

1.5 Outline

The thesis begins with an introduction to the theory of dielectrics and then continues on wave propagation and transmission line theory, measurement, and error correction techniques. Chapter 3 presents the simulation environment and the necessary theory needed to simplify the simulations. In chapter 4 the experimental procedure is presented and with emphasis on how to reduce errors of the experimental data using the theory presented in chapter 2. The primary focus is on chapter 5, where the results when comparing the measured spectra are presented, along with limitations regarding material, layer and frequency of the specific probe. Chapter 6 summarizes the findings into a conclusion with suggestions for further work.

Chapter 2

Theory

2.1 Dielectric theory

2.1.1 Dielectric material and polarization

We usually categorize electromagnetic materials into conductors, semiconductors, and insulators, where the latter is commonly known as a dielectric material. We define a dielectric material as a material that will be polarized under the effect of an electric field. In contrast to conductors where charges can move freely through the material, all charges in a dielectric material are attached to specific atoms or molecules. The electric field can distort the charge distribution of a dielectric atom or molecule either by stretching or rotating. If the material consists of neutral atoms, the electric field will induce a tiny dipole moment in each atom, which will point in the same direction as the electric field. If the material consists of polar molecules, each permanent dipole will experience a torque that will line up along the direction of the field. Regardless of what the material consists of, the result will be the same. The dipoles will point along the direction of the field. If we assume we are working with linear dielectrics, where the polarization is proportional to the electric field, the polarization is given by

$$\mathbf{P} = \varepsilon_0 \chi_e \mathbf{E} \quad (2.1)$$

where ε_0 is the permittivity in vacuum, χ_e is the electric susceptibility and \mathbf{E} is the electric field. The electric susceptibility is also referred to as the constant of proportionality, which depends on factors like temperature and structure of the material. The effect of polarization is to produce accumulations of bound charges ρ_b within the dielectric, given by

$$\rho_b = -\nabla \cdot \mathbf{P} \quad (2.2)$$

and a bound surface charge σ_b given by

$$\sigma_b = \mathbf{P} \cdot \hat{\mathbf{n}} \quad (2.3)$$

Where $\hat{\mathbf{n}}$ is the unit normal vector. If we denote the charge due to all other factors as free charge ρ_f , the total charge density of the dielectric material is given by

$$\rho = \rho_b + \rho_f \quad (2.4)$$

From Gauss's law written on differential form, we have that:

$$\nabla \cdot \mathbf{E} = \frac{\rho}{\varepsilon_0} \Rightarrow \varepsilon_0 \nabla \cdot \mathbf{E} = \rho = \rho_b + \rho_f = -\nabla \cdot \mathbf{P} + \rho_f \quad (2.5)$$

Rewriting this expression gives

$$\nabla \cdot (\varepsilon_0 \mathbf{E} + \mathbf{P}) = \rho_f \quad (2.6)$$

where $\varepsilon_0 \mathbf{E} + \mathbf{P}$ is commonly known as the electrical displacement vector \mathbf{D}

$$\mathbf{D} = \varepsilon_0 \mathbf{E} + \mathbf{P} \quad (2.7)$$

which is the electrical field deduced directly from the free charge distribution. Rewriting equation (2.6) we get

$$\nabla \cdot \mathbf{D} = \rho_f \quad (2.8)$$

Combining equation (2.8) and equation (2.1) we obtain:

$$\mathbf{D} = \varepsilon_0 \mathbf{E} + \mathbf{P} = \varepsilon_0 \mathbf{E} + \varepsilon_0 \chi_e \mathbf{E} = \varepsilon_0 (\mathbf{1} + \chi_e) \mathbf{E} = \varepsilon \mathbf{E} \quad (2.9)$$

where

$$\varepsilon = \varepsilon_0 (\mathbf{1} + \chi_e) \quad (2.10)$$

is called the permittivity of the material, and the relative permittivity or dielectric constant is given by [9]

$$\varepsilon_r = \mathbf{1} + \chi_e = \frac{\varepsilon}{\varepsilon_0} \quad (2.11)$$

2.1.2 Permittivity and relaxation

The permittivity of a material is a measure of the extent to which the electrical charge distribution in the material can be distorted or polarized by an electrical

field [10, p. 8]. The electrical permittivity is normally given as a complex quantity

$$\varepsilon^* = \varepsilon' - j\varepsilon'' \quad (2.12)$$

where ε' and ε'' is the real and imaginary part of the complex permittivity respectively. This equation can also be rewritten using equation (2.11) which gives us the complex permittivity as a function of the relative permittivity

$$\varepsilon^* = \varepsilon_0 \cdot \varepsilon_r^* = \varepsilon_0 \cdot (\varepsilon_r' - j\varepsilon_r'') \quad (2.13)$$

To understand why the permittivity is complex, we can consider an alternating electric field, where the motions of the dipoles will be limited by the relaxation time τ . The relaxation time is a measure of the mobility of the dipoles which exist within a material. The movement of dipoles in an alternating electric field causes collisions and hence internal friction that is dissipated as heat. This results in the dipoles rotating slowly until they reach the final state of orientation polarization. Once we change the polarity of the electric field, the sequence is reversed. Thus, the dielectric loss is proportional to the frequency up to the relaxation frequency f_c , where the dipoles become unable to follow the alternating electric field. This coincides with the frequency where the dielectric loss is at its maximum, as seen in figure 2.2. Above the relaxation frequency both ε' and ε'' decreases as the electrical field alternates too fast to influence the dipole rotation and the orientation of the polarization disappears [4, p. 57] [10, p. 16-17]. The relaxation time is connected to relaxation frequency by [11]

$$\tau = \frac{1}{\omega_c} = \frac{1}{2\pi f_c} \quad (2.14)$$

Where ω_c is the angular relaxation frequency. The real part of the permittivity ε' is a measure of how much energy from an external electric field is stored in a material. The imaginary part of the permittivity is called the loss factor and is a measure of how dissipative a material is to an external electric field. The loss tangent is given by

$$\tan \delta = \frac{\varepsilon''}{\varepsilon'} \quad (2.15)$$

and the dielectric power factor is given by

$$\cos \theta = \frac{\varepsilon'}{\sqrt{(\varepsilon')^2 + (\varepsilon'')^2}} \quad (2.16)$$

This can easily be deduced by drawing the complex permittivity in a vector diagram, where we observe that the real and imaginary component are 90 degrees out

of phase. As illustrated below [11][12].

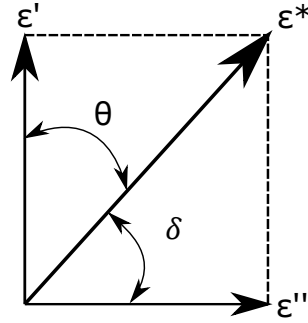


FIGURE 2.1: Vector diagram of complex permittivity. Redrawn from [11].

In order to understand the interactions between a material and electromagnetic fields on a macroscopic scale, Maxwell's equations can be used [9]

$$\nabla \cdot \mathbf{D} = \rho_f \quad (2.17)$$

$$\nabla \cdot \mathbf{B} = 0 \quad (2.18)$$

$$\nabla \times \mathbf{H} = \frac{\partial \mathbf{D}}{\partial t} + \mathbf{J}_f \quad (2.19)$$

$$\nabla \times \mathbf{E} = -\frac{\partial \mathbf{B}}{\partial t} \quad (2.20)$$

where \mathbf{H} is the magnetic field strength vector; \mathbf{E} , the electric field strength vector; \mathbf{B} , the magnetic flux density vector; \mathbf{D} , the electric displacement vector; \mathbf{J} , the current density vector and ρ , the charge density. Which has the following constitutive relations [12]

$$\mathbf{D} = \epsilon \mathbf{E} = (\epsilon' - j\epsilon'') \mathbf{E} \quad (2.21)$$

$$\mathbf{B} = \mu \mathbf{H} = (\mu' - j\mu'') \mathbf{H} \quad (2.22)$$

$$\mathbf{J} = \sigma \mathbf{E} \quad (2.23)$$

The constitutive parameters, the permittivity ϵ , permeability μ and conductivity σ are the parameters that explains the electromagnetic properties of a material. It is

important to note that the permittivity, permeability and conductivity are not static, and can change dynamically as a function of frequency, temperature orientation, mixture, pressure and molecular structure of the material. Rewriting equation (2.19) with equation (2.23) and (2.21), we obtain:

$$\nabla \times \mathbf{H} = \frac{\partial \mathbf{D}}{\partial t} + \mathbf{J} = \varepsilon \frac{\partial \mathbf{E}}{\partial t} + \sigma \mathbf{E} \quad (2.24)$$

Since the field is time dependent, i.e. $E = E_0 \cdot e^{j\omega t}$ so the equation can be further simplified into:

$$\nabla \times \mathbf{H} = (\sigma + j\omega\varepsilon) \mathbf{E} \quad (2.25)$$

and if we define the substitution:

$$\varepsilon \rightarrow \varepsilon - j\frac{\sigma}{\omega} \quad (2.26)$$

we get:

$$\nabla \times \mathbf{H} = j\omega \left(\varepsilon - j\frac{\sigma}{\omega} \right) \mathbf{E} \quad (2.27)$$

which concludes that the conductivity, which are due to contributions from ionic conduction, can be included in the complex permittivity and we get:

$$\varepsilon^* = \varepsilon' - j\varepsilon'' - j\frac{\sigma}{\omega\varepsilon_0} = \varepsilon' - j \left(\varepsilon'' - \frac{\sigma}{\omega\varepsilon_0} \right) \quad (2.28)$$

2.1.3 Dielectric mechanisms

The main dielectric mechanisms that are contributing to the permittivity of the material is ionic conduction, dipolar relaxation, atomic polarization and electric polarization. As stated in the previous section, the permittivity is frequency dependent, and in the low frequency ranges the permittivity is dominated by the slow mechanisms like ion conductivity and dipolar relaxation. At higher frequencies, atomic and electric polarization is prevalent. This can be illustrated by figure 2.2. It can also be seen that the loss factor ε'' has a peak at each critical frequency for the respective mechanics.

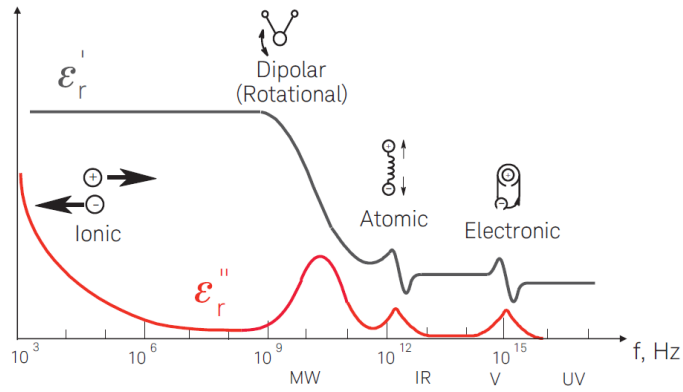


FIGURE 2.2: Frequency response of dielectric mechanisms [11].

2.1.4 Debye equation

According to Debye, the complex permittivity of a dielectric material due to dipolar and ionic relaxation can in most cases be expressed by [13]:

$$\varepsilon_r^* = \varepsilon_\infty + \frac{\varepsilon_s - \varepsilon_\infty}{1 + j\omega\tau} - j \frac{\sigma}{\omega\varepsilon_0} \quad (2.29)$$

where

$$\varepsilon_\infty = \lim_{\omega \rightarrow \infty} \varepsilon_r \quad (2.30)$$

$$\varepsilon_s = \lim_{\omega \rightarrow 0} \varepsilon_r \quad (2.31)$$

$$\Delta\varepsilon = \varepsilon_s - \varepsilon_\infty \quad (2.32)$$

where τ is the relaxation time, and ω is the angular frequency. From the Debye equation (2.29) we see that the relative permittivity at a given frequency is described by τ , ε_∞ , ε_s and σ . If we see the Debye equation in relation to figure 2.2 we see that for high frequencies the period of the alternating electrical field is much less than the relaxation time of the dipoles. Thus the dipoles are not influenced by the electric field and remain random. This implies that the permittivity at an high frequency, before atomic and electronic relaxation will be a finite positive value, which is ε_∞ . For low frequencies the relaxation process is able to keep up with the alternating field so that the polarization and the electric field has no phase difference. Thus ε_s also has a static positive value which decreases with increasing temperature due to increasing disorder [12]. The difference between ε_s and ε_∞ is known as the dispersion step $\Delta\varepsilon$. A plot showing the Debye model applied on distilled water is shown in figure 2.3.

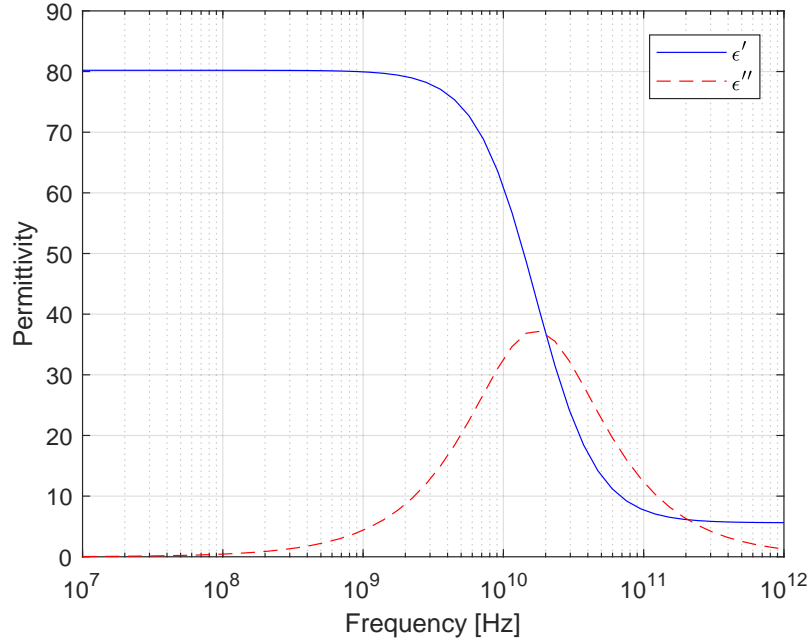


FIGURE 2.3: Debye model of distilled water at $T = 20^\circ\text{C}$, showing both the real and the imaginary part of the permittivity. Constants: $\varepsilon_s = 80.21$, $\varepsilon_\infty = 5.6$, $\tau = 9.36[\text{ps}]$ and $\sigma = 0$ [14].

2.1.5 Cole-Cole equation and other distributions

The Debye equation holds for materials with single relaxation time. If the material exhibits a distribution of relaxation times, several models have been proposed. Examples of these distributions are symmetrical distributions such as Frölich-Gevers, Wagner, Fuoss-Kirkwood and Cole-Cole, in addition to asymmetrical distributions such as Davidson-Cole and Havriliak-Negami [15]. The Cole brothers discovered that by introducing an empirical constant α to the Debye model, this could tell us something about the distribution of the relaxation times. Following, equation (2.29) can be written as [16]:

$$\varepsilon_r^* = \varepsilon_\infty + \frac{\varepsilon_s - \varepsilon_\infty}{1 + (j\omega\tau)^{1-\alpha}} - j \frac{\sigma}{\omega\varepsilon_0} \quad (2.33)$$

which is known as the Cole-Cole equation. The empirical constant α is in the range $0 \leq \alpha < 1$, and if $\alpha = 0$, we see that equation (2.33) is reduced to (2.29). Out of the different distribution functions, Cole-Cole is the most commonly used because the model is representative for a vast number and variety of dielectrics [17].

2.2 Wave propagation and transmission line

To understand how the electromagnetic waves propagate and resonate through a medium, transmission-line theory is needed. If we assume the wave is propagating in a linear media, where there is no free charge or no free current, $\mathbf{J}_f = 0$ and $\rho_f = 0$. Also, if we assume that the electrical field \mathbf{E} and magnetic field \mathbf{H} are sinusoidal waves that vary with time, we get

$$\begin{aligned}\mathbf{E} &= \hat{\mathbf{E}} \cdot e^{j\omega t} \\ \mathbf{H} &= \hat{\mathbf{H}} \cdot e^{j\omega t}\end{aligned}\quad (2.34)$$

and the wave equations for the electrical field \mathbf{E} and magnetic field \mathbf{H} is given by [9]

$$\nabla^2 \mathbf{E} + k^2 \mathbf{E} = 0 \quad (2.35)$$

$$\nabla^2 \mathbf{H} + k^2 \mathbf{H} = 0 \quad (2.36)$$

with the following relationship

$$k = \omega \sqrt{\varepsilon \mu} = \frac{2\pi}{\lambda} \Rightarrow k^2 = \omega^2 \varepsilon \mu \quad (2.37)$$

where k is the wave number and λ is the wavelength. The wave equation of the electrical field is of special relevance in this project. Normally in the transmission structure we decompose the electromagnetic field into transverse and axial components, i.e.

$$\mathbf{E} = \mathbf{E}_T + \mathbf{E}_z \quad (2.38)$$

$$\mathbf{H} = \mathbf{H}_T + \mathbf{H}_z \quad (2.39)$$

We have three types of electromagnetic waves with special E_z and H_z [12, p. 43]. If $E_z = 0$, the electromagnetic wave is called a transverse electric (TE) wave. If $H_z = 0$ the wave is called a transverse magnetic (TM) wave. Finally, if both $E_z = 0$ and $H_z = 0$, the wave is called a transverse electromagnetic (TEM) wave. If we solve the wave equation for an electric field propagating in the z -direction, and with an E -field parallel to the x -axis we get

$$\frac{\partial^2 \hat{E}_x}{\partial z^2} + \omega^2 \varepsilon \mu \hat{E}_x = 0 \quad (2.40)$$

which has the following general solution

$$\hat{E}_x = A \cdot e^{-\gamma z} + B \cdot e^{\gamma z} \quad (2.41)$$

where A and B complex numbers depending on the boundary conditions of the problem and γ is known as the propagation constant, defined by [12, p. 10]

$$\begin{aligned} \gamma &= jk \\ \gamma &= j\omega\sqrt{\varepsilon\mu} \\ \gamma &= j\frac{\omega}{c}\sqrt{\varepsilon' - j\varepsilon''} \\ \gamma &= \alpha + j\beta \end{aligned} \quad (2.42)$$

Using this result the forward travelling wave can be written as

$$\hat{E}_x = E_0 e^{-(\alpha + j\beta)x} e^{i\omega t} = E_0 e^{i(\omega t - \beta x)} e^{-\alpha x} \quad (2.43)$$

where α is the attenuation coefficient, $\beta = \frac{2\pi}{\lambda}$ is the phase change coefficient, λ is the operating wavelength in the medium and $c = \sqrt{\frac{1}{\varepsilon_0\mu_0}}$ is the velocity of light in vacuum. Attenuation is a fundamental property when it comes to wave propagation, and it contains information on how much the amplitude has decreased while propagating through the medium. This effect is mostly due to absorption and dispersion [9, p. 417-419] and can be illustrated by figure 2.4.

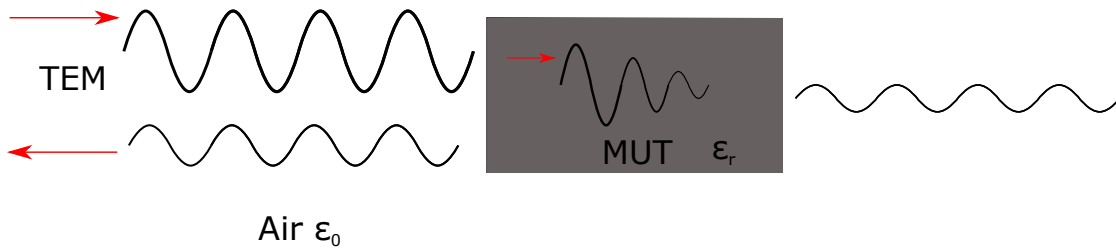


FIGURE 2.4: Reflected and transmitted signal. Redrawn and modified from [11].

Figure 2.4 shows a TEM wave propagating in air entering a material under test (MUT) with relative permittivity ε_r . From the figure, we see the wavelength decreases, the velocity decreases and the magnitude is attenuated. It can also be seen that some waves are transmitted through the material, whereas some are reflected between the boundaries of the material and air. Electromagnetic waves follow the three fundamental laws of geometrical optics [9]

1. The incident, reflected and transmitted wave vectors forms a plane (called the plane of incidence).
2. The angle of the incidence wave is equal to the angle of reflection:

$$\theta_I = \theta_R \quad (2.44)$$

3. The transmitted angle is given by (also known as Snell's law):

$$\frac{\sin(\theta_I)}{\sin(\theta_T)} = \frac{\eta_1}{\eta_2} \quad (2.45)$$

where

$$\eta = \sqrt{\frac{\varepsilon\mu}{\varepsilon_0\mu_0}} \quad (2.46)$$

which is known as the index of refraction of the material. For most materials, μ is very close to μ_0 . We can therefore simplify the expression as

$$\eta \cong \sqrt{\varepsilon_r} \quad (2.47)$$

Since ε_r is always greater than 1, light travels slower through matter, which can be seen by figure 2.4.

2.2.1 Transmission line and reflection method

Transmission line theory is a fundamental part of understanding how to measure the reflection coefficient. To understand this, consider an arbitrary transmission line with impedance Z_0 terminated in load with impedance Z_L with a voltage wave propagating in the $+z$ and $-z$ direction, as illustrated by figure 2.5. The so-called telegrapher equations show that propagation equation for the voltage is given by [12]

$$\frac{\partial^2 V}{\partial z^2} = \gamma^2 V \quad (2.48)$$

This equation has the same general solution as equation (2.41). The general solution implies that the voltage is the sum of a forward traveling wave and a backward traveling wave:

$$V = A \cdot e^{-\gamma z} + B \cdot e^{\gamma z} = V_i \cdot e^{-\gamma z} + V_r e^{\gamma z} \quad (2.49)$$



FIGURE 2.5: Transmission line with load.

Where V_i is the incident voltage and V_r is the reflected voltage wave of the voltage source. Analyzing the reflection properties of figure 2.5, the positive direction from the load to the generator is chosen such the voltage reflection coefficient is given by the reflected voltage V_r and the incident voltage V_i

$$\Gamma_L = \frac{V_r}{V_i} \quad (2.50)$$

and the relationship between the voltage and the current is determined by the loading impedance, so we have

$$Z_L = \frac{V_L}{I_L} = Z_0 \frac{V_i + V_r}{V_i - V_r} = Z_0 \frac{1 + \frac{V_r}{V_i}}{1 - \frac{V_r}{V_i}} = Z_0 \frac{1 + \Gamma_L}{1 - \Gamma_L} \quad (2.51)$$

Similarly, we could also define the reflection coefficient by the characteristic impedance of the transmission line and the impedance of the load:

$$\Gamma_L = \frac{Z_L - Z_0}{Z_L + Z_0} \quad (2.52)$$

If we consider a transmission line with length l connected to a load, we have the following relation [12]

$$V(l) = V_i e^{\gamma l} + V_r e^{-\gamma l} \quad (2.53)$$

$$I(l) = \frac{1}{Z_0} (V_i e^{\gamma l} - V_r e^{-\gamma l}) \quad (2.54)$$

$$Z_i(l) = \frac{V(l)}{I(l)} = Z_0 \frac{V_i e^{\gamma l} + V_r e^{-\gamma l}}{V_i e^{\gamma l} - V_r e^{-\gamma l}} = Z_0 \frac{1 + \Gamma_L e^{-2\gamma l}}{1 - \Gamma_L e^{-2\gamma l}} \quad (2.55)$$

which also implies that the input reflection coefficient is given by

$$\Gamma_i = \frac{Z_i - Z_0}{Z_i + Z_0} \Rightarrow \Gamma_i = \Gamma_L e^{-2\gamma l} \quad (2.56)$$

2.2.2 Loss-less transmission lines and special cases

From the definition of the hyperbolic tangent we have that

$$\tanh(x) = \frac{e^x + e^{-x}}{e^x - e^{-x}} \Rightarrow \tanh(\gamma l) = \frac{e^{\gamma l} + e^{-\gamma l}}{e^{\gamma l} - e^{-\gamma l}} \quad (2.57)$$

Following, we can rewrite equation (2.55) including the result from equation (2.52)

$$Z_i(l) = Z_0 \frac{Z_L + Z_0 \tanh(\gamma l)}{Z_0 + Z_L \tanh(\gamma l)} \quad (2.58)$$

If we are using a lossless transmission line, the propagation constant (equation (2.42)) becomes purely imaginary, i.e. :

$$\gamma = j\beta \quad (2.59)$$

This implies that the wave will not be attenuated and only the phase of the reflection coefficient (Γ_i) will change. Following, we can write Γ_i and Z_i as

$$\Gamma_i = \Gamma_L e^{-j2\beta l} \quad (2.60)$$

$$Z_i(l) = Z_0 \frac{Z_L + jZ_0 \tan(\beta l)}{Z_0 + jZ_L \tan(\beta l)} \quad (2.61)$$

2.2.3 Pure Travelling Wave

From equation (2.61) we see that if $\beta l = n\pi$, where $n \in \mathbb{Z}$, the expression will be reduced to $Z_i = Z_L$. In this state there is no reflection $\Gamma = 0$. Using the definition of the phase constant $\beta = \frac{2\pi}{\lambda}$, we can solve equation (2.61) for the length of the transmission line l

$$\frac{2\pi}{\lambda} l = n\pi \Rightarrow l = n \frac{\lambda}{2} \quad (2.62)$$

This implies that if the travelling length is any multiple of $n\frac{\lambda}{2}$ this will result in maximum transmission and minimum reflection, i.e. a pure travelling wave. In this case the input impedance will equal the load impedance

$$Z_i = Z_L \quad (2.63)$$

2.2.4 Pure Standing Wave

In the case of a pure standing wave the transmission line does not absorb any energy and all the energy is reflected: $|\Gamma_L| = 1$. This happens when $\beta l \rightarrow \frac{\pi}{2}$. Solving for the length l we get.

$$\frac{2\pi}{\lambda}l = \frac{\pi}{2} + n\pi \Rightarrow l = \frac{\lambda}{4} + n\frac{\lambda}{2} \quad (2.64)$$

Where $n \in \mathbb{Z}$, in this case equation (2.61) is reduced to:

$$Z_i = Z_0 \frac{jZ_0}{jZ_L} = \frac{Z_0^2}{Z_L} \quad (2.65)$$

If the travelling length is one quarter wavelength long, or a quarter wave length plus any multiple of n times half a wavelength, the transmission line is in pure standing-wave state. This is also known as quarter-wave resonance and can also occur when the load is short $Z_L = 0$ and when the load is open $Z_L = \infty$ [12, p. 48].

2.2.5 Mixed wave

In most cases when dealing with transmission lines, some of the energy is absorbed by the load whereas some is reflected. When the electromagnetic wave is in this state the wave is between the two extremities, i.e. a pure travelling wave and a pure standing wave.

2.3 Permittivity measurements

The methods for material characterization generally fall into non-resonant methods and resonant methods. Non-resonant methods are typically used to obtain

knowledge of the electromagnetic properties over a frequency range while resonant methods are used to obtain information at one or more specific frequencies. These methods can either be used separately or in combination. There are several practical factors to consider when choosing a method such as accuracy, cost, practical implementation and time. Typically the accuracy is higher for resonant methods than non-resonant methods.

2.3.1 Non-resonant methods

In non-resonant methods, the electromagnetic properties of materials are deduced from their impedance and the wave velocities in the materials over a wide frequency range. As discussed previously, electromagnetic waves follow the laws of geometrical optics. Therefore, when the wave propagates from one boundary to another, both the impedance and velocity of the wave change. This results in partial reflection from the interface between the two materials. By measuring the transmission and reflection of the interface, it can be acquired information about the dielectric properties of the two materials. Non-resonant methods are therefore further divided into reflection, transmission or a combination of reflection and transmission.

2.3.2 Resonant methods

As mentioned previously, resonant methods have higher accuracy compared to non-resonant methods, and is also more suitable for low-loss samples. In addition to only being able to measure at single or several discrete frequencies, they also have higher sensitivity than the non-resonant methods. The most common resonant methods include the resonator method and the resonant-perturbation (resonance-shift) method. In a resonator method the MUT serves as a resonator, i.e. the material will naturally oscillate at some frequencies with increased amplitude. And the properties of the sample are determined from the fact that a resonator will have different resonance frequency and quality factor depending on the permittivity and permeability of the sample. The quality factor is a dimensionless quantity which indicates the degree of damping in a resonator [18]. In the resonant-perturbation method, the sample is inserted into the part of the resonator where the electric field is largest. The properties of the sample are then calculated from the changes in quality factor and resonance frequency that is caused by inserting the sample.

2.3.3 Vector network analyzer and scattering parameters

A vector network analyzer (VNA) is a tool for measuring the amplitudes and phases of transmission and reflection coefficient of an analog circuit. A network analyzer mainly consists of a source, signal separation devices, and detectors [12]. The source launches a signal at a single frequency to the MUT. The receiver is tuned to the specific frequency to detect the reflected and transmitted signals from the material. The source is then stepped to the next frequency, and the measurement is repeated up to the specific frequency span that is set. And finally the data is presented as a function of frequency [11]. Normally when you use a VNA, you specify the number of stepped measurements over a selected frequency range. Therefore, depending on the frequency step and the selected measurement bandwidth, information can be missed during a sweep. It is important to ensure that there is sufficient overlap so that the all the information in the frequency range of the sweep are captured. The frequency step size is given by the following formula [19]:

$$f_{ss} = \frac{f_{stop} - f_{start}}{\#p - 1} \quad (2.66)$$

Where f_{ss} is the frequency step size, f_{stop} is the last frequency of the sweep, f_{start} is the first frequency of the sweep and $\#p$ is the number of stepped measurements respectively. If we consider a two-port network, the network analyzer can measure the four waves independently, i.e. two forward moving waves a_1 and a_2 and two reverse traveling waves b_1 and b_2 . This is illustrated in figure 2.6.

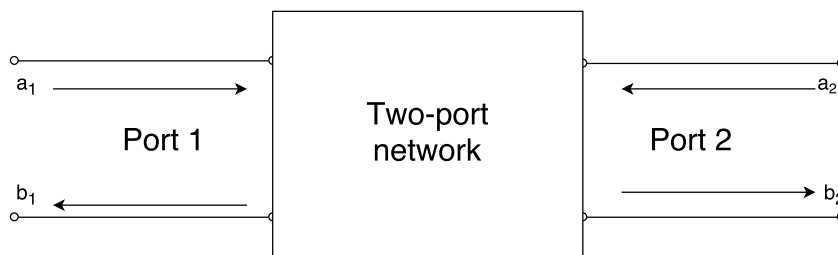


FIGURE 2.6: Two-port network with forward and reverse traveling waves. Redrawn from [12, p. 121].

If we assume that we have a loss-less and dispersion-less transmission line with a known characteristic impedance, we can describe the two-port network by a set of scattering parameters known as S-parameters. The S-parameters relate the incident and the reflected voltage waves. The scattering parameters for two-port network is

given by the following linear equations [20]:

$$b_1 = S_{11}a_1 + S_{12}a_2 \quad (2.67)$$

$$b_2 = S_{21}a_1 + S_{22}a_2 \quad (2.68)$$

The example with a two-port network can be extended to a multi-port network, by increasing the dimensions of the reflected, transmitted wave and scattering parameters matrices, which can be written as:

$$\begin{bmatrix} b_1 \\ b_2 \\ \vdots \end{bmatrix} = \begin{bmatrix} S_{11} & S_{12} & \vdots \\ S_{21} & S_{22} & \\ \vdots & & \ddots \end{bmatrix} \begin{bmatrix} a_1 \\ a_2 \\ \vdots \end{bmatrix} \quad (2.69)$$

S_{11} and S_{22} are regarded as the scattering reflection coefficients, whereas S_{12} and S_{21} are the scattering transmission coefficient of the network. Since the VNA gives us the amplitudes and phases of the scattering parameters, the parameters are complex, i.e. on the form $a + jb$. In general if $a_i = 0$ ($i \neq j$), we have that [12]:

$$S_{jj} = \frac{b_j}{a_j} \quad (j = 1, 2) \quad (2.70)$$

$$S_{ij} = \frac{b_i}{a_j} \quad (i \neq j; i = 1, 2; j = 1, 2) \quad (2.71)$$

In other words, if a port j is connected to a source and the other port is connected to a matching load with the same characteristic impedance as the transmission line, the reflection coefficient at port j is equal to S_{jj} :

$$\Gamma_j = S_{jj} = \frac{b_j}{a_j} \quad (2.72)$$

In this thesis an open-ended coaxial probe based on the reflection method is used together with the broad-band frequency method. The open-ended coaxial probe is well known for determining dielectric properties of materials, since the reflection coefficient depends on the material being tested [21][22]. However, this method is also very prone to measurement errors caused by e.g. the influence of air gaps, especially in the case of high-permittivity dielectrics [23]. This is due to the fact that the larger the impedance difference of the materials, the greater the modulation as can be seen by equation (2.52).

2.3.4 Error Correction Technique

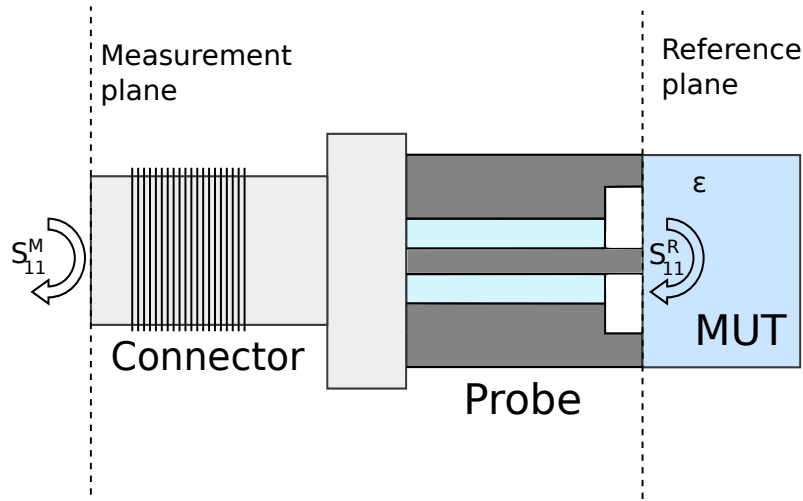


FIGURE 2.7: Open-ended coaxial probe as one-port network. Redrawn and modified from [7].

The measurements errors of a VNA usually fall into three categories: Measurement error, random error, and drift errors. Systematic error affect the system at all times. Therefore errors like directivity, port match, crosstalk and frequency response can be characterized through calibration. Random error are by definition unpredictable but can be limited through averaging and multiple measurements. Drift errors can be reduced by keeping the working conditions of the measurement system as close to the calibration conditions as possible. Temperature conditions are one of the main sources of drift error in dielectric spectroscopy, and instrumentation noise can be reduced by giving the electronic equipment sufficient time to stabilize. The temperature can also cause drift in the permittivity of the material being tested since permittivity has a temperature dependency. For an experimental setup, the VNA is calibrated with reference to the end of the coaxial cable as seen in figure 2.7. However, the measurements are performed at the end of the probe i.e., the reference plane. The difference between the measurement and reference plane leads to a phase lag between the two, and the measurement plane S-parameters can be given by a reference plane rotation [24]:

$$S_{11}^R = S_{11}^M e^{2\gamma l} \quad (2.73)$$

where γ is the propagation constant and l is the distance between the measurement plane and the reference plane. The simulations presented in chapter 3 are also influenced by the phase lag since the simulation was done at the reference plane. equation (2.73) assumes that there is no mismatch between the connector and the

probe. To account for this, a two-port error network can be used, as is shown in figure 2.8.

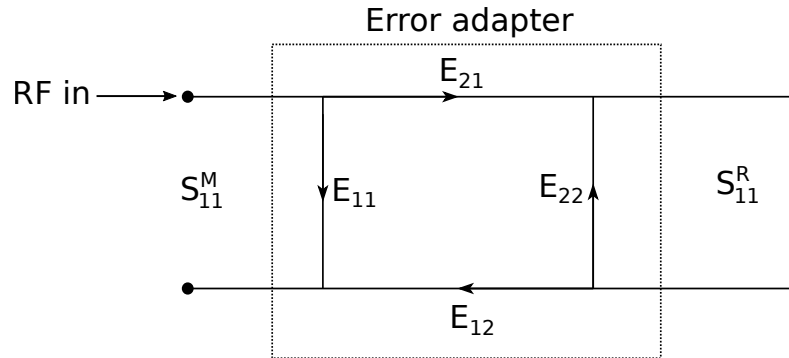


FIGURE 2.8: Two-port error model. Redrawn from [12][6].

where S_{11}^R and S_{11}^M are the reference and measurement plane reflection coefficient and E_{21} is the forward reflection tracking, E_{12} , the backward reflection tracking, E_{11} the directivity and E_{22} the source match. From the two-port error model in figure 2.74, we can find the reference plane reflection coefficient S_{11}^R from the measurement plane reflection coefficient S_{11}^M by the following equation:

$$S_{11}^R = \frac{S_{11}^M - E_{11}}{E_{22}S_{11}^M - (E_{11}E_{22} - E_{12}E_{21})} \quad (2.74)$$

equation (2.74) can be written as:

$$S_{11}^R = \frac{\tilde{A}S_{11}^M + \tilde{B}}{\tilde{C}S_{11}^M + 1} \quad (2.75)$$

where the complex frequency dependent coefficients \tilde{A} , \tilde{B} and \tilde{C} is found from S -parameter measurements of three calibration fluids with known permittivities, this equation is also known as the bilinear S -parameter transformation (BST) [25].

2.3.5 Short, Open, Load and Thru (SOLT)

To account for the systematic error parameters shown in figure 2.8, the SOLT calibration procedure introduced by Hewlett-Packard in 1978 is used [26]. The load calibration accounts for the directivity term (E_{11}), the open and short for the source match and reflection tracking (E_{22} , E_{12} and E_{21}) and the thru calibration is primarily for the tracking and load match. For 1-port VNAs, the thru calibration is discarded. The calibration parameters for the different calibration standards is defined by:

- **Short** - Transmission line length, transmission loss and frequency-dependent inductance given by:

$$L = L_0 + L_1 \cdot f + L_2 \cdot f^2 + L_3 \cdot f^3 \quad (2.76)$$

- **Open** - Transmission line length, transmission and frequency-dependent conductance given by:

$$C = C_0 + C_1 \cdot f + C_2 \cdot f^2 + C_3 \cdot f^3 \quad (2.77)$$

- **Load** - The load value is the same value as the characteristic impedance of source, e.g. 50Ω typically for coaxial lines. Load is in some literature referred to as match.
- **Thru** - Transmission line length and transmission loss.

In addition the frequency range of the calibration kit must be given for each calibration. As shown in figure 2.7, the calibration is done at the end of the measurement plane. Any additional connectors between the measurement plane and the reference plane will increase the phase shift due to internal reflections in the connector and probe.

2.3.6 Open-ended coaxial probe

The coaxial line has many advantages over the different types of transmission lines and is a widely used method for characterization of material properties [22]. The main advantages of using an open-ended coaxial probe can be summarized as:

- Wide working frequency range.
- Little or none sample preparation.
- Can be used in a temperature controlled environment.
- Works on both high and low-loss samples.

And the following disadvantages:

- The need for calibration and calibration fluids for permittivity calculations.
- Requires good contact between the coaxial aperture and the sample surface.

The open-ended coaxial probe is a coaxial line that is a cut-off section of the transmission line. The electromagnetic field propagates into the MUT, and the reflection signal (S_{11}) can be measured. The coaxial probe is categorized as a non-resonant reflection method (see section 2.3). A sketch of an open-ended coaxial probe propagating into a sample with a layer with thickness d and with a permittivity ϵ_1 and backing material with a permittivity of ϵ_2 is shown in figure 2.9. The probe design is generic because different measurement probes are often specially designed for the measurement requirements needed [27]. The real probe has some impedance customization, to better the impedance match within the probe that is not shown in this thesis. The open-ended probe has a restricted sensitivity depth when the probe is non-radiating. This implies that only samples close to the termination of the probe affects the measured reflection coefficient and layers greater than the probe sensitivity is considered infinitely thick. In other words, this means that the backing-layer will not influence the measured permittivity if the layer is thicker than the sensitivity depth. This critical sensitivity depth has been found to be approximately equal to the outer radius of the probe [28]. The critical sensitivity depth d_{crit} is defined as the layer thickness where the backing material does not affect the effective permittivity of the two layers.

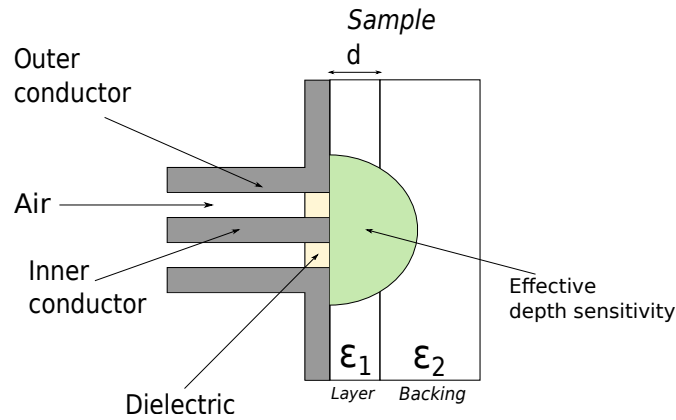


FIGURE 2.9: Sketch of open-ended coaxial probe with effective depth sensitivity with a sample with a layer of permittivity ϵ_1 and backing material with permittivity ϵ_2 .

A semi-empirical model has been created for estimating the permittivity of a sample of finite thickness, given by [6]:

$$\epsilon_{eff}^* = (\epsilon_2^* - \epsilon_1^*)e^{d/D} + \epsilon_1^* \quad (2.78)$$

Where ϵ_{eff}^* is the measured effective permittivity, ϵ_1^* is the layer permittivity, ϵ_2^* is

the permittivity of the backing material, d is the layer thickness and D is an empirical parameter that depends on the sensor geometry. With this model the effective permittivity of the sample can be solved, or if the permittivity is known the inverse problem of finding the thickness can be solved.

2.3.7 Equivalent circuit and bilinear calibration procedure

To relate the reflected signal S_{11} and the complex permittivity of the material being tested, the complex admittance of the equivalent circuit of the open-ended probe can be evaluated. A test environment as shown in figure 2.10a, results in a equivalent circuit as shown in figure 2.10b. In this example, Teflon is used as a dielectric

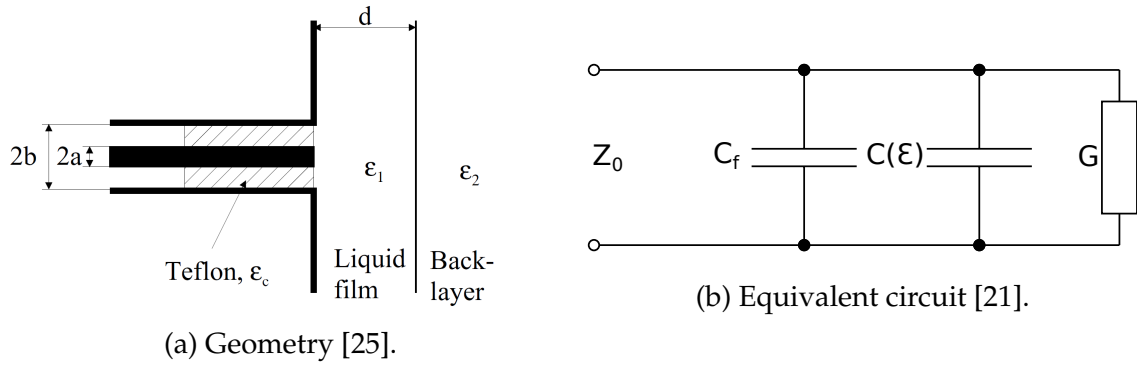


FIGURE 2.10: A open-ended probe connected with a test sample with backing layer.

medium between the inner and outer conductor of the probe. Z_0 is the characteristic impedance of the coaxial line, C_f represents the electric field concentration inside the dielectric part of coaxial line. The capacitance $C(\varepsilon)$ and conductance G represents the capacitance of the capacitor formed by the inner conductor and the test sample, and the radiation conductance of the probe. Evaluating the circuit in the frequency domain, the total admittance is be given by:

$$Y(\omega) = j\omega C_f + j\omega C(\varepsilon) + G \quad (2.79)$$

The radiation conductance in vacuum is given by [29]:

$$G_0 = \frac{4\pi}{3\eta} \left[\frac{(b^2 - a^2)}{\lambda^2 \ln(b/a)} \right]^2 \quad (2.80)$$

where λ is the wave length, η is the index of refraction in vacuum and a and b represents the inner and outer radius of the probe respectively. The conductance in

vacuum is related to the conductance in a material by [29]:

$$G = G_0 \varepsilon^{5/2} \quad (2.81)$$

As shown in equation (2.80) the conductance in vacuum depends on the geometry of the probe. In cases where a and b are small, we can neglect G and are left with a linear two capacitor probe model. It is also possible to rewrite equation (2.81) using the relation between the wavelength and the frequency:

$$\lambda = \frac{2\pi v}{\omega} = \frac{v}{f} \quad (2.82)$$

where v is the velocity of the wave which gives us a modified equation for the conductance:

$$G(\omega) = \hat{G}_0 \omega^4 \varepsilon^{5/2} \quad (2.83)$$

where \hat{G}_0 is the modified version of G_0 written in terms of frequency instead of wavelength. This frequency dependence of the conductance shows that it can only be neglected at low frequencies. Rewriting equation (2.51) as a function of admittance instead of impedance, the reflection coefficient at the reference plane becomes:

$$Y_L = \frac{1}{Z_0} \frac{1 - S_{11}^R}{1 - S_{11}^R} \quad (2.84)$$

Using a linear two capacitor model for the probe we can find the permittivity as a function of the reflection coefficient [25] as shown in equation (2.85). This is known as a bilinear calibration procedure (BCP) [24]. The iterative algorithms used for transforming the reflection coefficient has been provided by CMR. However, this model will not account for the radiation conductance, inducing increased error as the frequency increases:

$$\varepsilon^* = \frac{\tilde{A}S_{11}^M + \tilde{B}}{\tilde{C}S_{11}^M + 1} \quad (2.85)$$

It is to be noted that the three calibration fluids must have a permittivity close to that of the sample in order to achieve measurement accuracy.

2.3.8 Resonance Frequency

In section 2.3.7 we saw how the permittivity could be calculated by solving equation (2.85). If the given frequency results in a traveling length equal to an odd

number of quarter wavelengths, giving increased reflection. In turn, this can result in significant errors in the calculated permittivity [25]. This effect will limit the useful frequency range of the probe, making it restricted to frequencies below the first quarter-wavelength resonance, which is given by the following equation [25, p. 23]:

$$f < \frac{c}{4l\sqrt{\frac{\epsilon' + |\epsilon^*|}{2}}} \quad (2.86)$$

Where l is the travelling length and c is the speed of sound in vacuum. This equation was derived for sensor design of a coaxial cell, but it is assumed that this holds propagation in the MUT as well. However, for the purpose of this thesis, equation (2.86) also gives an indication of when it can be assumed that resonances will occur. If the MUT is low-loss, equation (2.86) is reduced to $f < \frac{c}{4l\sqrt{\epsilon'}}$.

2.3.9 Near-and far field

When dealing with an open-ended coaxial probe, the probe will radiate like an antenna at high frequencies. The electromagnetic field around an antenna is divided into two regions, near-field and far-field. These can be further subdivided into reactive near-field, radiating near-field and far field, the different regions is illustrated by figure 2.11. In the reactive near-field region, the \mathbf{E} and \mathbf{B} becomes complex resulting in field patterns that varies considerably from one point to another. Either the \mathbf{E} or \mathbf{B} -field may dominate at given points. The outer boundary of this region is given by [30]:

$$r_1 \leq 0.62\sqrt{\frac{D^3}{\lambda}} \quad (2.87)$$

where r is the distance from the probe, λ is the wavelength and D is the largest dimension of the of the probe. In the following region, the radiative near-field, the electromagnetic waves propagate predominantly in phase. However, the \mathbf{E} and \mathbf{B} fields are still complex, and becomes more predictable the further away from the antenna the wave gets before becoming a plane wave in the far-field region. The criteria for this region is given by [30]:

$$r_2 > \frac{2D^2}{\lambda} \quad (2.88)$$

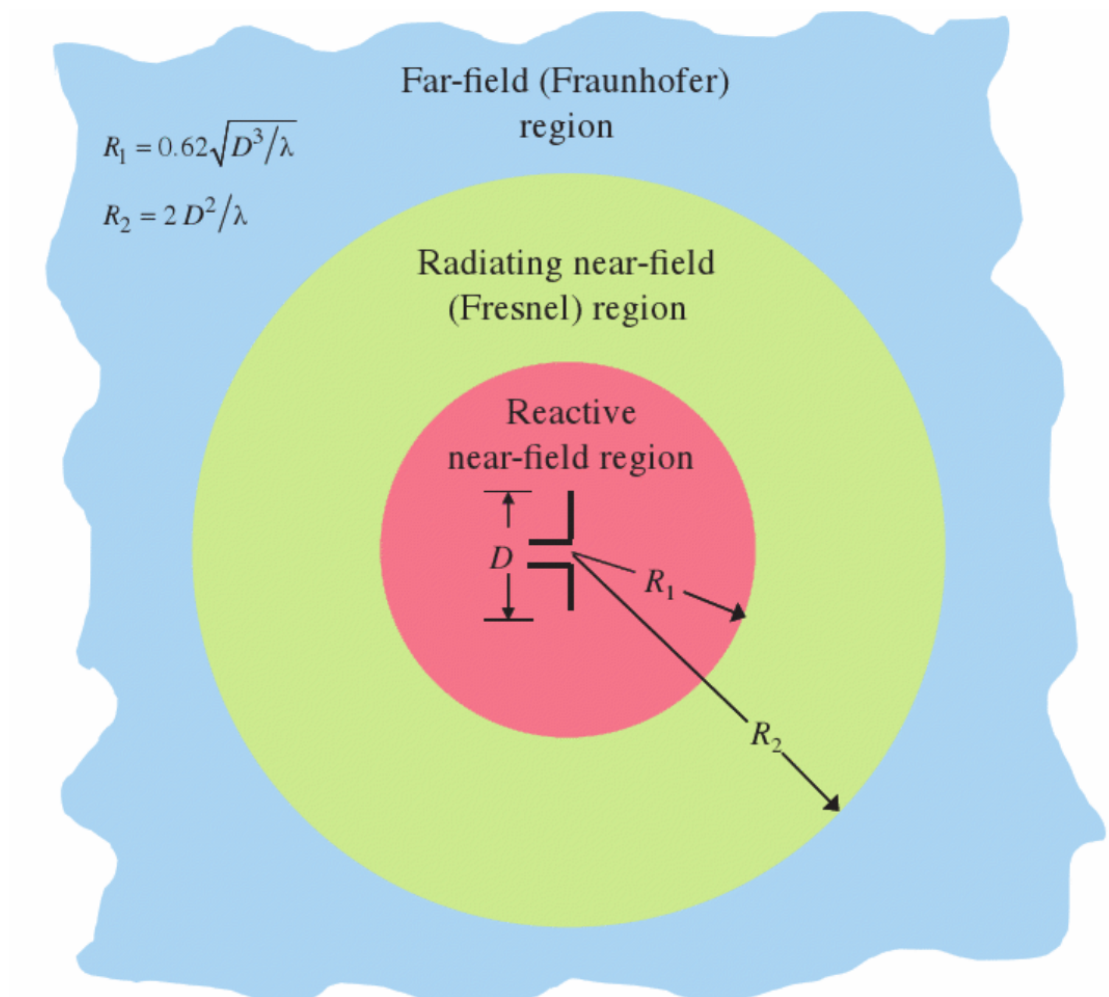


FIGURE 2.11: Near-and far-field of antenna showing the different regions [30].

which is known as the *far-field requirement*. In this region, the \mathbf{E} and \mathbf{B} field are in phase, mutually perpendicular and have equal magnitudes at any point in space. The radiative near and the far-field is often referred to as the Fresnel and Fraunhofer region respectively due to the analogy to optic terminology. The numerical values for the near-and far-field for the open-ended coaxial probe in this thesis, for a frequency of 13.6 GHz correspond to approximately 4.2 and 9.1 mm respectively.

Chapter 3

FE-modeling of sensor

In this thesis, a new experimental setup was created in order to do measurements on material with known permittivity. In this chapter a simulation model of the new experimental setup is built to simulate the measurement response. In chapter 5 results from some experiments are presented to verify the validity of the simulations.

The open-ended coaxial probe used in the simulations and the subsequent experiments, developed initially by Kjetil Folgerø and Kjetil Haukalid, is described in [1] as probe A. The probe is composed of a coaxial transmission line with an electrically open-end as discussed in chapter 2. The probe consists of an inner and an outer conductor, a dielectric support medium and air as an insulator as shown in figure 3.1 and in figure 2.9.

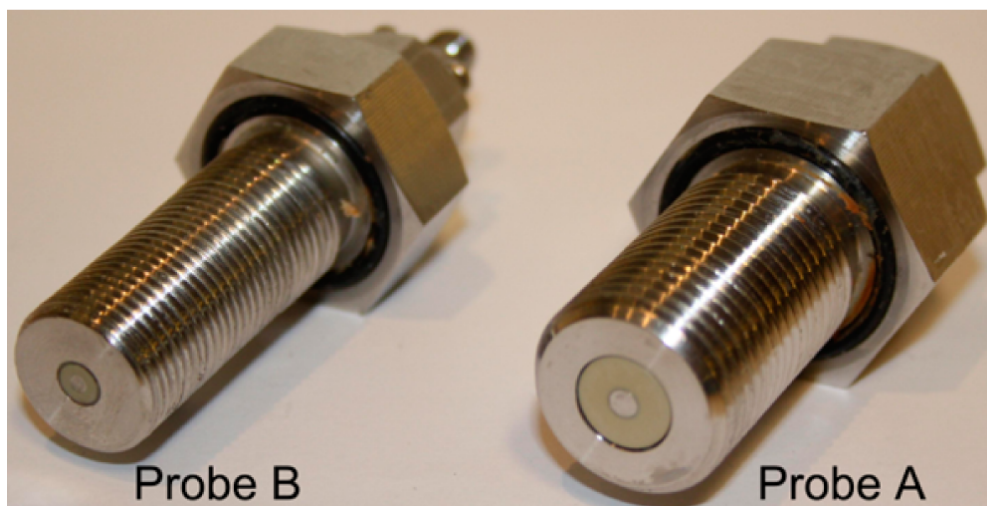


FIGURE 3.1: Two open-ended coaxial probes used in previous experiments [1].

3.1 Introduction to COMSOL®

Software simulations of physical experiments are efficient for evaluating and predicting physical effects prior to performing the experiment. CMR has used *COMSOL Multiphysics* as a tool to create a model for their open-ended coaxial probe and this simulation model was modified to include the new test setup described in this thesis. The main reason for choosing a FEM software for evaluating the behavior of the probe is that it is more flexible than full analytic wave models. The foundation of *COMSOL Multiphysics* is a Finite Element Analysis (FEA) software, which is formed by the laws of physics expressed as mathematical models which are discretized using the FEM [31].

3.1.1 Finite Element method

As presented previously, Maxwell's equations are the foundation of electromagnetism, and is based on a set of *partial differential equations* (PDEs). For the most part, geometries and problems involving PDEs cannot be solved analytically, and must instead be solved by approximations. This is achieved by using different types of discretizations that can approximate the PDEs with numerical model equations, which in turn can be solved using numerical methods. The solution to the numerical equations represent an approximation to the real solution of the PDEs. In our case we are solving for the wave equation (2.35), given by $\nabla^2 \mathbf{E} + k^2 \mathbf{E} = 0$.

In general the FEM involves the following steps [32]:

- Represent the structure of interest as a patchwork of smaller elements/domains.
- Express the unknown solution by interpolation of values at vertices/nodes of the elements.
- Assemble the resulting equations for each element into global matrix equations.
- Solve the global system of equations.

3.1.2 Boundary Conditions, Perfect Electric Conductor and Perfectly Matched Layer

In order to simplify the model of the simulation, several concepts has to be introduced that will be applied to the model. By still assuming we are propagating in linear media, where there is no free charge or no free current, $J = 0$ and $\sigma = 0$. As the wave is propagating from one medium to another it must obey the electrodynamic boundary conditions [9] [32]:

1. The tangential components of the electric field must be continuous.

$$\mathbf{E}_1^{\parallel} = \mathbf{E}_2^{\parallel} \quad (3.1)$$

2. The tangential components of the magnetic field must be continuous.

$$\mathbf{H}_1^{\parallel} = \mathbf{H}_2^{\parallel} \quad (3.2)$$

3. The normal components of the electric field must be continuous.

$$\varepsilon_1 E_1^{\perp} = \varepsilon_2 E_2^{\perp} \quad (3.3)$$

4. The normal components of the magnetic flux density must be continuous.

$$\begin{aligned} B_1^{\perp} &= B_2^{\perp} \\ \mu_1 H_1^{\perp} &= \mu_2 H_2^{\perp} \end{aligned} \quad (3.4)$$

But since $\mu_1 = \mu_2 = 1$ for most materials we are left with:

$$H_1^{\perp} = H_2^{\perp} \quad (3.5)$$

Some of the challenges when dealing with finite element modeling is how to treat unbounded boundaries, especially for wave structure interactions. One way to deal with this problem is to limit the extent of the model into a manageable region of interest, as shown in figure 3.2. The perfectly matched layer (PML) method was proposed by Berenger in 1994 [33], this method utilizes the use of an absorbing layer with a matched medium designed to absorb the electromagnetic waves without reflecting them. In addition, a boundary surrounding the PML consisting of a perfect

electric conductor (PEC) is added. A PEC boundary condition is essentially a surface without loss, which has a conductivity of $\sigma = \infty$, so that all field components must be zero inside the conducting region [32], i.e.

$$\hat{\mathbf{n}} \times \mathbf{E} = 0 \quad \text{or} \quad \hat{\mathbf{n}} \cdot \mathbf{H} = 0 \quad (3.6)$$

This result can also be seen by considering an imperfect conductor with a finite conductivity, where the skin depth goes to zero as the conductivity increases. This type of boundary is also called an electric wall, since the tangential components of the electrical field is shorted out and must vanish at the surface of the conductor [34].

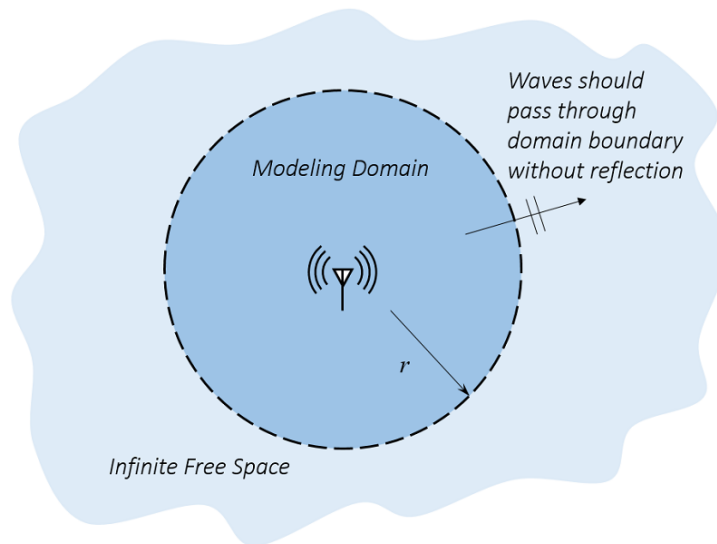


FIGURE 3.2: Modeling domain of an antenna in free space [35].

3.1.3 Port

We need to define where the electromagnetic waves enter and exit the model. This is where we change the frequency of the incoming waves to look at the response. For the purpose of computing S-parameters, only one port can be excited at a time.

3.1.4 Impedance boundary condition

It is a challenge that electromagnetic waves get scattered by a material. Since one has to derive the field expansion both inside and outside the material prior to the

application of the boundary conditions. To avoid this, impedance boundary conditions (IBC) can be applied in order to not calculate the field within the body, by assuming that the currents flow only the surface. This simplifies the analysis and reduces the computational time significantly since any material on the other side of the boundary is treated as infinitely large [36].

3.1.5 Mesh and Degrees of Freedom

As stated, the first step of finite element modeling is to represent the structure as a patchwork of smaller domains. The elements has to be chosen such that the shape and size represent the geometry and edges of the domain of interest. These elements form a mesh, that can be irregular in shape so it is possible to have finer elements where required and larger elements elsewhere. This makes the model more computationally efficient. For 2D models COMSOL chooses the option between triangular or quadrilateral elements. By default triangular elements are used for meshing. The reason for this is that triangular elements makes it possible to mesh automatically any 2D or 3D structure, regardless of shape or topology. By comparison quadrilateral elements are more difficult to generate automatically, but the accuracy of the simulation is often significantly higher then by using triangular elements [37]. It is also important to mention that COMSOL uses adaptive mesh refinement (AMR) for increasing the number of elements in regions where the error is significant. As a result AMR changes the element sizes in a nonuniform manner.

The solution time and and memory requirements of the solution is related to the number of degrees of freedom (DOF) in the model, the total number of DOF can be estimated by the following formula:

$$\#DOF = \#nodes \cdot \#dependentvariables \quad (3.7)$$

The dependent variable is present in all the nodes of the mesh and the number of nodes is related to the number of elements by the following approximations for 2D structures [38]:

- Linear triangular elements: $\#nodes = 0.5 \cdot \#elements$
- Linear quadrilateral elements: $\#nodes = 1 \cdot \#elements$

3.1.6 Symmetry

Many structures and objects exhibit symmetry in one form or another. The most common form of symmetry is mirror symmetry, axial symmetry, cyclic symmetry and repetitive symmetry. Theoretically, if you were to consider a finite element model of an object consisting of 100000 DOF, you could by mirror symmetry reduce the model to a quarter of the size and thus increase the accuracy of the numerical error, reduce the equation system and the load on the processor [37]. In general we can summarize the differences between a real life experiment and simulation with the comparison shown in table 3.1.

TABLE 3.1: Comparison of an experiment versus a simulation environment [39]

Real world	Simulation Enviroment
Anechoic chamber absorbing electromagnetic waves	Perfectly matched layer
Metallic coaxial cable and surface	· IBC · PEC
Network analyzer for measuring S-parameters	Port
Network or spectrum analyzer for measuring far-field radiation pattern	Far-field domain and calculation

3.2 COMSOL model of the experiment

The COMSOL model was created as a 2D axisymmetric model in order to save computational time. The model when evaluated is then rotated along the z -axis thus creating a 3D model from the 2D model. The model of the probe is based on CMRs existing probe, which was described in section 2.3.6. COMSOL uses the following work-flow which is generic regardless of the physics being modeled.

1. Set up the model environment
2. Create geometrical objects
3. Specify material properties
4. Define physics boundary conditions
5. Create the mesh
6. Run the simulation
7. Post-process the results

3.2.1 Model geometry

Figure 3.3 shows the layout and block information of the geometry, the respective parameter expressions in table 3.2 and the block definition with materials in table 3.3. The geometry consists of a cylindrical shell of Plexiglas with a PML on top to absorb the incoming electromagnetic waves without reflecting them. By using IBC, we truncate the domain in the r -direction. However, since the container is open-ended in the z -direction, a PML was placed on top of the measurement volume that consist of a backing material and the MUT. The height of the container from the measurement plane is 0.1 m. Thus, the height of the backing materials varies with the thickness of the slab. By simulation and far-field analysis, it was shown that the radiation was propagating primarily in the z -direction. The parameters that will vary during the simulation is the thickness of the slab and the permittivity of materials being tested. At the bottom, the probe is fed through a coaxial waveguide in TEM mode with increasing frequency. The probe in the simulation is simplified model of the real probe shown in figure 3.1.

It can be difficult to imagine how a 2D model is converted into a 3D model. Therefore, to understand how the probe is constructed in COMSOL a cross-section view

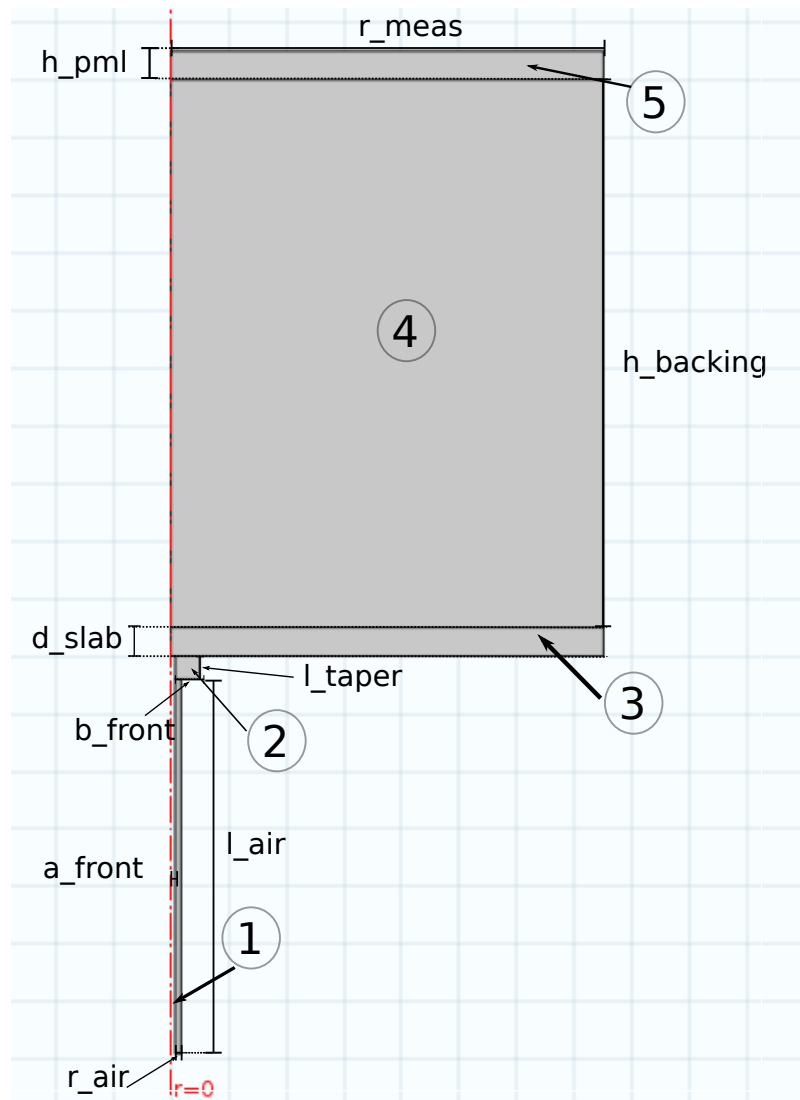


FIGURE 3.3: Block and layout information about geometrical model.

of the coaxial probe is shown in figure 3.4. Due to the IBC applied to the model it is not necessary to model the outer radius of the conductor to the probe. Rotating the axisymmetric figure around the z axis, from 0 to 270° , we see how a 2D model is transformed into a 3D model, as shown in figure 3.5.

3.2.2 Material

After defining the geometry of the model, the materials of the geometry must be selected. The block definition in figure 3.3 is given by table 3.3. When adding a user-defined material to the geometry, the properties of the material added depends on the physics that is applied to the model. In our case the electrical conductivity,

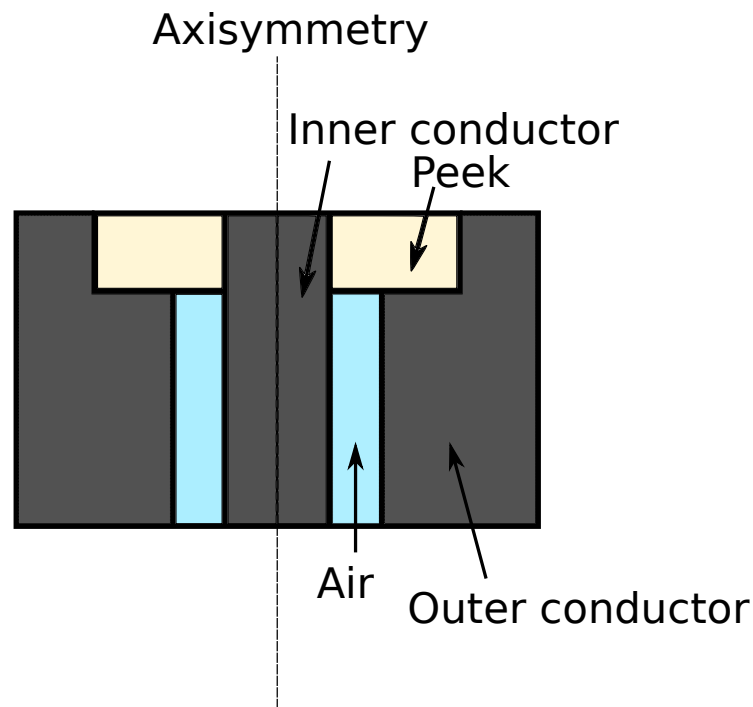


FIGURE 3.4: Cross-section view of the coaxial probe.

relative permittivity and relative permittivity has to be defined for solving the wave equation. The properties used for this model is shown in table 3.4.

TABLE 3.2: Parameter expression used to designing the geometry.

Name	Expression	Description
r_{meas}	r_{meas}	Radius of measurement volume
d_{slab}	d_{slab}	Thickness of layer
$h_{backing}$	$0.1 \cdot d_{slab}$	Height of backing material
l_{taper}	l_{taper}	Length of dielectric bead
a_{front}	a_{air}	Inner radius of dielectric bead
b_{front}	b_{front}	Outer radius of dielectric bead
a_{air}	a_{air}	Inner radius of air
b_{air}	b_{air}	Outer radius of air
r_{air}	$b_{air} - a_{air}$	Width of air insulator
l_{air}	l_{air}	Length of air insulator
h_{pml}	h_{pml}	Height of PML

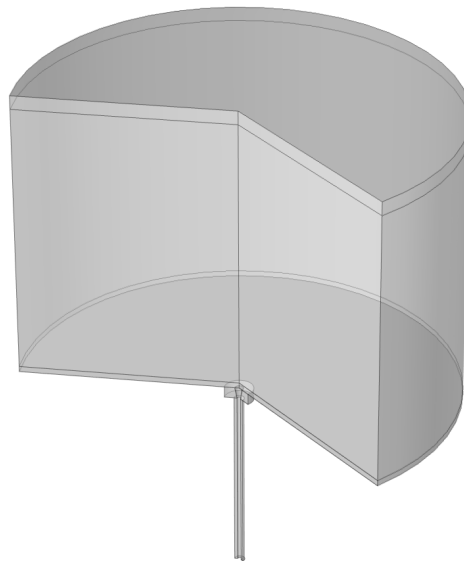


FIGURE 3.5: Transparent 3D visualization of the simulation from a 2D axisymmetric model, rotated from 0° to 270° .

TABLE 3.3: Block definition of the geometry in the model.

Block number	Material	Description
1	Air	Probe Insulator
2	Peek	Dielectricum
3	See Table	Material under test
4	Air	Backing material/Far field domain
5	Air	Perfectly matched layer

TABLE 3.4: Material definitions used in the model.

Material	Electrical conductivity [S/m]	Relative permittivity	Relative permeability	Reference
Polyether ether ketone (PEEK)	0	3.2	1	Ref
Air/Backing Material	0	1.000536	1	[40]
Slab	Varies	Varies	1	3.6

3.2.3 Boundary Conditions

The respective boundary conditions applied to the model is shown in figure 3.6. The inner and outer conductor of the probe is made of steel with a relative permittivity of $\varepsilon_r = 1$, relative permeability of $\mu_r = 1$ and an electrical conductivity of

$\sigma = 5 \cdot 10^5 [S/m]$. This will affect how far the waves penetrate into the conductor since the waves will be attenuated due to ohmic heating. Also, the measurement plane consists of a metallic surface, so the IBC is applied here as well. An additional IBC has been added to the wall of the container mimicking the Plexiglas surrounding the measurement volume. Here the permittivity is $\epsilon_r = 3.5$, permeability $\mu_r = 1$ and for simulation purposes the conductivity is set to $0 [S/m]$. One could have added air and PML outside the boundary of the Plexiglas, but the results from the simulations show that this was not necessary. Therefore the model was kept to minimum complexity to save computational time. The wave excitation port is placed at the bottom of the probe where the coaxial cable would have been connected in an experimental setting, as shown in figure 3.6.

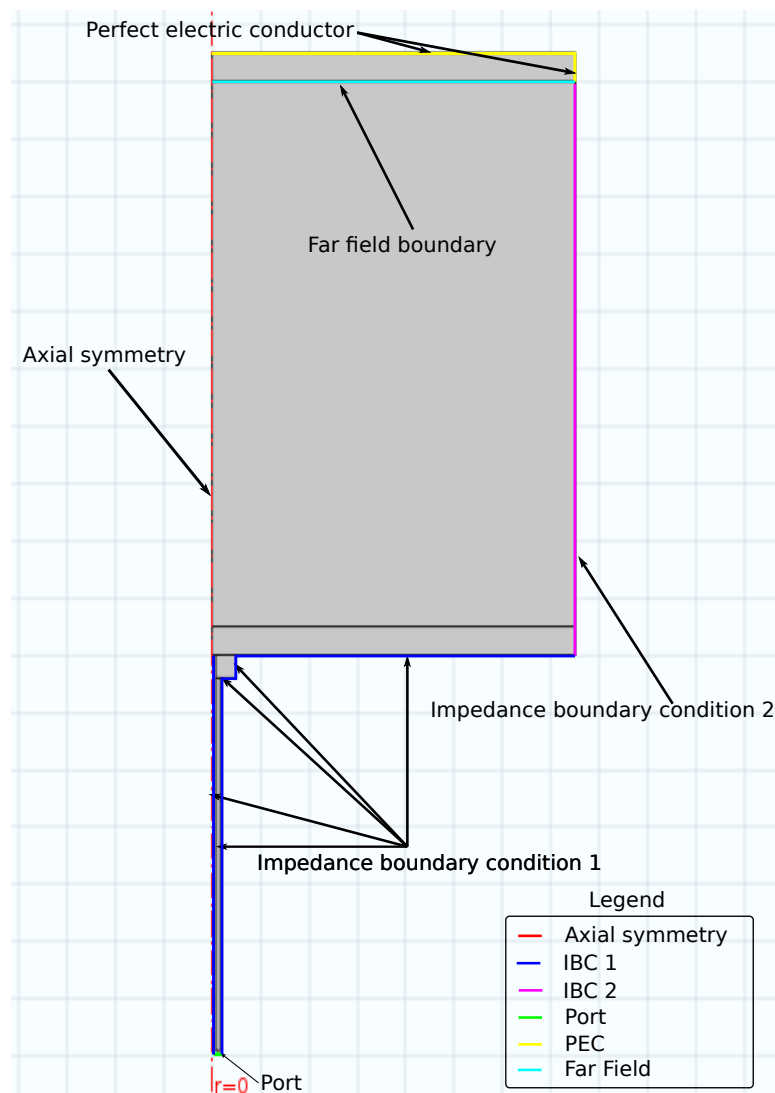


FIGURE 3.6: Boundary conditions of the simulations.

During the simulations, the port input power of the electromagnetic wave was set to 1[W]. To truncate the modeling domain, a PEC is used as periphery/termination on top of the PML, which will reflect any incoming electromagnetic wave.

3.2.4 Mesh

COMSOL Multiphysics has by default nine-built in size parameters for physics controlled mesh. Which range from extremely coarse to extremely fine. These predefined meshes are a set of 5 different parameters that are set, which consist of:

- **Maximum element size** - limits how big each mesh element can be.
- **Minimum element size** - limits how small each mesh element can be.
- **Maximum element growth rate** - limits the size difference of two adjacent mesh elements.
- **Curvature factor** - limits how big a mesh element can be along a curved boundary.
- **Resolution of narrow regions** - controls the number of layers of mesh elements in narrow regions.

With the physics used to define this model, the physics controlled mesh had the following parameters shown in table 3.5.

TABLE 3.5: Default parameters of the physics controlled mesh of the simulation model

General Physics	Maximum element size [m]	Minimum element size [m]	Maxium element growth rate	Curvature factor	Resolution of narrow regions
Extremely coarse	0.0574	0.0087	2	1	0.9
Extra coarse	0.0348	0.00278	1.8	0.8	1
Coarser	0.0226	0.00104	1.5	0.6	1
Coarse	0.0174	3.48e-4	1.4	0.4	1
Normal	0.0117	5.22e-5	1.3	0.3	1
Fine	0.00922	5.22e-5	1.3	0.3	1
Finer	0.00644	2.18e-5	1.25	0.25	1
Extra fine	0.00348	1.13e-5	1.2	0.25	1
Extremely fine	0.00174	3.48e-6	1.1	0.2	1

In order to determine which mesh that was the most suitable for our geometry, a mesh refinement study was conducted to monitor the solution time and convergence of the solution as the mesh was gradually refined. The testing conditions used during the mesh refinement study was a slab with thickness 0.2 cm consisting of water and air as backing material. As stated earlier, the frequency step size has

to be sufficient enough, to not lose any information. For this purpose 55 stepped measurements was chosen, which computationally wise was fast and provided enough information about the reflection coefficient. First the solution was tested with the physics controlled mesh. Afterwards the physics controlled mesh was used along with a custom mesh, which is denoted user controlled mesh. The parameter used to define the user controlled mesh was to limit the maximum element size of the physics controlled mesh and leave the other parameters to default. When the changes between each successful iteration was small enough, it was concluded that the model had converged. A free-tetrahedral mesh was applied to the regions of interest (block no. 1-3 in table 3.3). For the backing material an extra fine physics controlled mesh was used. When only modifying the maximum element size, it was important that the value was not less than the minimum element size. By letting the maximum element size be static and in the order of magnitude -4 and using different physics controlled meshes the magnitude and phase of the reflection coefficient remained the same within an acceptable range. Where the acceptable range was set to maximum deviation of 0.5 %. Therefore a normal physics controlled mesh was chosen with variable maximum element sizes of the different domains. Comparing the user defined mesh with that of the physics controlled mesh, the following response was obtained for the magnitude and phase of the reflection coefficient, as shown in figure 3.7 and 3.8. From the response we see that a user defined mesh results in a more accurate solution when the order of magnitude of is greater than -4 . Comparing the maximum deviation between -5 and -4 for the magnitude of the response, there was a difference of 0.2 % at 11.2 GHz. Comparing the phases there was no noticeable difference between each mesh. Therefore a magnitude of -4 for the maximum element size was chosen for simulation of the experiment due to accurate solution and a computational time that was acceptable.

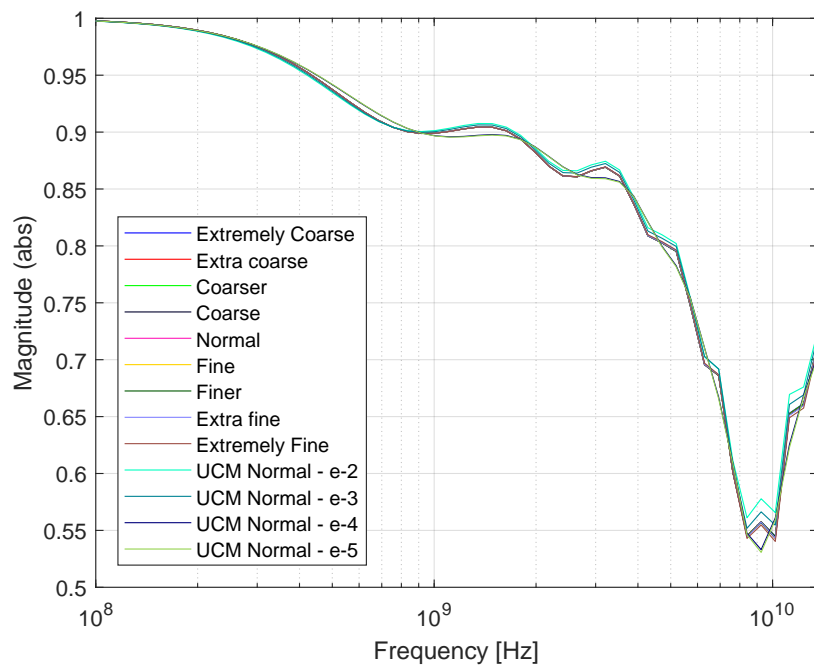


FIGURE 3.7: Magnitude of physics controlled mesh and user controlled mesh

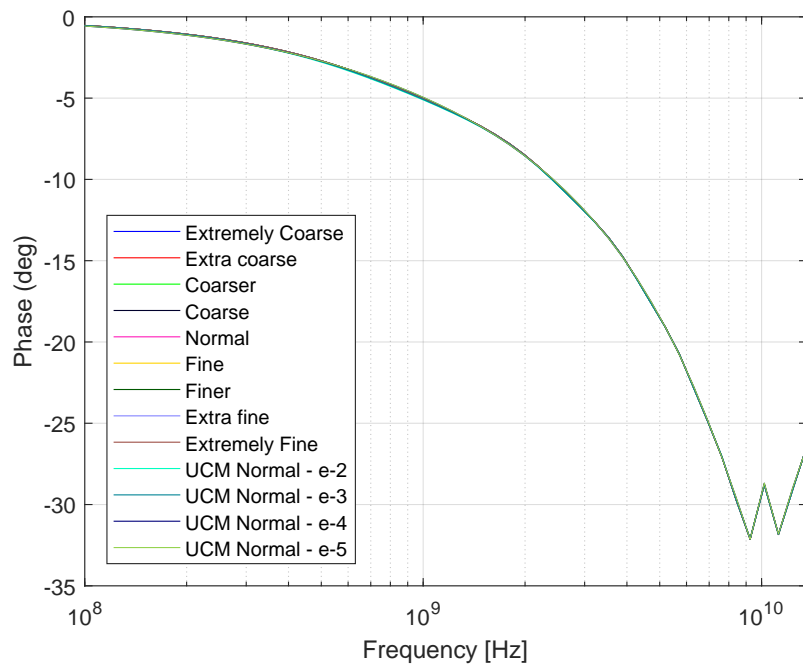


FIGURE 3.8: Phase of physics controlled mesh and user controlled mesh

The selected mesh resulted in the the following simulated mesh pattern, as shown in figure 3.9. From the figure we see that there is a significantly finer mesh in the regions of specific interest, i.e the probe and the slab. The same applies for the

backing material and PML which are physics controlled. The result of AMR gives nonuniform element sizes.

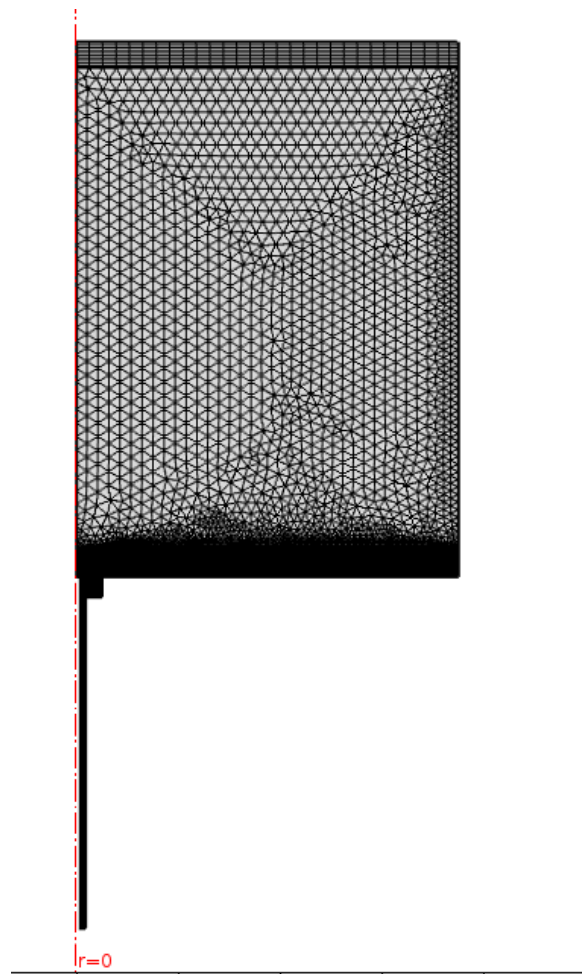


FIGURE 3.9: Finalized tetrahedral mesh of the simulation model.

3.3 Simulation

With the geometry, material and boundary conditions defined, a simulation matrix was obtained by iterating over the different materials shown in table 3.6 as layer and using air as backing material. The ethanol/water mixtures was chosen as layers due to the fact that the dielectric properties of these are well documented and their dielectric dispersion model could be implemented in COMSOL. The mixtures are given as a mole fraction of the concentration of ethanol in the mixture, i.e.

$$\chi_e = \frac{\text{moles of ethanol}}{\text{total moles}} \quad (3.8)$$

TABLE 3.6: Dispersion step $\Delta\varepsilon$, high frequency permittivity ε_∞ , relaxation time τ and conductivity σ for different ethanol/water mixtures at different mole fractions χ_e of ethanol at temperature $T = 20^\circ C$

Material	$\Delta\varepsilon$	ε_∞	τ [ps]	σ [S/m]	Reference
Water, $x_e = 0$	74.61 ± 0.2	5.6 ± 0.2	9.36 ± 0.05	0	[14]
Ethanol/Water mixture, $x_e = 0.22$	46.0 ± 1	4.4 ± 0.3	38 ± 4	0	[41]
Ethanol/Water mixture, $x_e = 0.36$	35.1 ± 2	4.6 ± 0.3	55 ± 3	0	[41]
Ethanol/Water mixture, $x_e = 0.54$	28.4 ± 0.3	4.3 ± 0.2	80 ± 5	0	[41]
Ethanol/Water mixture, $x_e = 0.76$	24.2 ± 0.2	3.8 ± 0.1	121 ± 1	0	[41]
Ethanol, $x_e = 1$	20.7 ± 0.1	3.5 ± 0.1	184 ± 2	0	[41]

The open-ended probe has a restricted sensitivity depth [6], but due to additional reflections from the sample boundary this can result in artifacts in the apparent permittivity. This effect is stronger at some frequencies. Due to resonances caused by the probe radiating like a monopole antenna at high frequencies [21]. The amplitude of the resonances will depend on the layer thickness of the sample, permittivity of the layer and backing material and the probe dimensions. To account for this, the simulations have been done on layers of up to 5 cm in incremental steps. The slab thickness simulations are done in 3 step sizes totaling 128 different thicknesses being simulated. The different layer thicknesses are shown in table 3.7. The frequencies have been selected to acquire information on the higher frequencies of the frequency span corresponding to that of the network analyzer used in the experimental setup (9 kHz-13.6 GHz). The simulations resulted in a S_{11} -matrix with dimensions $55 \times 128 \times 6$ which corresponds to the number of frequencies, slab thicknesses and materials respectively. The measurement results obtained from the simulations will be compared to the experimental values and a new method for thickness and material estimations using simulations will be described later. Some of the results from the simulation matrix are shown in appendix A as permittivity spectra, which was transformed using BCP.

TABLE 3.7: Different slab thicknesses for simulation purposes

Number of steps	Start thickness [mm]	Stop Thickness [mm]	Step size [mm]
25	0.1	2.5	0.1
13	2.6	5	0.2
90	5.5	50	0.5

Chapter 4

Experiment

In this chapter the experimental setup for measuring the reflection coefficient is presented along with other precautions to minimize errors. To ensure reproducibility, the equipment, setup and necessary steps are outlined here. The materials being tested is the same as the ones simulated but with greater incremental steps in terms of layer thickness than the simulations.

4.1 Experimental setup

The experiment was conducted at the chemistry lab at CMR. The equipment and materials used is presented in table 4.1. A figure of the setup is presented in figure 4.1. A new experimental setup was designed and built at the mechanical workshop at the Department of Physics and Technology, University of Bergen. The setup consists of a flange that was threaded so the probe could be inserted in the middle of the container. A plexiglass cylinder with a diameter of 15 cm and height of 10 cm was glued on top of the flange. A photograph of the setup is shown in figure 4.2. The interface between the network analyzer and the computer was made with a cross-over RJ-45 network cable for the data transfer data between a controller and the analyzer could be simplified. The network analyzer could then be controlled remotely, by utilizing scripts provided by CMR. The probe is connected to the network analyzer using a coaxial cable and the probe is installed at the bottom of the experimental setup which is elevated to avoid unnecessary bending of the coaxial cable.

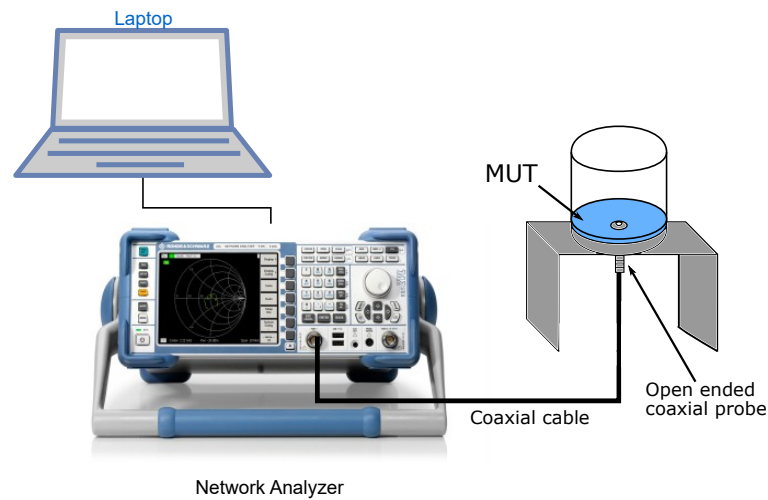


FIGURE 4.1: Model of experimental setup.

4.1.1 Preparation of fluids

To create the different ethanol/water mixtures, the ethanol available in the laboratory had to be diluted with distilled water in order to create the correct mole fractions needed. Unfortunately the ethanol bought commercially was contaminated with water and it was analyzed to have a mole fraction of $\chi_e = 0.865$. This meant that it was not possible to create pure ethanol mixtures for the experiments. The ethanol water mixtures and the appropriate masses needed to create the respective molar fractions is listed in table 4.2.

TABLE 4.1: Equipment and materials used

Equipment	Description
Network Analyzer	Rohde & Schwarz ZVL13
Probe	Probe A
Calibration kit	Rohde & Schwarz ZV-Z21
Coaxial cable	Flexco Coaxial Cable
Weight	Mettler Toledo Excellence
Computer	Dell Latitude E7240
Temperature sensor	F250 Mk II Precision Thermometer
Materials	See table 3.6

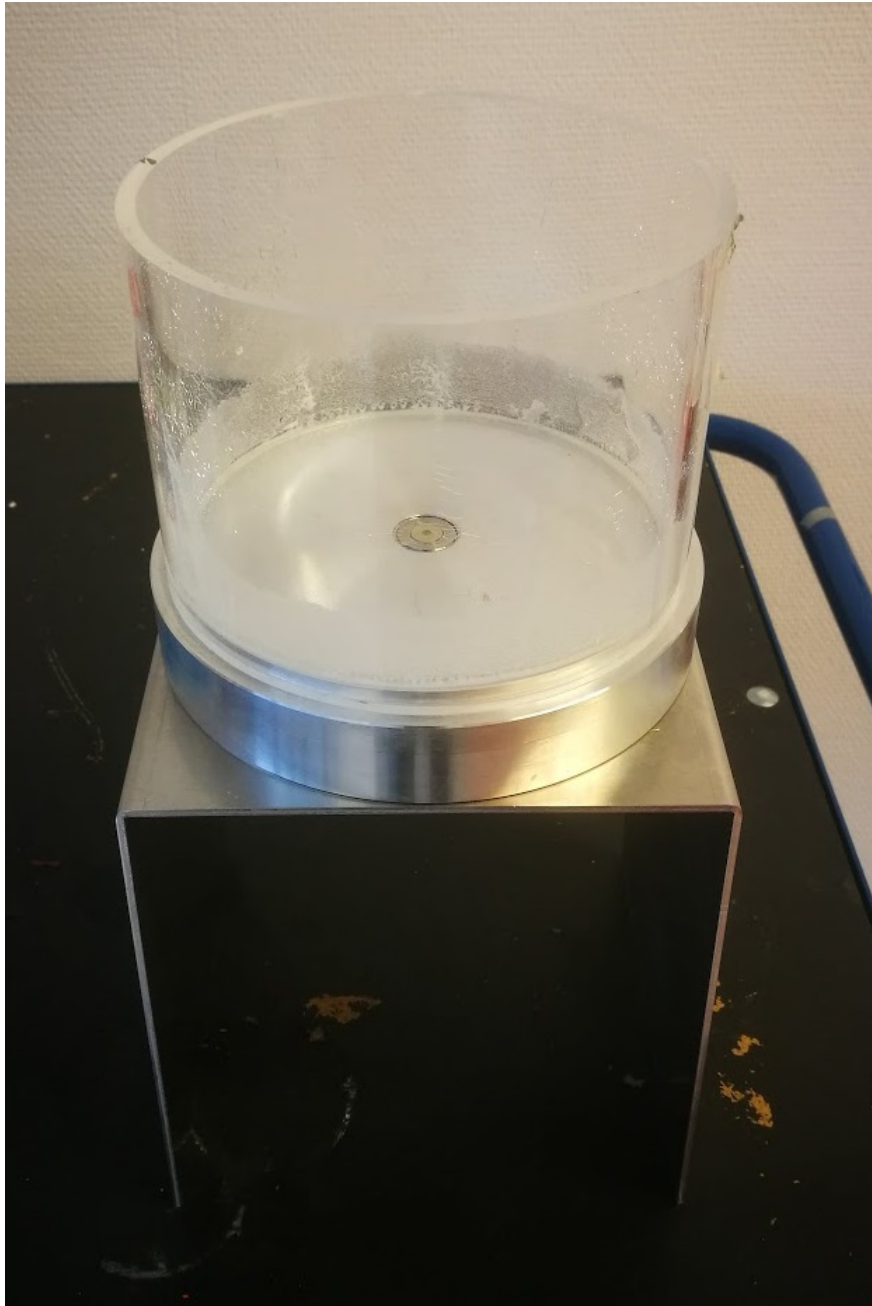


FIGURE 4.2: Photo of the experimental setup with the probe inserted in the center of the flange.

TABLE 4.2: Dilution table for creating different ethanol/water mixtures.

Mole fraction	Mass of distilled water [g]	Mass of contaminated ethanol [g]
$\chi_e = 0.22$	210.55	263.00
$\chi_e = 0.36$	284.70	170.16
$\chi_e = 0.54$	349.11	89.52
$\chi_e = 0.76$	401.72	23.65

4.1.2 Reducing uncertainty of the experimental setup

In order to reduce errors in the experimental setup the calibration was done prior to each experiment conducted. In addition several other precautions was taken into account, to minimize the total error of the system during the experiment, such as drift errors and systematic errors. The entire experiment procedure can be summarized, as shown in figure 4.3.

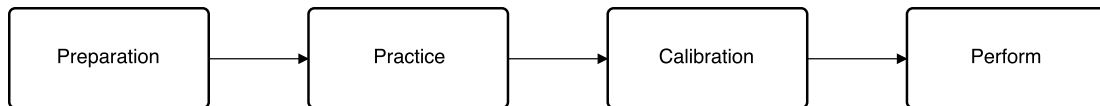


FIGURE 4.3: Steps of experimental procedure.

Where each step has the following substeps[42]:

- **Preparation** - The preparation steps include: sufficient warm-up time for the VNA, placing the VNA and MUT in a stable environment, using high quality adapters and torque wrenches, and check that the connections are clean and undamaged. A stable VNA and environmental temperature is needed to reduce drift in the VNA and permittivity, as seen in [41] and [14]. High-quality cables, adapters, torque wrenches and connectors improve measurement repeatability and reduce measurement uncertainty. The torque wrenches used, also reduces the mechanical damage to the equipment. In addition, an external temperature sensor was used to confirm the temperature of the material being tested.
- **Calibration** - After the leaving the VNA on for a sufficient time, the calibration is performed and a verification of the calibration is conducted.
- **Practice** - Set the respective parameters of the VNA, frequency span, etc. Check that the calibration standards and the probe is properly connected to the VNA.
- **Perform** - In this step the experiment is conducted. The temperature of the MUT is recorded for each experiment.

4.2 Measurements

The VNA parameters used in the experiment is summarized in table 4.3. Using the steps described in figure 4.3, the VNA was given sufficient warm-up time. Following, the coaxial cable was connected to the VNA using torque wrenches and

calibrated at the end of the coaxial cable using the 1-port full calibration described in section 2.3.5, i.e. using short, open and load calibration. The parameters of the broadband sweep was then set, using 1001 frequency points in the frequency range 10 MHz to 13.6 GHz. The room temperature was normally $\sim 20^\circ C$. However, the temperature of the liquids was measured continuously when performing the experiments. Due to the simulation material parameters used for the dielectric properties was given for a temperature of $20^\circ C$, as shown in table 3.6. The experiment was initiated with the container being empty. Following, the liquids was gradually poured into the container. Due to surface tension of the liquid, the layer thickness poured into the container could not be less than 2 mm for the layer to be considered homogeneously distributed across the diameter of the container. The layer thickness was increased from 2 to 25 mm, using 1 mm incremental step up to 3 mm and in 2 mm incremental step from 3 mm to 25 mm. Once the liquid had reached a maximum height of 25 mm, the container was emptied using a syringe to avoid any unnecessary movement of the measurement setup and cable. The remaining liquid residue was removed using paper towels and the procedure was repeated for the other liquids. The experiments on the liquids containing ethanol was done in succession with a minimized time interval between each layer thickness to avoid any unnecessary evaporation.

TABLE 4.3: Parameters set in the VNA

Frequency points	Bandwidth	Start Frequency	Stop Frequency
1001	100 Hz	10 MHz	13.6 GHz

4.2.1 Measurement uncertainty of layer thickness

The layer thickness of the experiment is adjusted by adding a known volume to the container. The volume is given by

$$V = \frac{\pi d^2 \cdot h}{4} \quad (4.1)$$

Solving for the height of the container we get

$$h = \frac{4V}{\pi d^2} \quad (4.2)$$

with the following uncertainty

$$\sigma_h^2 = \left(\frac{\partial h}{\partial V}\right)^2 \cdot \sigma_V^2 + \left(\frac{\partial h}{\partial d}\right)^2 \cdot \sigma_d^2 \quad (4.3)$$

$$\sigma_h^2 = \left(\frac{4}{\pi d^2}\right)^2 \cdot \sigma_V^2 + \left(-\frac{8V}{\pi d^3}\right)^2 \cdot \sigma_d^2 \quad (4.4)$$

where d is the diameter of the container, h is the desired height of the layer, and V is the volume. The caliper used to measure the diameter of the container has an accuracy of ± 0.02 mm and the diameter was measured to 149.5 mm. The measuring container used has an accuracy of ± 0.5 ml. We can treat the rectangular probability distributions as normal probability distributions by the following relationship

$$\sigma_x = \frac{\Delta x}{\sqrt{3}} \quad (4.5)$$

Where Δx is the rectangular, and σ_x the normal probability distributions respectively. This equipment used and uncertainties is summarized in table 4.4.

TABLE 4.4: Equipment to used measure diameter and generate layer thicknesses of appropriate heights with rectangular and normalized uncertainties

Component	Brand	Δx	σ_x
Measuring container	BLAUBRAND	± 0.5 ml	0.2887 ml
Caliper	Mitutoyo Digimatic 150 mm	± 0.02 mm	0.0115 mm

Thus, the measurement uncertainty of the layer thickness, is found to be ± 0.0285 mm. This is the measurement uncertainty for one particular layer. However, in the experiments, the volume was increased gradually. Which gives increasing error for time the volume was added due to different amounts of residue liquid present each time the liquid was poured into the container.

4.3 Interpolation

Typically, the frequency points of the simulation and measurements will differ. There are two possible solutions when comparing the experimental result to the simulations, i.e. either by fitting the experimental data to the simulation data, or by fitting the simulation data to the experimental data. Normally the latter will be the preferred method of approach due to the fact that a VNA during a broadband sweep will use a greater number of points than those used in the simulations. Also the simulations are not biased by systematic or random errors like the experimental data. In an ideal scenario one could have simulated for the frequency points of the experimental data. However, as discussed in chapter 3 this is a computationally intensive task which requires significant processing time. As a result one has to construct a continuously defined function from the discrete data. This remains a challenge when dealing with signal analysis. The most common approach to solving this problem is through interpolation. With interpolation the unknown values between the discrete values are estimated. The simplest form for interpolation is where a linear relationship between the different measurement are assumed. However, this technique is in many cases not sufficiently accurate so other interpolation techniques such as cubic, spline and polynomial interpolation is preferred instead [27].

By fitting experimental frequency points to the simulations, different interpolation techniques were compared to each other. The spline interpolation method gave the most accurate results of the different interpolation techniques available in MATLAB, but it fails at high frequencies due to an inadequate number of frequency points in this range, thus creating a high number of oscillations, as shown in figure 4.4. However, this was a result of interpolating the real and imaginary parts of the complex reflection coefficient, which was the default option in MATLAB. A better result was achieved by interpolating the magnitude and phase of the reflection coefficients separately, and recombining them again using the following formula:

$$S_{11} = Re^{i\theta} \quad (4.6)$$

Where R is the magnitude and θ is the phase angle of the complex reflection coefficient after interpolating. By using this method we achieve a better interpolation, as shown in figure 4.5. The figure shows that we are not creating a high number of oscillations at high frequencies, and we are able to create a well defined function that corresponds with the simulated data points. The other solution is to fit the experi-

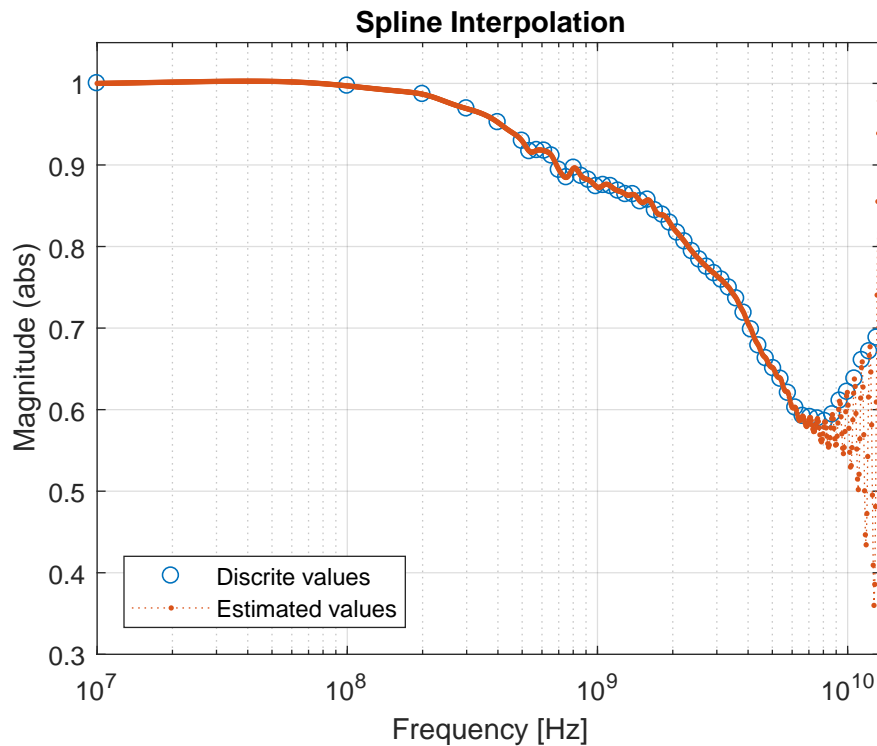


FIGURE 4.4: Spline interpolation method showing 55 simulated points fitted to 1001 experimental points for water with a layer thickness of $d = 50$ mm at $T = 20^\circ\text{C}$.

mental data to the simulations at the cost of measurement resolution but decreased oscillations at high frequencies as shown in figure 4.6. Results from fitting several different experimental data sets to the simulations yielded that the interpolation technique is only optimal for estimating values between discrete values e.g. if the experimental data has a max frequency of 13.6 GHz it will overestimate the value at 14 GHz, leading to increased error in the reflection coefficient. To avoid this, a mathematical function was developed which interpolates and removes the points below and above that of the experimental minimum and maximum frequency when interpolating. This proved to give a more accurate result.

4.3.1 Conclusion

By using appropriate techniques both interpolation of simulated frequency points to experimental frequency points and *visa versa* proved accurate. However, it was chosen to fit the experimental frequency points to simulation points since the interpolation technique also smoother the noise present in the experiments.

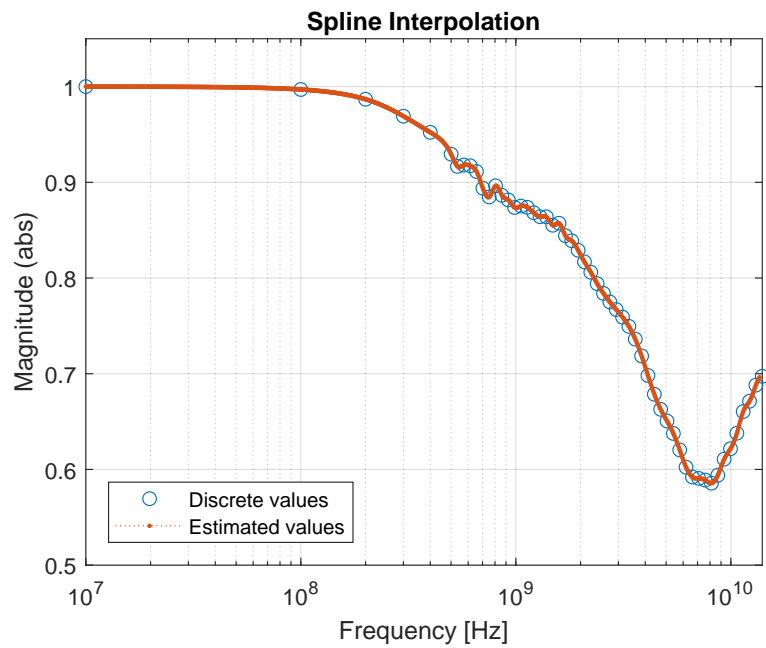


FIGURE 4.5: Spline interpolation of magnitude and phase, showing 55 simulated points fitted to 1001 experimental points for water with a layer thickness of $d = 50\text{mm}$ at $T = 20^\circ\text{C}$.

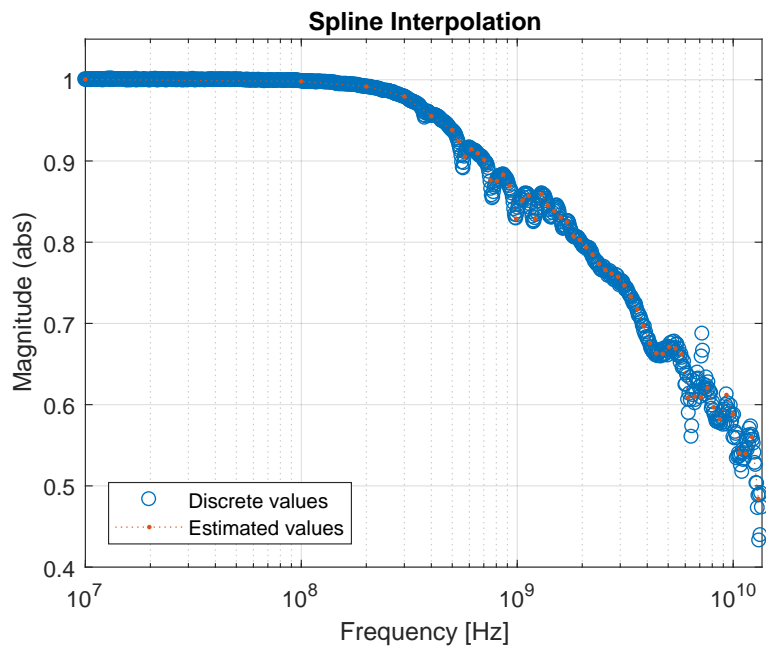


FIGURE 4.6: Spline interpolation method showing 1001 experimental points fitted to 54 simulation points for water with a layer thickness of $d = 40\text{mm}$ at $T = 20^\circ\text{C}$.

Chapter 5

Results and discussion

In this chapter the results from the simulations and the experiments are presented, and with emphasis on how simulations can be used to estimate the layer thickness and the permittivity of the materials simultaneously. The transformation from reflection coefficients to permittivities is achieved using the bilinear calibration procedure (see section 2.3.7).

The second part of this chapter focuses on the occurrences of resonances, using a theoretical model and simulations. And how the resonances can be used to estimate layer thicknesses greater than the probe sensitivity depth. It will also be indicated which characteristic features that are optimal for resonances for the specific probe, e.g.

- Frequency range
- Permittivity range
- Layer thickness range.

5.1 Estimating material and layer thicknesses using FEM simulations

5.1.1 Comparison of permittivity (ϵ^*)

In this section the complex permittivity measurements from the FEM simulation spanning different ethanol/water mixtures and layer thicknesses from chapter 3 are evaluated to estimate layer thickness and material of the measured data. The comparison procedure is presented here and is also shown in figure 5.1.

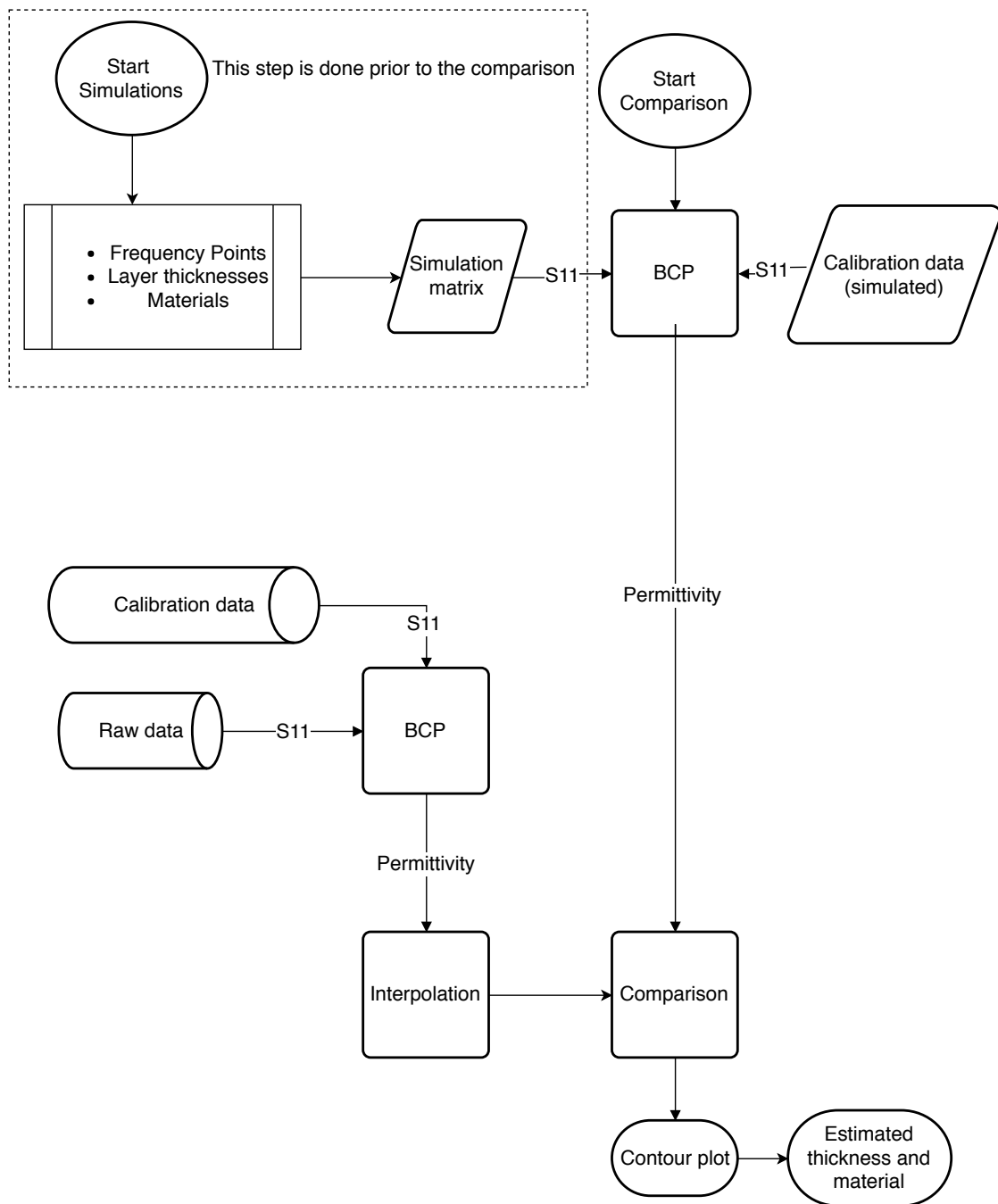


FIGURE 5.1: Flowchart of the process for evaluating material and layer thickness using permittivity for comparison.

where following steps are

- **Simulation matrix;** the simulation matrix spans the relevant layer thickness and layer permittivity ranges for a given frequency range. This is a time-consuming process and must be done prior to doing the experiments.
- **BCP of simulation data;** here the reflection coefficient matrix from the simulation data is transformed from reflection coefficient S_{11} to complex permittivity ε^* . To achieve this the response of air, water and contaminated ethanol was simulated. These calibration fluids were chosen since they have permittivities close to that of the sample in order to achieve high precision. The compounds and their corresponding dielectric model and constants are shown in table 5.1
- **BCP of measured data;** here the difference between the measurement plane and reference plane is removed by using the same calibration fluids and dielectric models as in the simulation.
- **Interpolation;** here the experimental data is fitted to the simulation data using the spline interpolation technique. This also reduces the random noise of the measured signal.
- **Comparison of simulated and experimental data;** this step can be divided into two parts. If the layer thickness and material is known, the measured data can be compared against the appropriate layer and be evaluated. The second part is to solve the inverse problem, i.e. to estimate the material and layer thickness of an unknown sample using the transformed measured permittivity.

TABLE 5.1: Calibration fluids for transformation from reflection coefficient S_{11} to permittivity ε . for simulated and experimental data

Compound	ε_s	ε_∞	$\Delta\varepsilon_1$	$\Delta\varepsilon_2$	τ_1 [ps]	τ_2 [ps]	α	Dielectric model	Reference
Air	1.000536	N/A	N/A	N/A	N/A	N/A	N/A	Constant	[40]
Ethanol $\chi_e = 0.865^1$	25.2422	4.0760	21.1662	2.2326	145.72	21.997	0.0778	Cole-Cole	[41]
Water	80.21	5.6	74.61	N/A	9.36	N/A	0	Debye	[14]

Testing this method for various liquid layers shows a good compliance between the measured and simulated spectra, thus verifying the validity of the simulations. Figure 5.2 shows the response of the measured data, the simulation data and the reference value of water with a layer thickness of 5 mm and air as backing material. The artifacts caused by resonances in the GHz-region is observed and is in accordance with the theory. To create a plot of how the measured data compares with the simulated data, a contour plot was used. By mapping the mole fraction

¹This mole fraction was used to reflect what was commercially available in the laboratory, model was achieved by interpolating the mole fractions from [41].

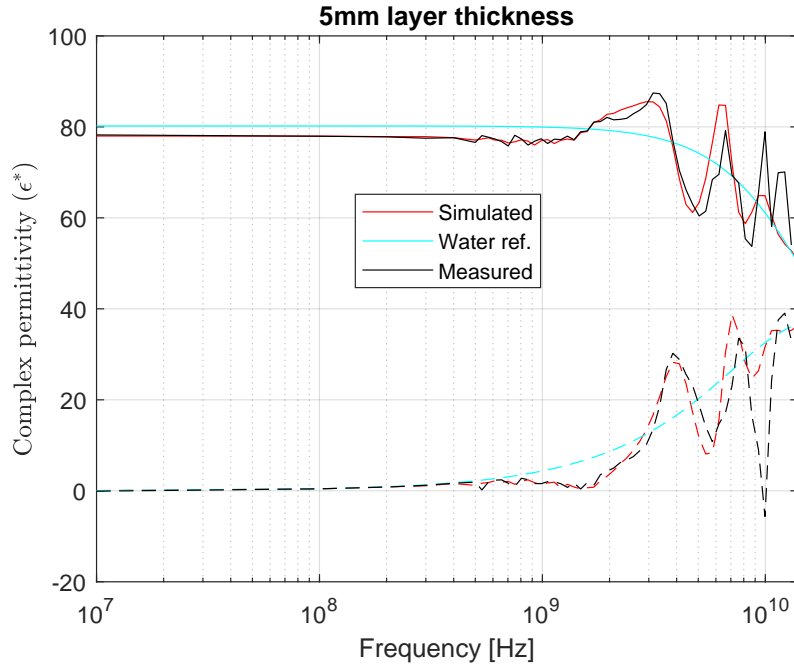


FIGURE 5.2: Comparison of simulation and experimental result of water with a layer thickness of 5mm and air as backing material.

of ethanol in the x -direction and the layer thickness in the y -direction, the error of the measured data is shown as amplitudes in the xy -plane. The error of the complex permittivity was estimated using a root square deviation (RSD) on the real and imaginary part for all frequency points, given by the following formula

$$RSD = \sum_{i=1}^M \sqrt{(\varepsilon'_{meas} - \varepsilon'_{sim(i,j)})^2} + \sum_{i=1}^M \sqrt{(\varepsilon''_{meas} - \varepsilon''_{sim(i,j)})^2} \quad i, j \in M, N \quad (5.1)$$

Where M is the number of frequency points of the simulation matrix and N is the number of simulations in the matrix. This corresponds to the rows and columns of the simulation matrix, respectively. Using RSD as amplitudes with respect to the xy -plane, we get the following contour plot of the same measurement data as shown in figure 5.2. Using a different method for evaluation, the error may result in different contour plots. This method evaluates the complex permittivity, but is also possible to include the phase into the comparison. By evaluating different techniques for estimating the error of the experimental data compared to the simulations, we saw that a logarithmic scale of the error ($\log(RSD)$) had a better performance then using RSD directly.

As seen in figure 5.3 the error is largest the further away the mole fractions are from water, and smallest in a area around 5 mm water. This is be expected due to the measurement uncertainty of the layer thickness in the experiment.

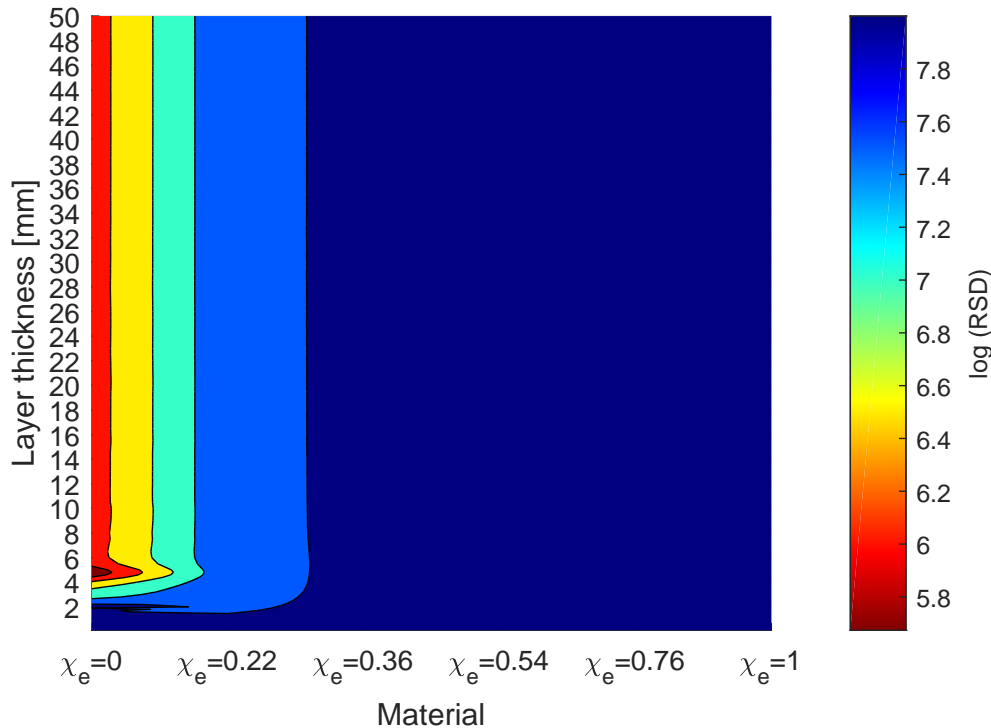


FIGURE 5.3: Contour plot of experimental result of water with a layer thickness of 5mm and air as backing material with respect to simulations.

5.1.2 Comparison of reflection coefficient (S_{11})

When comparing the simulated and experimental data, we can either compare the complex permittivity ε^* , as shown in the previous section or compare the reflection coefficient S_{11} directly. The flow chart for this procedure is shown in figure 5.4. The procedural flow is the same as in figure 5.1. However, in this case the calibration fluids from the simulations and the experiments are used to transform the reflection coefficient from the measurement plane to the simulation reference plane using equation (2.75) (BST). Using the same experimental data as in figure 5.3, i.e. water with a layer thickness of 5 mm and air as backing material the response can

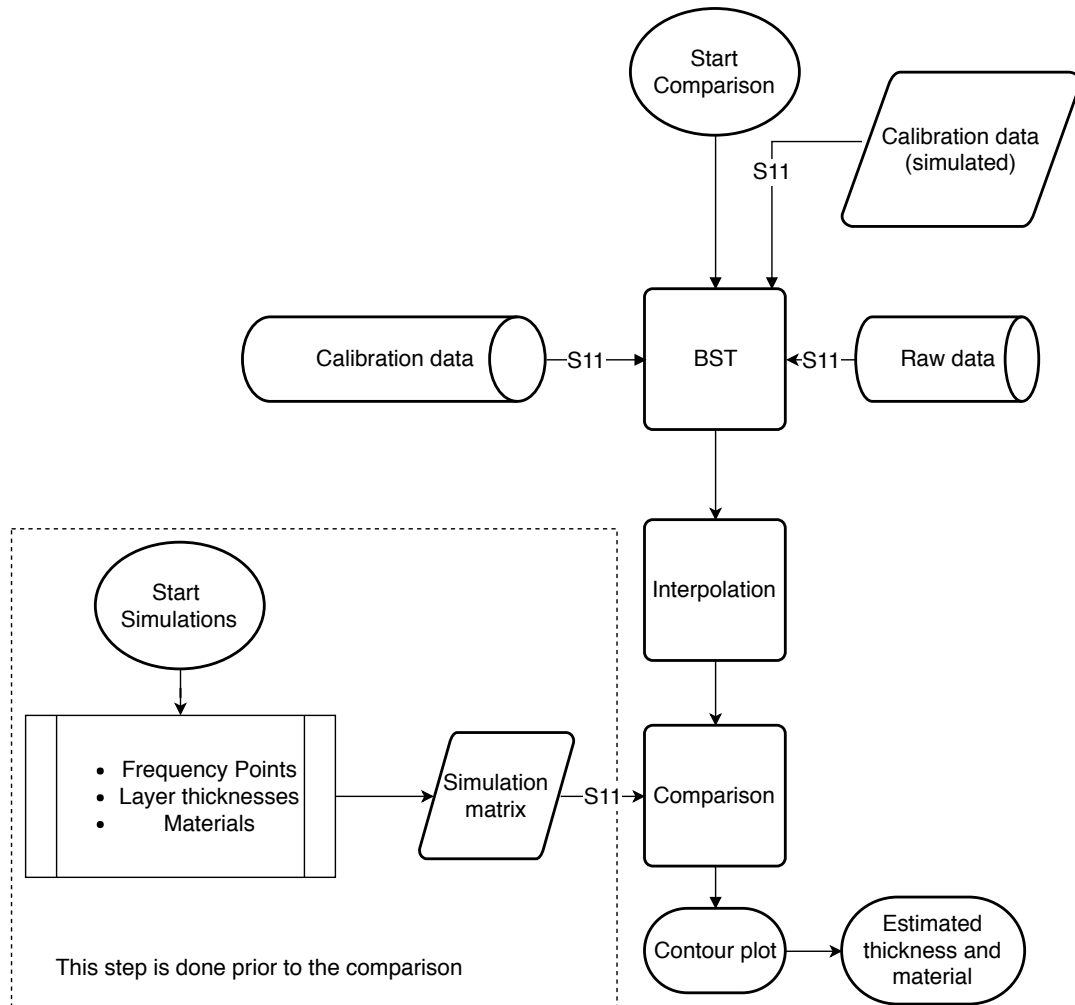
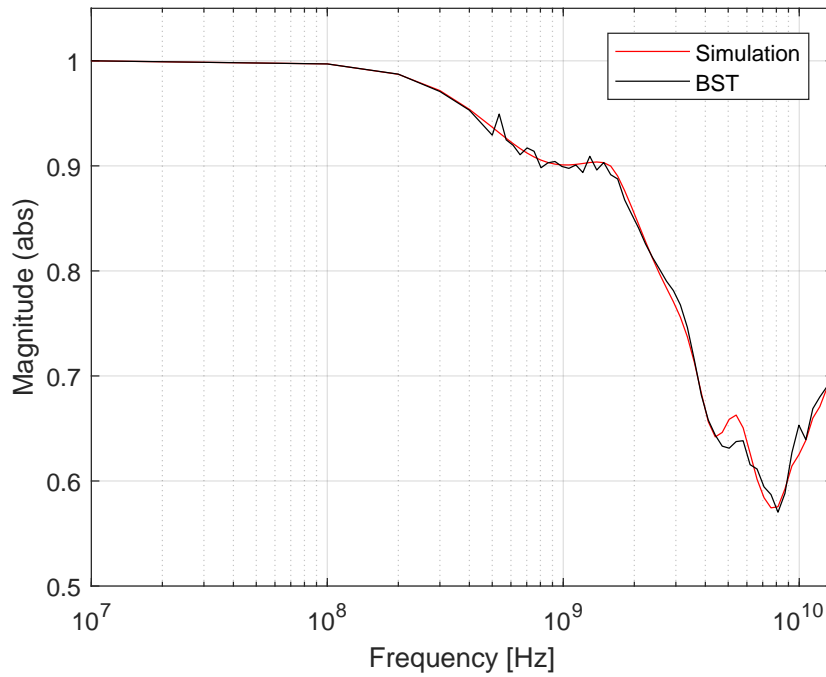
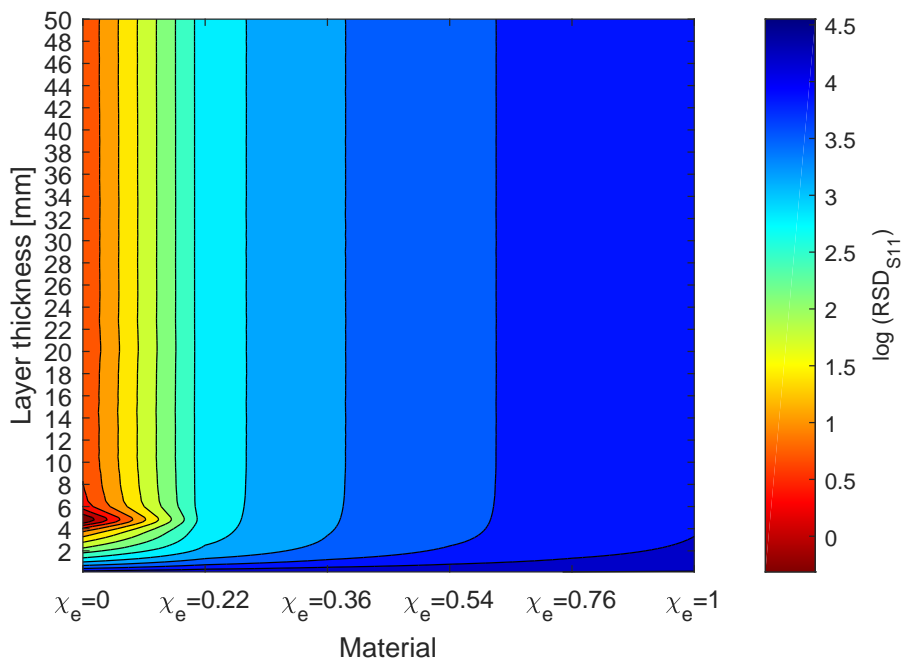


FIGURE 5.4: Flowchart of the process for evaluating material and layer thickness using the reflection coefficient for comparison.

be evaluated using the reflection coefficient instead, as shown in figure 5.5. To estimate the error of the measured reflection coefficient compared to the simulations a RSD evaluation of the real and imaginary part of the reflection coefficient was used, which can be summarized by equation (5.2)

$$RSD_{S_{11}} = \sum_{i=1}^M \sqrt{(S'_{11,meas} - S'_{11,sim(i,j)})^2} + \sum_{i=1}^M \sqrt{(S''_{11,meas} - S''_{11,sim(i,j)})^2} \quad i, j \in M, N \quad (5.2)$$

In this case we also used a logarithmic scale of the RSD of the reflection coefficient ($\log(RSD_{S_{11}})$). Using this method we see that we need a larger resolution on the level-step of the contour plot in order to estimate the layer and the material of experimental data being evaluated. This is to be expected since transforming the reflection coefficient to permittivity using BCP will result in a large total error when evaluating the deviation of the measurement, this is especially true when resonances occur, since this leads to a large error in the complex permittivity.

(a) S_{11} 

(b) Contour plot

FIGURE 5.5: Contour plot of experimental result of water with a layer thickness of 5mm and air as backing material with respect to simulations using S_{11} .

5.1.3 ε^* and S_{11} comparison

Comparing the permittivity of a different measurement with an ethanol/water mixture of $\chi_e = 0.76$ and with a layer thickness of 5 mm it required an increase in the level-step of the contour plot compared to that of water in order to estimate the layer thickness of the sample. The reason for this is that the artifacts caused by resonances are much less apparent for a larger fraction of ethanol than they are for water. However, we see clearly that the material is most likely to be $\chi_e = 0.76$ and the layer thickness around 5-7 mm, as shown in figure 5.6. In figure 5.7a the reflection coefficient S_{11} is compared against the equivalent simulated response. From this figure, we see small deviance in the reflection coefficient. This can be explained by a deviance in the mole fraction since a small change in the water content of the mixtures will affect the reflection coefficient accordingly. In figure 5.7b a contour plot of is shown based on a logarithmic RSD of the reflection coefficient with respect to the simulations. Here we are unable to determine an accurate solution in terms of layer thickness. However, we can estimate the material to be $\chi_e = 0.76$. This result proves that the permittivity is the preferred option when comparing the measurement against the simulations, since the method can estimate both the layer thickness and the material of the sample.

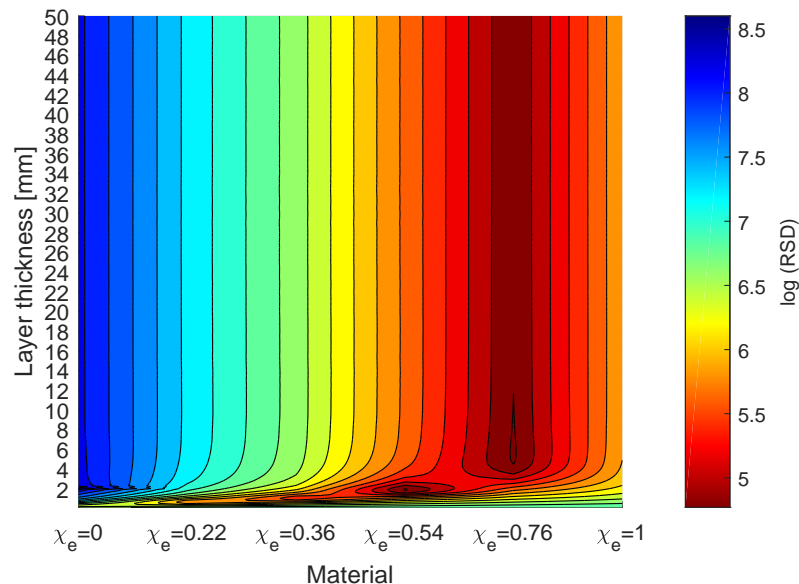
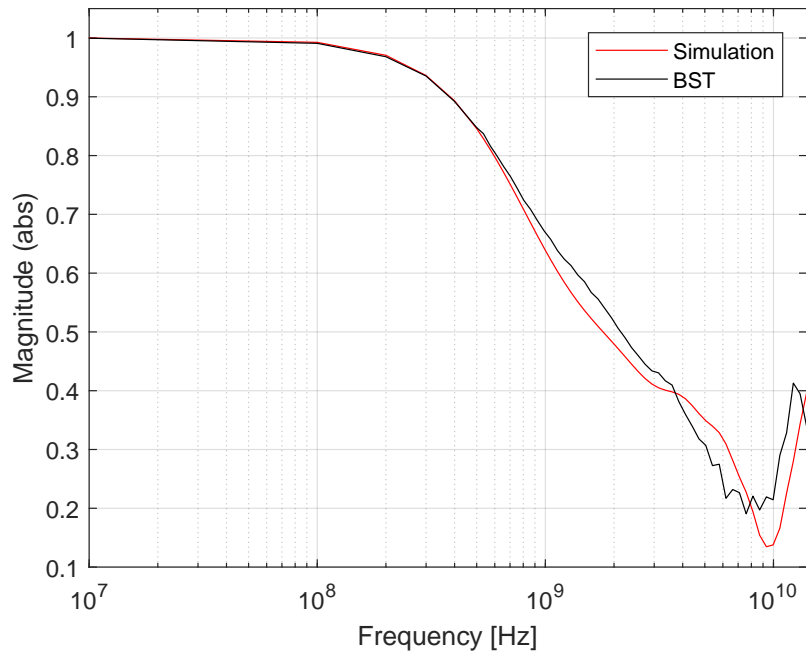
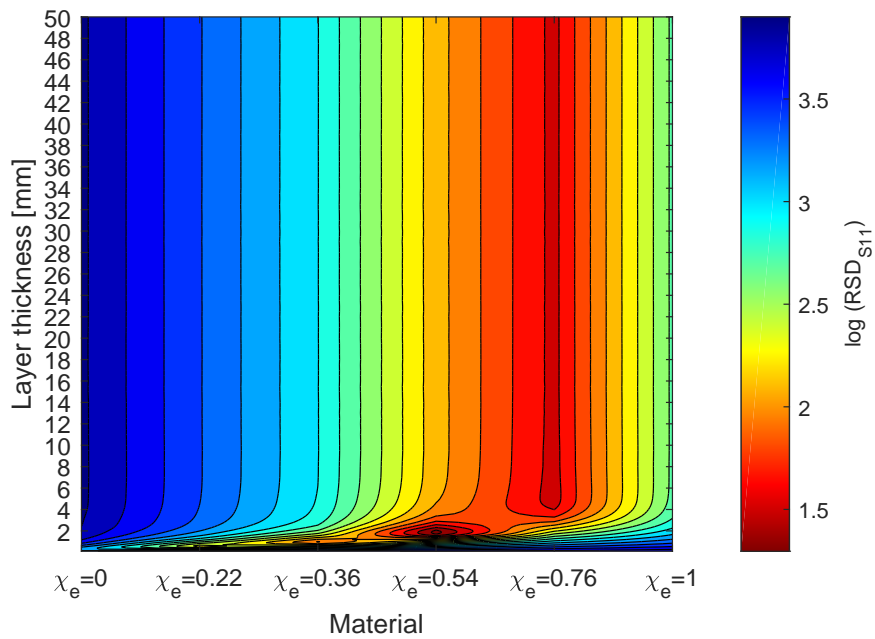


FIGURE 5.6: Contour plot of experimental result of $\chi_e = 0.76$ with a layer thickness of 5mm and air as backing material with respect to simulations.

In appendix B, a paper accepted for presentation at the "ISEMA" conference using permittivity for comparison and RSD is included [43]. In the paper a 3 mm thick water layer is presented in figure 6, and a 3 mm thick contaminated ethanol layer is presented in figure 7, both with air as backing material. The responses shown in the paper include the best fit of the comparison between the measured spectra and the simulations and the reference value of the given response. We see a good compliance between the best fit and the reference. From the results in the article and the results shown in figure 5.3 and 5.6, we see the accuracy of the solution indicated by the color of the contour plot, where a deep red color indicates the least deviation with the simulated spectra. We observe that the red-colored area is more defined, the higher the water content in the ethanol/water mixtures, due to artifacts caused by the occurring resonances.

(a) S_{11} 

(b) Contour plot

FIGURE 5.7: S_{11} and contour plot of experimental result of ethanol/water mixture, $\chi_e = 0.76$ with a layer thickness of 5mm and air as backing material with respect to simulations.

5.1.4 Layer thicknesses larger then the probe sensitivity

As mentioned previously, when resonances occur this leads to a large error in the complex permittivity. Usually resonances present an unwanted measurement error. However, by using the information when the reflection coefficient is transformed to permittivity using BCP, this can be used to estimate layer thicknesses greater than the sensitivity of the probe. Evaluating a 13 mm water layer with air as backing material, we get the response as shown in figure 5.8, and a zoomed response as shown in figure 5.9. From the responses we see that the experimental result is most likely to be water with a thickness between 12-14 mm. Layers with thicknesses larger then the critical sensitivity depth of the probe (for probe A this is normally around 7-8 mm), will be considered infinitely thick. We see that by evaluating responses that generates resonance for a given probe dimension, layer thickness and material we are then able to estimate layers that are greater then the sensitivity of the probe. For comparison, the response for 13 mm layer consisting of an ethanol/water mixture with $\chi_e = 0.54$ is shown in figure 5.10. From the plot it can be seen that it is not possible to find a distinct response for what the layer thickness of the compound is,

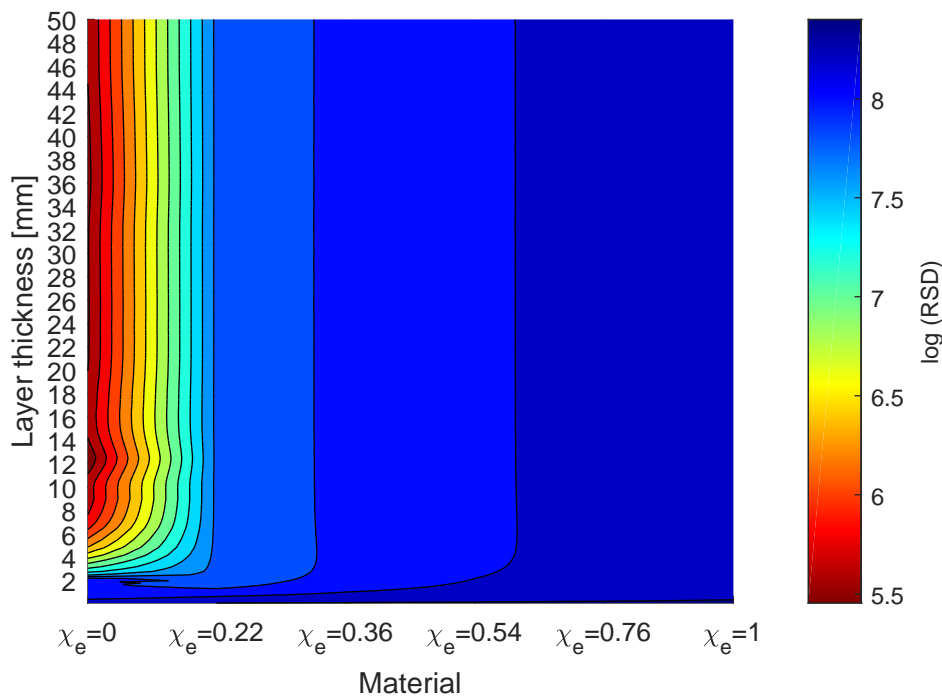


FIGURE 5.8: Contour plot of experimental result of water with a layer thickness of 13mm and air as backing material with respect to simulations.

since at this depth it is considered infinitely thick. We are however able to determine that the layer consists of $\chi_e = 0.54$ quite clearly.

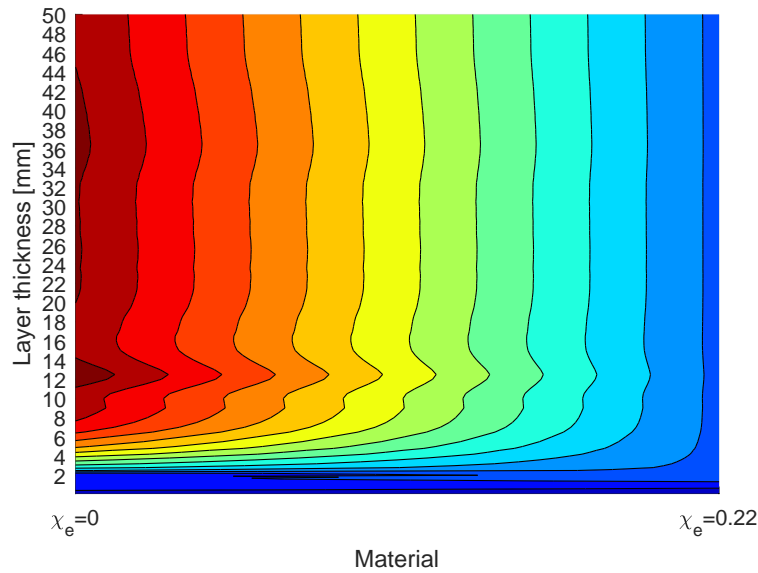


FIGURE 5.9: Zoomed response from figure 5.8

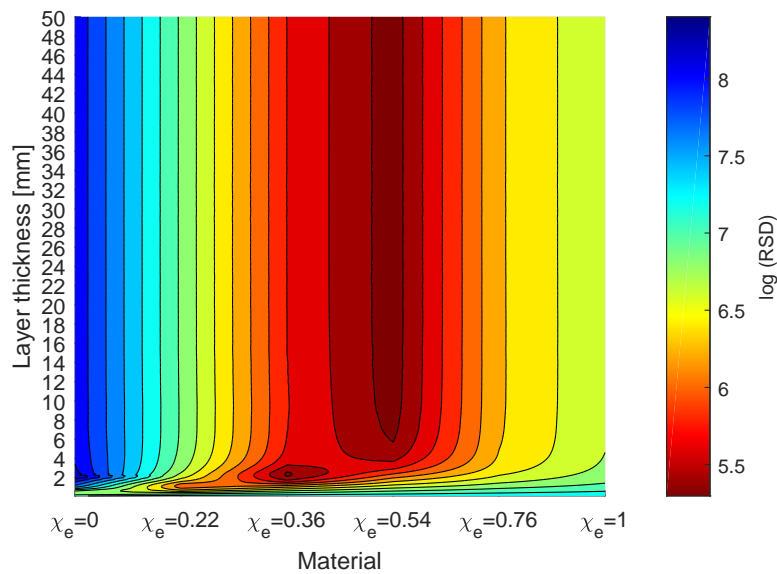


FIGURE 5.10: Contour plot of experimental result of $\chi_e = 0.54$ with a layer thickness of 13mm and air as backing material with respect to simulations.

5.2 Resonances

As discussed previously, the probe radiates at high frequencies. When measuring on samples with finite thicknesses, this can result in additional reflections from the sample boundary, as illustrated in figure 1.1. This effect will be greater on frequencies corresponding to quarter-wavelength resonances, as discussed in section 2.2.2. From the simulations and experimental results, we see that the resonances primarily emerges in the GHz region of the measured reflection coefficient. By looking at the reflection coefficient and permittivity of a specific case, i.e. 12 mm water as layer and air as backing material, as shown in figure 5.11. We see that the amplitude of the resonance in this case, is small for the given layer thickness and which is to be expected due to attenuation of the electromagnetic wave. To emphasize this result, a new simulation was conducted with a theoretical medium consisting of water with no loss, i.e. no imaginary part in the complex permittivity. This resulted in large resonances when the probe became radiating. The comparison between water and loss-less water is shown in figure 5.11.

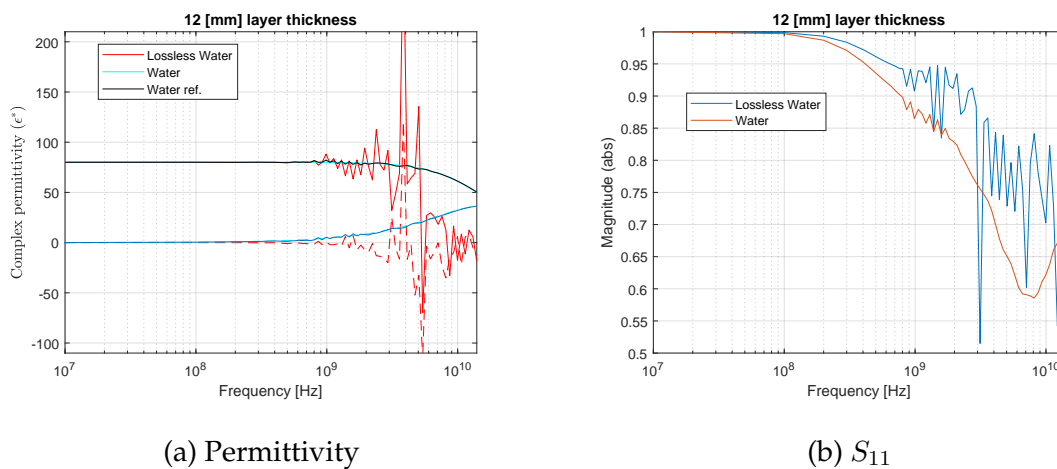


FIGURE 5.11: Simulated response of water and loss-less water ($\epsilon^* = 80.21$) with 12 mm layer thickness and air as backing material.

From this comparison we see that the more dissipative the medium is, the fewer resonances occur. By evaluating the simulation matrix for different ethanol/water mixtures with a layer thickness of 5 mm we see this effect clearly in both the permittivity and reflection coefficient. While evaluating the response of different materials and backing-layers, the results show that there were only significant resonances occurring for water layers and with air as backing material, as shown in figure 5.12.

To analyze the effect of resonances further, the simulations were reversed, i.e. using air as layer and ethanol/water mixtures as backing material, as shown in figure 5.13. From the figure, we see that we have only small resonances in the permittivity spectrum of air-filled layers with liquids as backing material. This result could also be derived from equation (2.86), which for a 5 mm air-filled layer, the first resonance occurs above approximately 15 GHz. This shows that there are limitations to which material can be used if the resonances are to be used to estimate layer thicknesses greater than the probe sensitivity depth and to improve the accuracy of the contour plots. To determine when resonances occur at a given layer depth and for different materials, a simplified theoretical model has been developed using transmission line theory. The theoretical model is compared against the simulations, in order to verify the usefulness of the model.

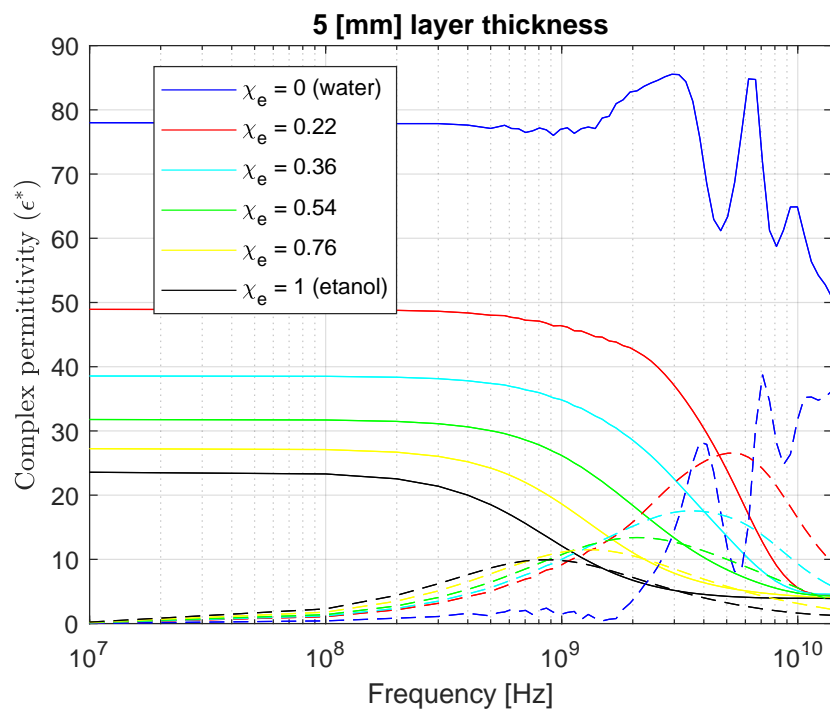
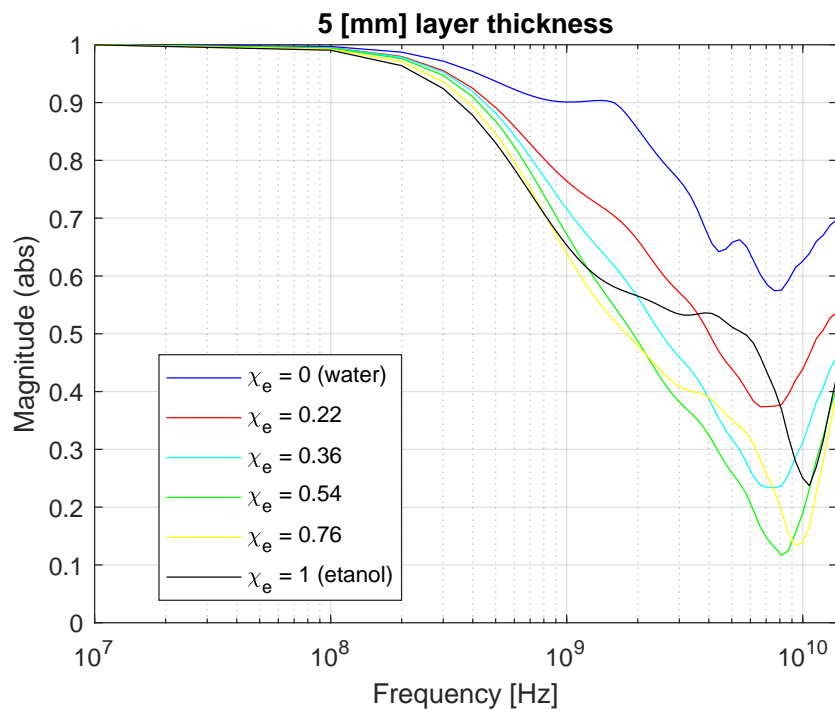


FIGURE 5.12: Permittivity and reflection coefficient for simulated mixtures of ethanol/water mixtures as layer and air as backing material.

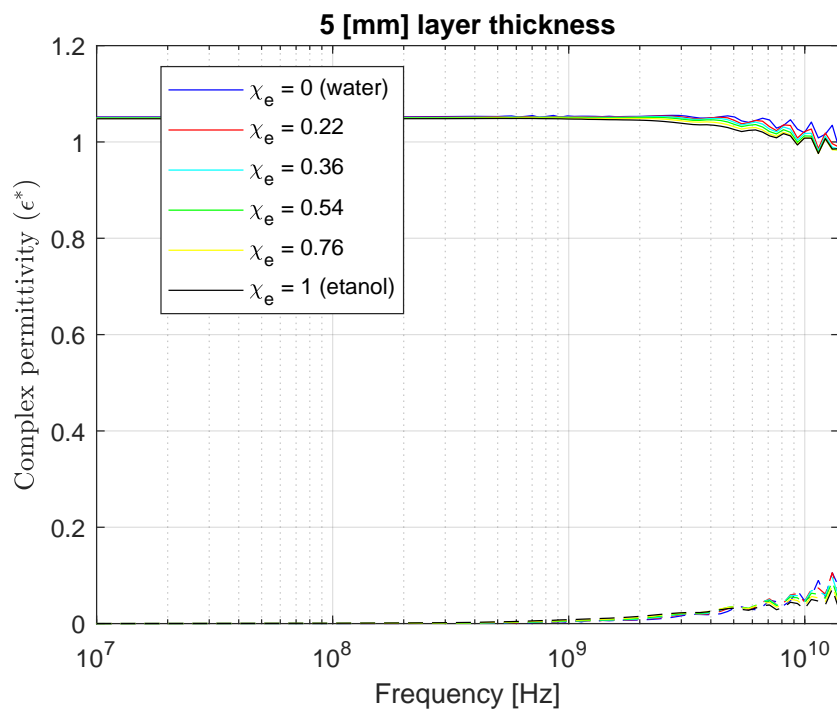
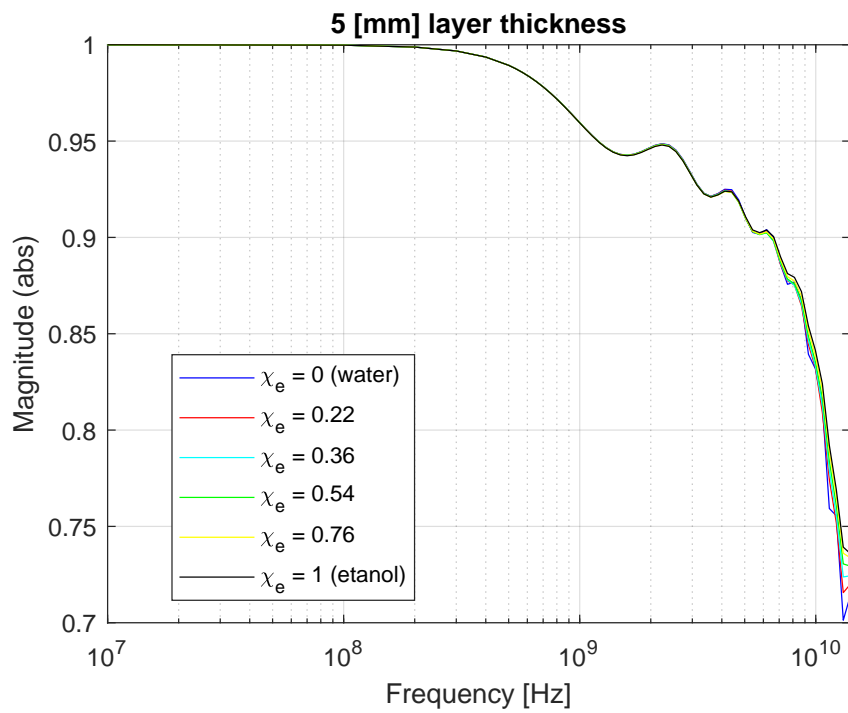


FIGURE 5.13: Permittivity and reflection coefficient for simulated mixtures of ethanol/water mixtures as backing material and air as layer.

5.2.1 Simplified model of the reflection coefficient

Assuming that we have an electromagnetic wave propagating in free space and the wave is plane propagating into an isotropic, homogeneous dielectric with negligible magnetic properties and zero conductivity, a simplified model was created, as shown in figure 5.14.

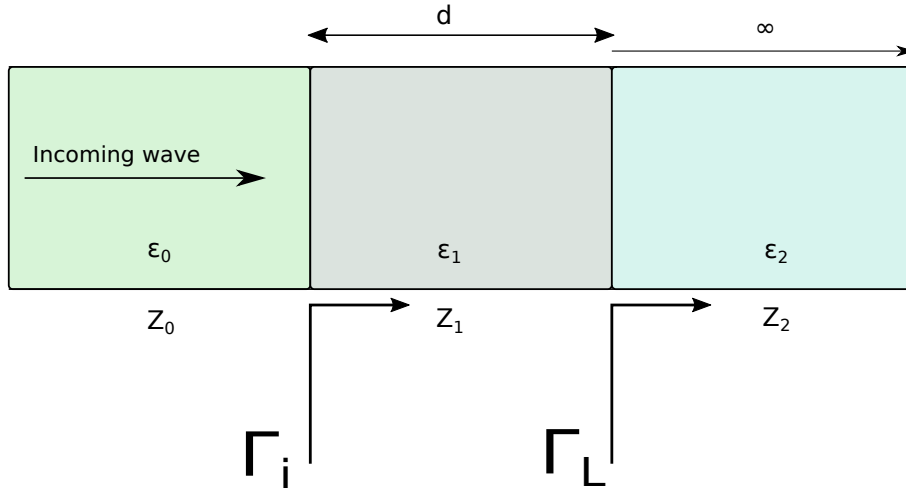


FIGURE 5.14: Simplified model of electromagnetic wave propagating in free space hitting a layer with thickness d and permittivity ϵ_1 , and a backing material of infinite length with permittivity ϵ_2 .

The wave impedance Z for the given medium can then be calculated by the following equation [12]:

$$Z = \sqrt{\frac{\mu}{\epsilon}} = \sqrt{\frac{\mu_0}{\epsilon_0 \epsilon_r}} = \frac{Z_0}{\sqrt{\epsilon_r}} \quad (5.3)$$

where Z_0 is the wave impedance of free space, which is approximately:

$$Z_0 = \sqrt{\frac{\mu_0}{\epsilon_0}} \approx 376.73 \Omega \quad (5.4)$$

From the equations derived in section 2.2.1, the reflection coefficient for the boundary between the layer and the backing material can be found:

$$\Gamma_L = \frac{Z_2 - Z_1}{Z_2 + Z_1} = \frac{Z_0 \left(\frac{1}{\sqrt{\epsilon_2}} - \frac{1}{\sqrt{\epsilon_1}} \right)}{Z_0 \left(\frac{1}{\sqrt{\epsilon_2}} + \frac{1}{\sqrt{\epsilon_1}} \right)} = \frac{\sqrt{\epsilon_1} - \sqrt{\epsilon_2}}{\sqrt{\epsilon_2} + \sqrt{\epsilon_1}} \quad (5.5)$$

The input impedance and input reflection coefficient can then be deduced:

$$Z_i = Z_1 \frac{1 - \Gamma_L e^{-2\gamma l}}{1 + \Gamma_L e^{-2\gamma l}} \quad (5.6)$$

where

$$\Gamma_L e^{-2\gamma l} = \frac{\sqrt{\varepsilon_1} - \sqrt{\varepsilon_2}}{\sqrt{\varepsilon_2} + \sqrt{\varepsilon_1}} e^{-j \frac{4\pi f l}{c} \sqrt{\varepsilon_1}} \quad (5.7)$$

and finally the input reflection coefficient can be calculated by

$$\Gamma_i = \frac{Z_i - Z_0}{Z_i + Z_0} = \frac{Z_1 \frac{1 - \Gamma_L e^{-2\gamma l}}{1 + \Gamma_L e^{-2\gamma l}} - Z_0}{Z_1 \frac{1 - \Gamma_L e^{-2\gamma l}}{1 + \Gamma_L e^{-2\gamma l}} + Z_0} \quad (5.8)$$

5.2.2 Comparison of theoretical model vs simulation

Using the simulations as a reference tool, the performance of the theoretical response versus the simulated response is estimated. To thoroughly evaluate the performance of the simplified model, 5 cases were studied using the simulations as a reference and air as backing material.

- Case 1. Debye vs Simulation.
- Case 2 - High permittivity, loss-less medium
- Case 3 - Low Permittivity, loss-less medium
- Case 4 - High permittivity with loss
- Case 5 - Low permittivity with loss

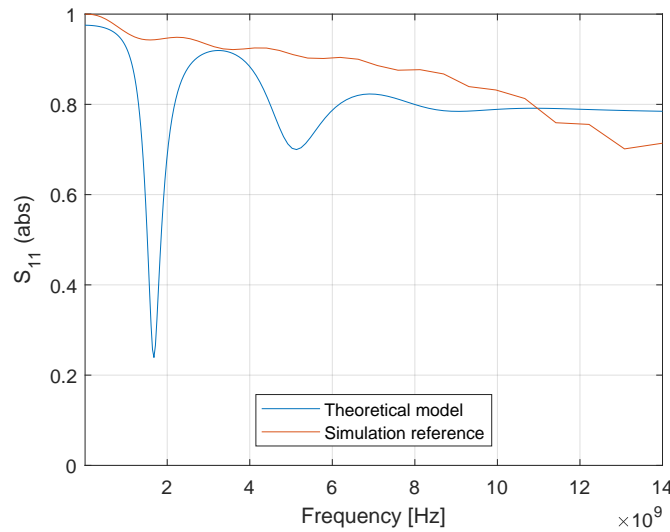


FIGURE 5.15: Theoretical model for reflection coefficient using the Debye relaxation model vs. simulation for a 5 mm water layer with air as backing material.

Case 1. Debye vs Simulation. Using the Debye relaxation model with the same parameters for water as seen in table 3.6 a comparison vs. the theoretical model and the simulation can be done. The response is shown in figure 5.15. From the response, we see that the theoretical model is inaccurate compared to the simulation and that the number resonances and the amplitude do not match.

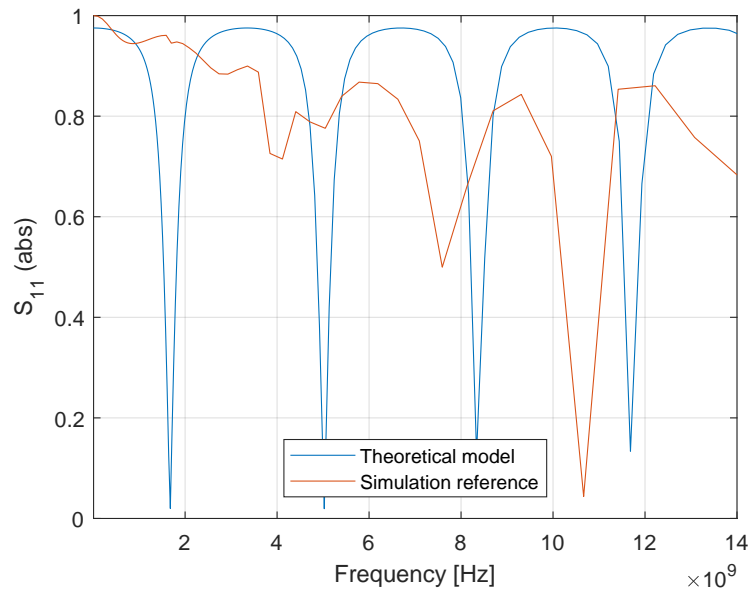


FIGURE 5.16: Theoretical model for reflection coefficient vs. simulation for a 5 mm loss-less water layer with air as backing material.

Case 2 - High permittivity, loss-less medium. Using a simpler model i.e., keeping the permittivity constant. In this case, loss-less water is used with a complex permittivity, where the real part is 80.21, and the imaginary part is 0. This material is purely theoretical but gives a good indication of when the greatest resonances occur. In this case, we see good compliance with the simulations, as seen in figure 5.16.

Case 3 - Low Permittivity, loss-less medium. In this case we evaluate the response of the theoretical model when the layer is a low permittivity loss-less material. Here the layer has a complex permittivity of 20 and air as backing material. The resonances occur less frequently than with a high permittivity material and is less in compliance with the simulations, as seen in figure 5.17.

Case 4 - High permittivity with loss. In this case, the layer has a complex permittivity of $80.21 - i20$. Here we see a good compliance in terms of number of resonances occurring and in similarity between the theoretical model and simulated model, as seen in figure 5.18.

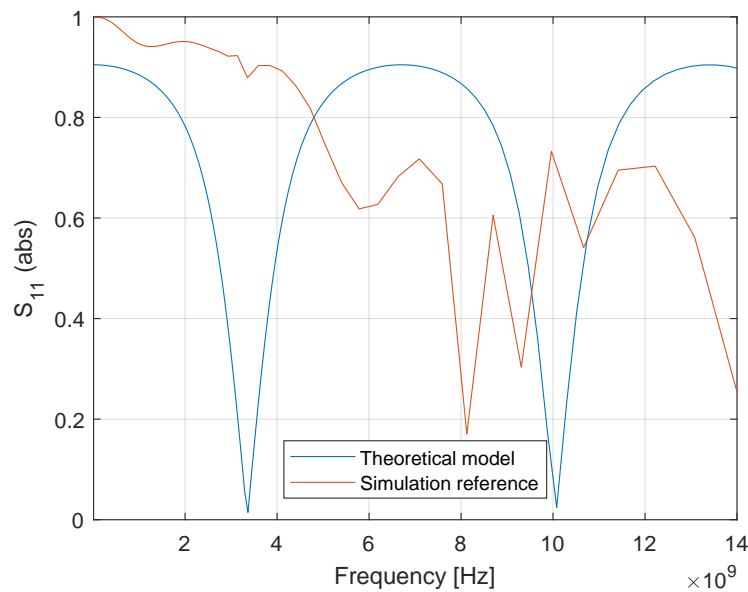


FIGURE 5.17: Theoretical model for reflection coefficient vs. simulation for a 5 mm loss-less medium layer with a complex permittivity of 20, and with air as backing material.

Case 5 - Low permittivity with loss. In this case, the layer has a complex permittivity of $20 - i5$, and as expected while evaluating the different cases, the amplitude is reduced due to the imaginary part of the complex permittivity, and the number of resonances is reduced to the real part of the complex permittivity, as shown in figure 5.19.

Conclusion - The theoretical model shows that we have increasing resonances occurring, the larger the real part of the complex permittivity is. The theoretical model fails to be accurate for complex models like the Debye model, but it proved accurate enough as a "rule of thumb" that can be used to estimate how the reflection coefficient will behave for a given layer, backing material, and depth. Since FE-modeling is a time-consuming task, the model can work as a guideline before conducting a simulation. It also proved that the ideal material for resonances is a high permittivity loss-less material. The main reason for the theoretical model not being accurate is that it is generic and does not consider the probe dimensions and it assumes that we are in the far-field region of the probe propagating in free space. Whereas in the simulation, the near-field where the E and B field is more complex is considered, along with the fact that the radiation from the probe changes with frequency and permittivity.

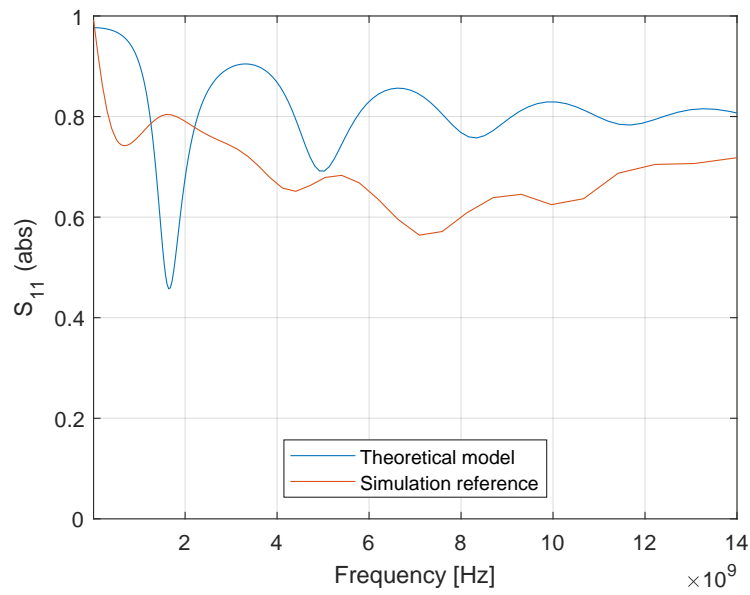


FIGURE 5.18: Theoretical model for reflection coefficient vs. simulation for a 5 mm loss-less layer with a complex permittivity of $80.21 - i20$, and with air as backing material.

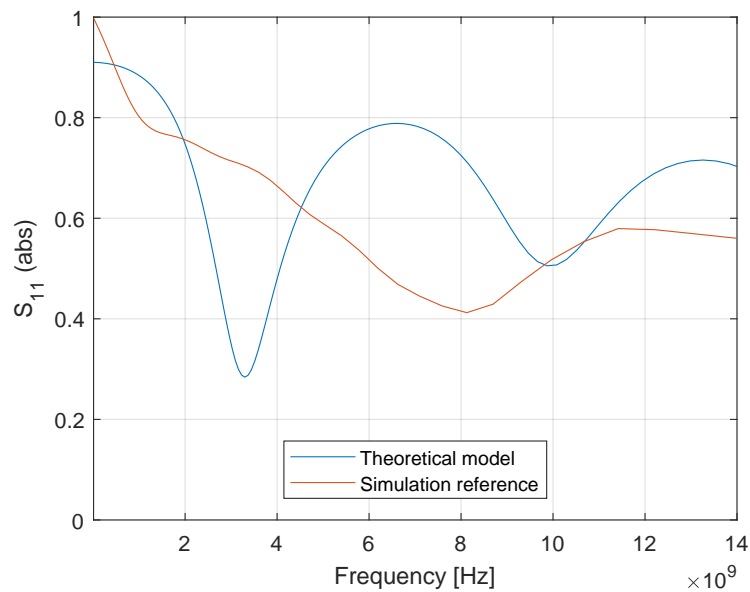


FIGURE 5.19: Theoretical model for reflection coefficient vs. simulation for a 5 mm layer with a permittivity of $\epsilon^* = 20 - i5$, and with air as backing material.

5.3 Permittivity and depth limitations

From the previous section, we saw that the resonances that occur are heavily dependent on the complex permittivity, layer thickness, and frequency for the given probe. It has been shown that the resonances are beneficial and provides increased accuracy especially when it comes to estimating the layer thicknesses. It is therefore helpful to map when the resonances occur for a given permittivity and layer thickness by using the COMSOL model described in chapter 3, so the use-full range of the probe can be determined. The focus in this section has been on thin layers from 0.1 mm to 5 mm thicknesses done in 0.1 mm incremental steps and material and backing material shown in table 5.2. All the materials in this table are loss-less i.e., the complex permittivity does not have an imaginary part. The reflection coefficient from the resulting simulation matrix has been transformed to permittivity using BCP and by using air, ethanol, and water as calibration fluids.

TABLE 5.2: Layer and backing material for simulations to map the the use-full range of the probe

Layer material	$\epsilon^* = 10$	$\epsilon^* = 20$	$\epsilon^* = 30$	$\epsilon^* = 40$	$\epsilon^* = 50$	$\epsilon^* = 60$	$\epsilon^* = 70$	$\epsilon^* = 80$
Backing Material	Air	Air	Air	Air	Air	Air	Air	Air

If we now look at a specific case of a simulation matrix for layers consisting of $\epsilon^* = 10$ with air as backing material, where the y -axis is the span of layer thicknesses from 0.1 to 5 mm, the x -axis is the frequency range of the simulations, and the error is interpreted as amplitude with respect to the xy -plane. In this case the error is given as a relative error in how much the simulated complex permittivity deviates from the response at the lowest frequency divided by the absolute value of the permittivity at the given frequency and layer thickness. This can be summarized by equation (5.9). The main reason for choosing a relative error for this case is that since the layers are thin, the effective measured permittivity will more be affected by the backing layer the smaller the layer thickness is.

$$E_{sim}(i, j) = \frac{\sqrt{(\epsilon'_{sim(1,j)} - \epsilon'_{sim(i,j)})^2 + (\epsilon''_{sim(1,j)} - \epsilon''_{sim(i,j)})^2}}{\sqrt{(\epsilon'_{sim(i,j)})^2 + (\epsilon''_{sim(i,j)})^2}} \quad i, j \in M, N \quad (5.9)$$

Since resonances in the reflection coefficient leads to a significant error in the complex permittivity, a great relative error in the permittivity tells us at the for the given

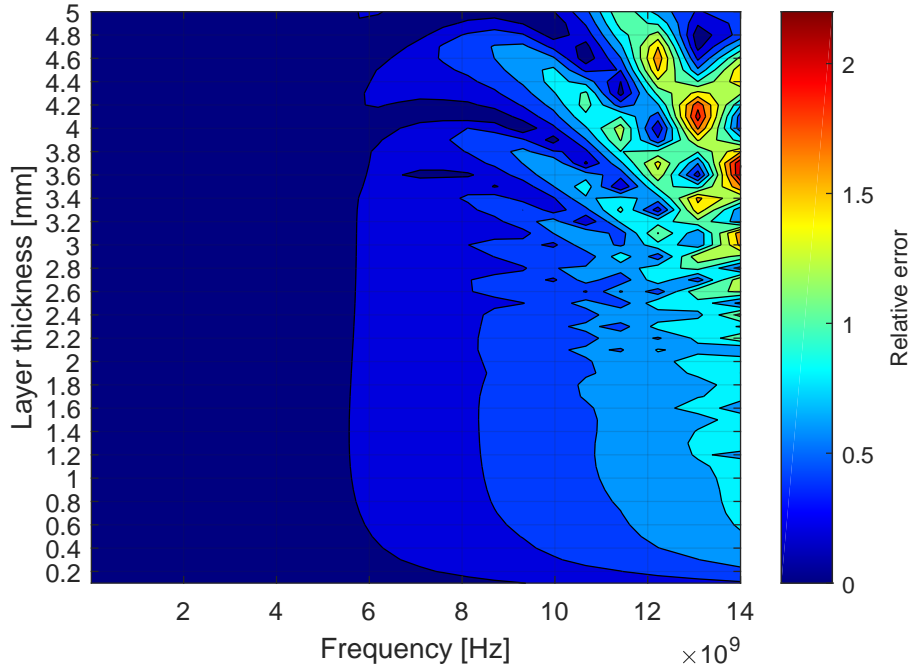


FIGURE 5.20: Contour plot of the relative error, with $\varepsilon^* = 10$ as layer and air as backing material with respect to layer thickness and frequency.

layer thickness and frequency, a resonance has occurred. A contour plot of the specific case is shown in figure 5.20. From the response we see that the resonances occurring happens primarily above 10 GHz, this is in accordance with equation (2.86). For a layer of 3 mm and $\varepsilon' = 10$, (2.86) gives us $f < 7.9 \approx 8$ GHz. We also see the layers and frequencies that result in the greatest relative error, and thus one can estimate before conducting an experiment, the ideal frequency and layer that creates resonances. However, the frequency span is normally limited by the VNA. So the main focus has been on which layers are ideal for a given layer with the properties described in table 5.2. To achieve this, the relative error across all the frequency points has to be summed up and a new relative error function was implemented, given by equation (5.10) and the contour plot is shown in figure 5.21.

$$E_{sim} = \frac{\sum_{i=1}^M \sqrt{(\varepsilon'_{sim(1,j)} - \varepsilon'_{sim(i,j)})^2 + (\varepsilon''_{sim(1,j)} - \varepsilon''_{sim(i,j)})^2}}{\sum_{i=1}^M \sqrt{(\varepsilon'_{sim(i,j)})^2 + (\varepsilon''_{sim(i,j)})^2}} \quad (5.10)$$

From the contour plot, we see that the greater the relative error the greater the amplitude of the resonances. However, a distinct line of where the relative error

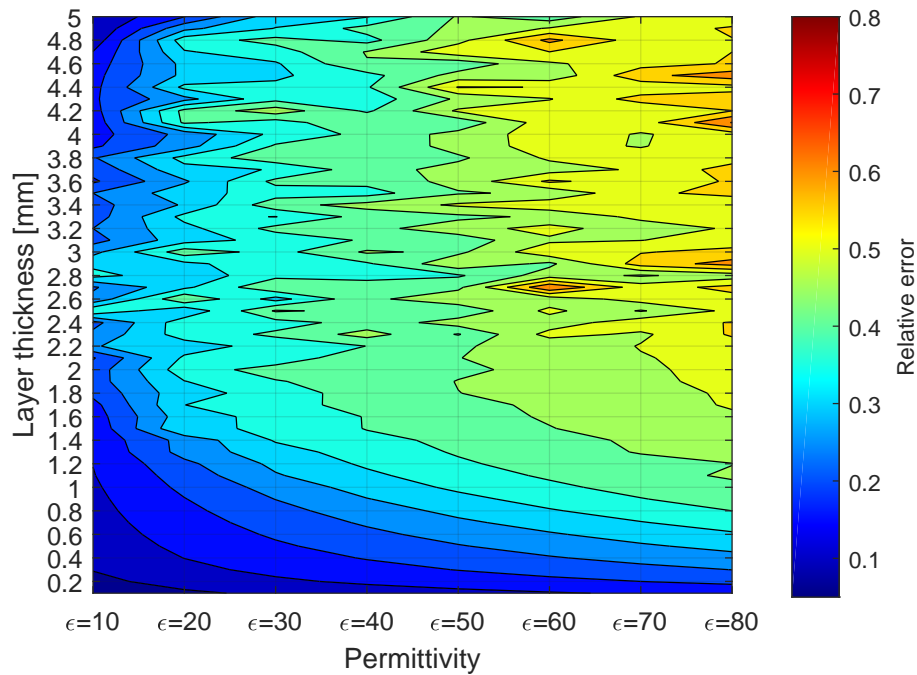


FIGURE 5.21: Contour plot of the relative error, with $\varepsilon^* = 10$ to $\varepsilon^* = 80$ as layer and air as backing material with respect to layer thickness.

results in a significant change in the apparent permittivity has to be established. By evaluating several responses a relative error above > 0.05 results in a good fit, this corresponds to 5% as percentage error. Redrawing the contour plot with changed limits, we get the plot seen in figure 5.22. Here the red area indicates the best layer thicknesses for the given materials that result in a significant change in the apparent permittivity. So a by adding an imaginary part of $5i$ to the layer materials in the table 5.2 a new contour plot can be created, as seen in figure 5.23. From the figure. we see that by introducing a loss factor to the complex permittivity the effective region where the probe creates significant resonances is narrowed down.

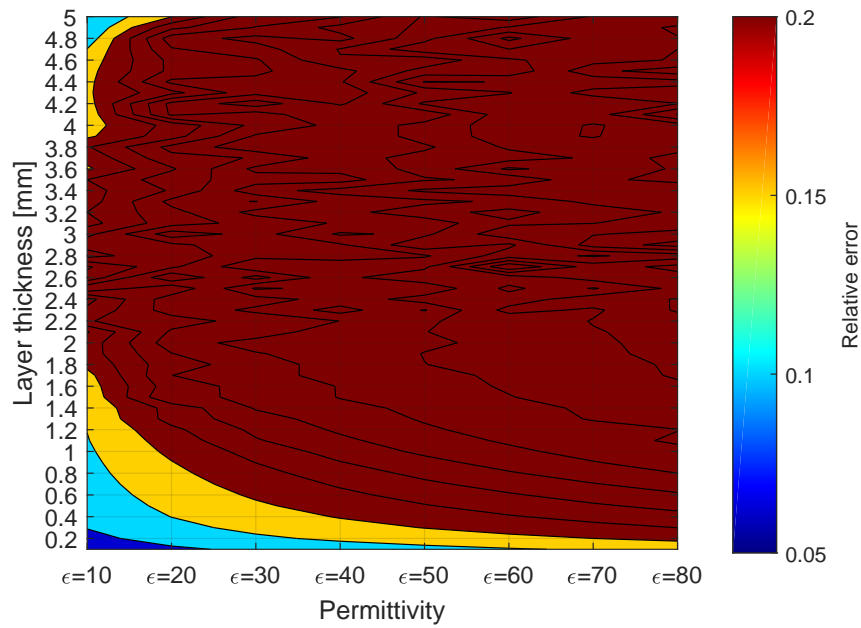


FIGURE 5.22: Contour plot of the relative error with changed limits, with $\epsilon^* = 10$ to $\epsilon^* = 80$ as layer and air as backing material with respect to layer thickness.

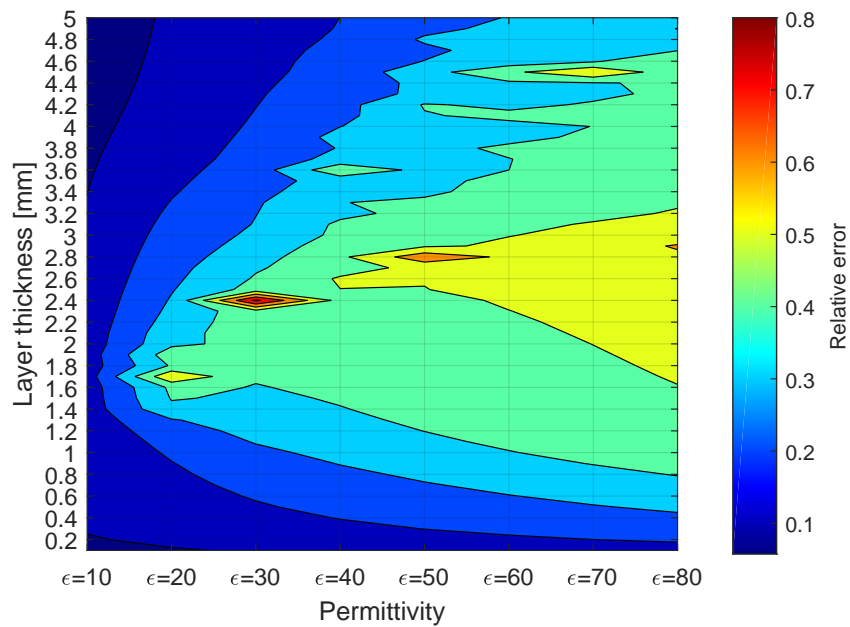


FIGURE 5.23: Contour plot of the relative error, with $\epsilon^* = 10 - 5i$ to $\epsilon^* = 80 - 5i$ as layer and air as backing material with respect to layer thickness.

5.3.1 Low-permittivity layers with water as backing material

By using the method described in section 5.3, we can use this to estimate when resonances will occur for layer materials ranging from 2-to 10 and with water as backing material. The reason for looking at this specific case is that this the most similar to real-life experimental setup. Where the scale building up on the interior of the wall will typically be a low permittivity (solid) material with a mixture of water, oil, and gas flowing within the pipe [3]. Here the backing material, consisting of water was modeled using the Debye relaxation model parameters from table 3.6 and the reflection coefficient was transformed to permittivity using BCP and by using air, ethanol and water as calibration fluids. Normally one would chose calibration fluids close so that of the sample, but since the effective permittivity is heavily influenced by the backing material for thin layers. Meaning that the effective permittivity would be almost equal the backing layer. Therefore, these materials proved optimal as calibration fluids. The contour plot of the relative error is shown in figure 5.24. From

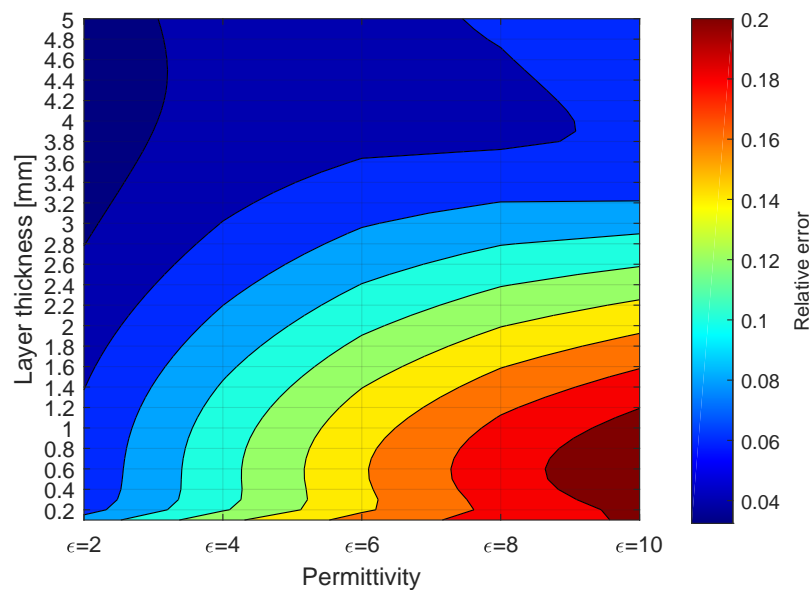


FIGURE 5.24: Contour plot of the relative error, with $\epsilon^* = 2$ to $\epsilon^* = 10$ as layer and water as backing material with respect to layer thickness.

the plot, it can be observed that the relative error increases the higher the permittivity of the layer is, and the preferred response that would generate the greatest amplitude of the resonances would have a permittivity of 10 and a layer thickness of 0.1 to 1.2 mm. The response here is in accordance with the results from section

5.2.2, i.e. the higher the real part of the complex permittivity the greater the amplitude of the resonances. However, it is hard to conduct experiments on solids, since it is difficult to create a well-defined plane surface, air gaps can cause a mismatch between the probe and the sample boundary, and nonhomogeneity of the dielectric can cause problems [44].

5.3.2 Permittivity and depth limitations for ethanol/water mixtures

The method described in section 5.3 proved inaccurate for evaluating when resonances occur simulations based on dispersion models e.g., Debye, Cole-Cole etc. To account for the inaccuracy, a different methodology was created for estimating when resonances occur. Instead of evaluating how the simulated complex permittivity deviates from the response at the lowest frequency. It was in this case evaluated against the effective permittivity of a given layer using the theoretical dielectric model from table 3.6. In other words, the permittivity response caused by comparing the probe the radiating probe against its non-radiating reference value at a given layer. As mentioned in section 2.3.6, a semi-empirical model for estimating the effective permittivity of a sample of a finite thickness was given by equation (2.78). However, this requires that the empirical parameter D is known, which requires curve fitting tools. By introducing a complex gain factor $\tilde{\kappa}$ the effective permittivity of a given layer can be found. The complex gain factor is found by dividing the permittivity of the simulated response ε_{sim} at the lowest frequency of a given layer on the reference permittivity ε_{ref} of the material, i.e. :

$$\tilde{\kappa}(1, j) = \frac{\varepsilon_{sim}(1, j)}{\varepsilon_{ref}} \quad (5.11)$$

Where i the index of the frequency, and j is the layer in the simulation matrix. The resulting vector $\tilde{\kappa}$ can then be used to find the non-radiating effective permittivity ε_{eff} of each layer, given by:

$$\hat{\varepsilon}_{eff}(i, j) = \tilde{\kappa}(1, j) \cdot \varepsilon_{ref}(i, j) \quad (5.12)$$

The method can be explained by evaluating e.g., a 1 mm thick layer consisting of $\chi_e = 0.54$ and with air as backing material, as shown in figure 5.25. Here, the simulated response from the simulation matrix for the given layer is a plotted, along with the theoretical model of $\chi_e = 0.54$ using the values from table 3.6. The effective permittivity of the layer is shifted down from the theoretical model, since thin

layers is influenced by the backing material with a lower permittivity, reducing the effective permittivity of the given layer. $\hat{\epsilon}_{eff}$ will converge against the theoretical model for layers that are considered infinitely thick. The relative error is then cal-

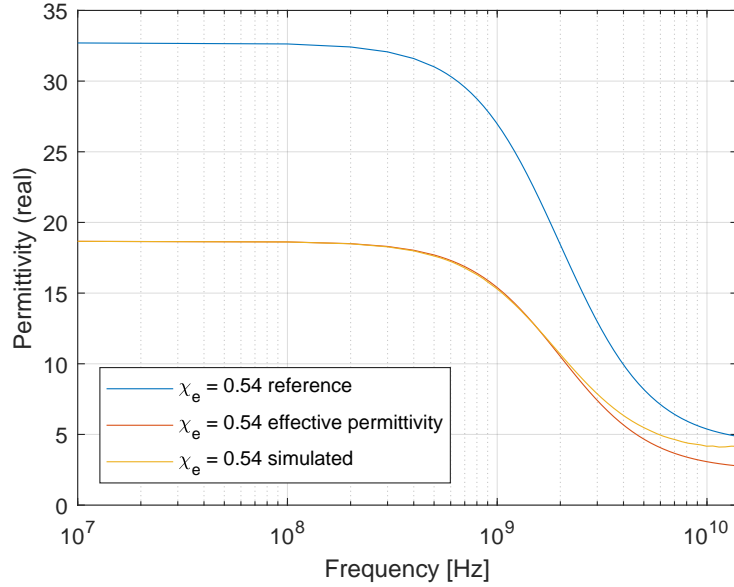


FIGURE 5.25: Reference model, effective and simulated permittivity for a 1 mm thick layer with a molar fraction of $\chi_e = 0.54$, and with air as backing material.

culated by modifying equation (5.10) to find the relative error between the effective complex permittivity and the simulated complex permittivity:

$$\hat{E}_{sim}(i, j) = \frac{\sum_{i=1}^M \sqrt{(\epsilon'_{sim(i,j)} - \hat{\epsilon}'_{eff(i,j)})^2 + (\epsilon''_{sim(i,j)} - \hat{\epsilon}''_{eff(i,j)})^2}}{\sum_{i=1}^M \sqrt{(\hat{\epsilon}'_{eff(i,j)})^2 + (\hat{\epsilon}''_{eff(i,j)})^2}} \quad (5.13)$$

A logarithmic scale was utilized to present the relative error in a contour plot, as shown in figure 5.26. The plot indicates where the greatest resonances occur for a given layer thickness and molar fraction. Which in turn improves the accuracy of the solution when comparing an experimental data versus the simulation matrix. However, there is deviance in the plot for $\chi_e = 0.22$; The plot indicates that the usefull range of layer thicknesses is from 0 to 50 mm. From the experimental data and other simulations, one would expect that the simulated response converges with the theoretical model once the layer thickness is sufficiently large. A plot of 50 mm, $\chi_e = 0.22$ is shown in figure 5.27 and for comparison a plot of 50 mm, water is shown in figure 5.28. Here we see that the water layer converges and the radiation is minimal,

as expected. The deviance can be traced back to when the simulation matrix is converted to permittivity using BCP. The procedure assumes a linear two capacitor model of the probe, and the increasing conductance gives increasing error when being transformed. Also, since the simulation matrix spans over a vast range of permittivities, it is difficult to have calibration fluids with permittivity close to all the samples. This result is of significance, and careful consideration of calibration fluids when transforming the data from S_{11} to ε^* is needed. Ideally, one would split the simulation matrix into segments and use different calibration fluids to avoid this deviance, since different calibration fluids will give different permittivity spectra when transformed from reflection coefficient. Splitting the simulation matrix into two segments and recombining them using water, $\chi_e = 0.22$, $\chi_e = 0.36$, $\chi_e = 0.54$ and $\chi_e = 0.76$ as calibration fluids yielded the corrected response shown in figure 5.29. The corrected response proved better for $\chi_e = 0.22$, but a problem for $\chi_e = 0.54$. Although there is a small deviance for $\chi_e = 0.54$, the correct response is more accurate compared to the uncorrected response.

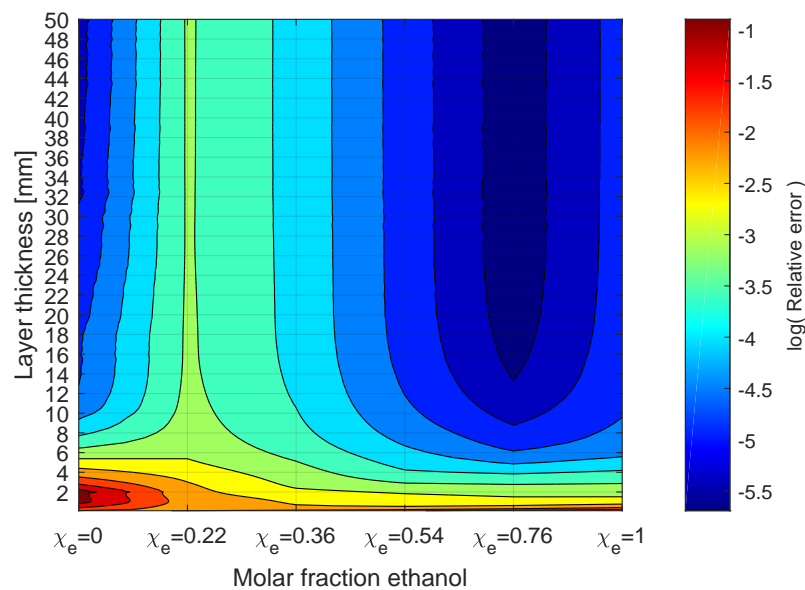


FIGURE 5.26: Contour plot of the relative error, with different mole fractions of ethanol/water mixtures as layer and air as backing material with respect to layer thickness.

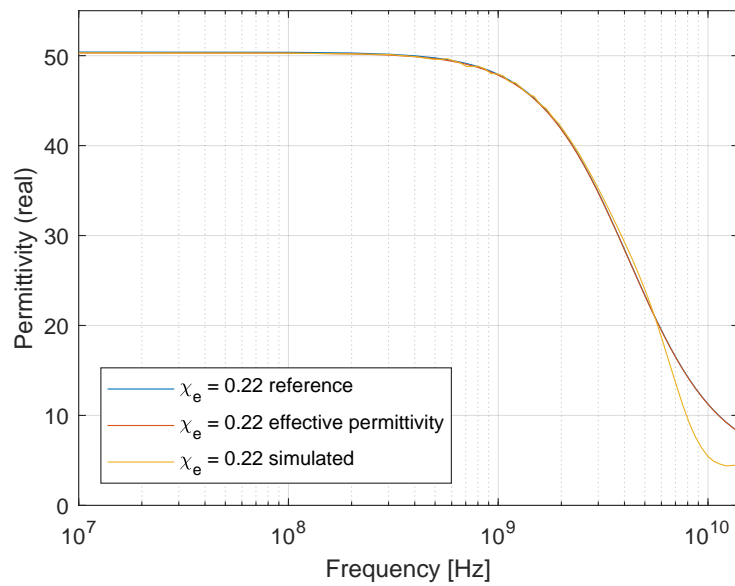


FIGURE 5.27: Reference model, effective, and simulated permittivity for a 50 mm thick layer with a molar fraction of $\chi_e = 0.22$, and with air as backing material.

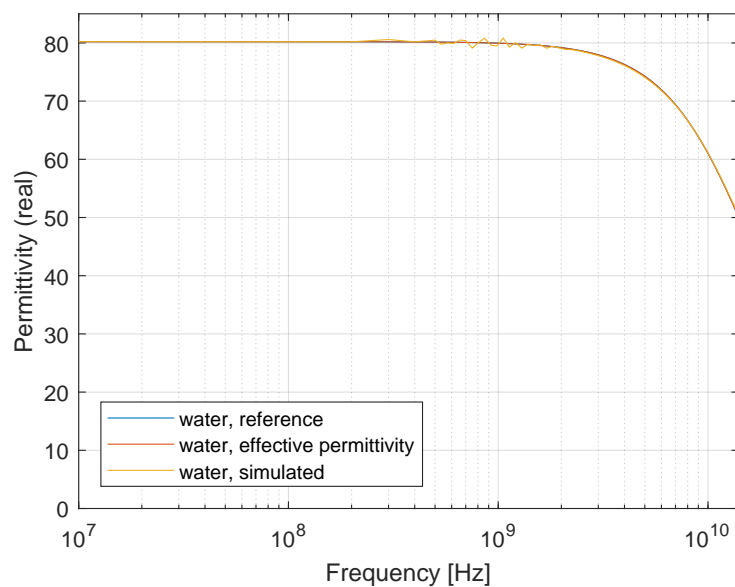


FIGURE 5.28: Reference model, effective, and simulated permittivity for a 50 mm thick layer with water, and with air as backing material.

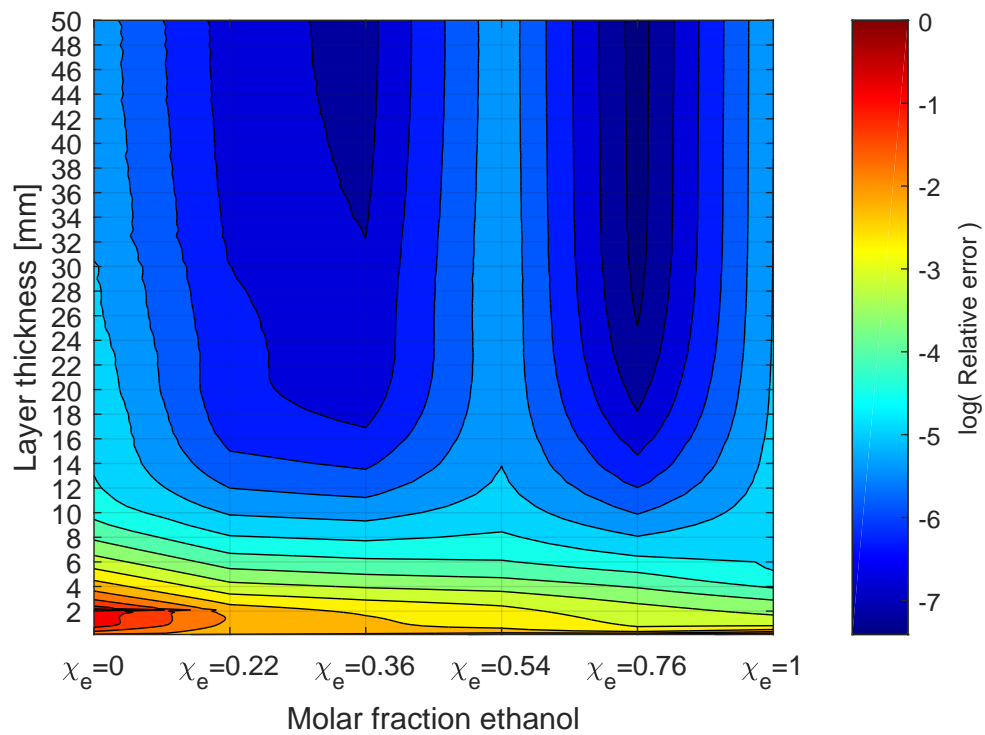


FIGURE 5.29: Corrected contour plot of the relative error, with different mole fractions of ethanol/water mixtures as layer and air as backing material with respect to layer thickness.

Chapter 6

Summary and conclusions

The objective of this thesis was to develop a method for estimating both the thickness and permittivity of layers simultaneously using an open-ended coaxial probe. A two-dimensional axisymmetric model of the open-ended coaxial probe created by CMR was expanded upon to include a new measurement setup, using the simulation software COMSOL Multiphysics. The simulation model spanned the appropriate layers and materials and was verified by measuring and simulating on ethanol/water mixtures layers with known dielectric properties. When the probe radiates at high frequencies, this can result in additional reflections from the probe-sample boundary. The additional reflections lead to artifacts when transformed from reflection coefficient to permittivity using BCP. Typically, this effect will be stronger at some frequencies due to resonance effects. The resonance amplitude and frequency depends on the layer thickness, the permittivity of the layer/backing material and the probe dimensions. When comparing measurement data to the simulations, there are two possible solutions since the frequency points differ. A function was developed that fits the measured frequency points to the simulations using the spline interpolation technique. This was chosen to minimize noise present in the experiment.

The comparison between the measurement and the simulations could be done on the reflection coefficient or on the transformed permittivity. The latter comparison proved most accurate. Utilizing a logarithmic scale of the deviation between the measured spectrum and simulation matrix (equation 5.1), we can estimate the molar fraction of the ethanol/water mixtures and the thickness of the layer. A contour plot was used to display how the measured data compares to the simulated data. The contour plot spans the appropriate thicknesses in the y -direction, the ethanol/water mixtures in the x -direction and the error as amplitudes with respect to the xy -plane.

Usually, resonances present an unwanted measurement error, but they also contain information about the layer thickness. Additionally, the measured spectrum also contains information about the layer permittivity. Hence, open-ended coaxial probes were applicable for combined layer thickness and permittivity measurements, and they increase the accuracy of the solution in the contour plots. We are also able to estimate layers greater than the sensitivity of the probe, shown in figure 5.8. Since the resonances are beneficial, it is necessary to map when they occur. This depends on the complex permittivity, layer thickness, and frequency for the given probe. A theoretical model was used to estimate when the resonances occur, but it proved inaccurate compared to the simulations and should only be used as a "rule of thumb" before simulating. Since resonances in the reflection coefficient lead to a significant error in the complex permittivity. A high relative error in the permittivity indicates a resonance occurrence.

We can determine when resonances occur for a given layer thickness and frequency. By using contour plots to map the amplitude of the relative error with respect to the xy -plane, where x -axis and y -axis represent the frequencies and layer thicknesses respectively. Since the frequencies of the measurement is limited by the VNA, the focus was to map the occurrence of resonances as function of layer thickness and material. Depending on whether the evaluated material had been modeled using a static model or dispersion model for the permittivity, different techniques were utilized, resulting in the contour plots in figure 5.23 and 5.26. By evaluating the materials based on dispersion models, limitations in the BCP was found. The solution was to divide the S_{11} -matrix into segments and use appropriate materials as calibration fluids close to the permittivity of the segment, before recombining. This resulted in the corrected contour plot shown in figure 5.29.

The main conclusion of this work is that an open-ended coaxial probe is applicable for estimating both the thickness and permittivity of layers simultaneously over a limited range. The FEM simulation determines the operating range with regards to permittivity and layer thickness for the probe. A method for estimating permittivity and layer thickness has been developed and verified by measuring on liquids with known dielectric properties. Lastly, resonances present in the measurements were deemed useful, and methods for determining resonance occurrences as a function of frequency, permittivity and layer thickness have been presented.

6.1 Future work

6.1.1 Conductivity and salinity

During the production of a reservoir, the production can vary greatly depending on its age and location. With increasing age, water is often injected into the reservoir to increase recovery of oil and gas. This combination of formation water and injected water will increase the salinity during production. The increased salinity will therefore increase the conductivity of the water [45]. The simulations conducted in this thesis has been on ideal liquids with zero conductivity. From equation (2.28) we see that this influences the imaginary part of the permittivity, which in turn increases the attenuation of the electromagnetic wave. Further investigation is needed on how the salinity affects the measurements, and the simulation matrix should be expanded to include the simulation on liquids with increased conductivity. This will make the method presented in thesis more applicable.

6.1.2 Regarding level steps in contour plots

In some of the plots presented in chapter 5, the level steps are done manually and are fine-tuned to create the optimal contrast ratio in the response. Ideally, this should be an automatic process which sets the level step appropriately depending on the error.

6.1.3 Limitation of the simulations

The simulations require an accurate model of the layer and backing material i.e., the dielectric properties of the materials being simulated must be well known and documented to achieve high accuracy with the experimental data. Further investigation is needed for materials that are more complex and have several relaxation times. Also temperature variations and pressure should be considered, since the permittivity will be directly affected by these conditions.

6.1.4 Other probe geometries

The results discussed in this thesis has been on one probe specifically, another probe with a different geometry and radiating properties should be evaluated and compared against the probe used in this work. Preferably a probe with more radiating properties might yield less of a limitation when it comes to choosing a material and layer thicknesses that causes resonances.

References

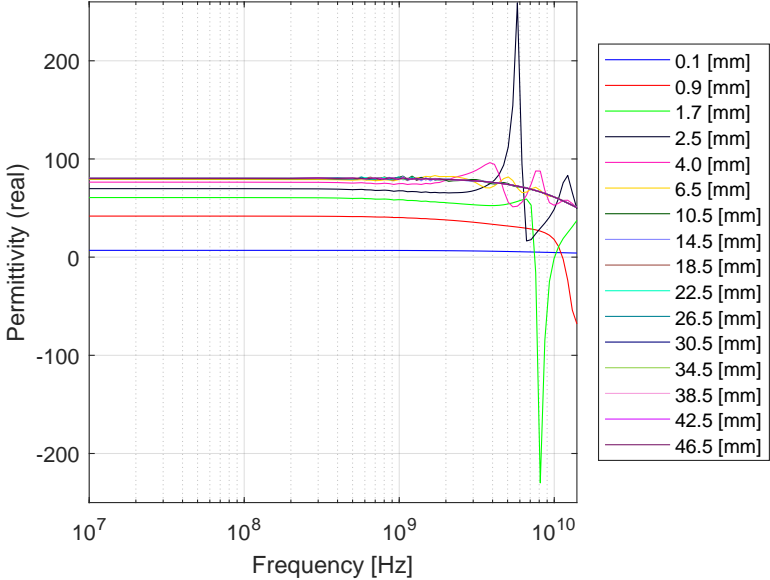
- [1] Kjetil Haukalid and Kjetil Folgerø. "Broad-band permittivity measurements of formation of gas hydrate layers using open-ended coaxial probes". In: *Energy & Fuels* 30.9 (2016), pp. 7196–7205.
- [2] Thorvald Jakobsen and Kjetil Folgerø. "Dielectric measurements of gas hydrate formation in water-in-oil emulsions using open-ended coaxial probes". In: *Measurement Science and Technology* 8.9 (1997), p. 1006.
- [3] Gregory J White and Arthur S Rood. "Radon emanation from NORM-contaminated pipe scale and soil at petroleum industry sites". In: *Journal of environmental radioactivity* 54.3 (2001), pp. 401–413.
- [4] Jacob M. Farrell P. & Brodie G. *Microwave and Radio-Frequency Technologies in Agriculture*. De Gruyter Open., 2016. URL: <https://www.degruyter.com/view/product/466435>.
- [5] Adishesu Nyshadham, Christopher L Sibbald, and Stanislaw S Stuchly. "Permittivity measurements using open-ended sensors and reference liquid calibration—an uncertainty analysis". In: *IEEE Transactions on Microwave Theory and Techniques* 40.2 (1992), pp. 305–314.
- [6] Kjetil Folgerø and Tore Tjomsland. "Permittivity measurement of thin liquid layers using open-ended coaxial probes". In: *Measurement Science and Technology* 7.8 (1996), p. 1164.
- [7] Kjetil Haukalid. "Formation of gas hydrates studied by means of broad-band permittivity measurements". PhD thesis. University of Bergen, 2017.
- [8] Kocbach, Jan Folgerø, Kjetil and Haukalid, Kjetil. "Permittivity measurements of layers". Pat. US20170160069A1. 2017-06-08. URL: <https://patents.google.com/patent/US20170160069A1/en>.
- [9] D. J. Griffiths. *Introduction to Electrodynamics*. 4th ed. Pearson, 2014. ISBN: 989-1-29202-142-3.
- [10] J.B. Hasted. *Aqueous dielectrics*. Studies in chemical physics. Chapman and Hall, 1973.
- [11] *Basics of Measuring the Dielectric Properties of Materials*. Retrieved 28.08.2017. Keysight Technologies, Mar. 2017. URL: <http://literature.cdn.keysight.com/litweb/pdf/5989-2589EN.pdf?id=670519>.

- [12] Neo, C. P. Chen, L.F. Ong, C.K. *Microwave Electronics*. Wiley, 2004. ISBN: 0-470-84492-2.
- [13] Peter Josef William Debye. *Polar molecules*. Chemical Catalog Company, Incorporated, 1929.
- [14] Udo Kaatze. "Complex permittivity of water as a function of frequency and temperature". In: *Journal of Chemical and Engineering Data* 34.4 (1989), pp. 371–374.
- [15] J Vanderschueren and J Gasiot. "Field-induced thermally stimulated currents". In: *Thermally stimulated relaxation in solids* (1979), pp. 135–223.
- [16] Kenneth S Cole and Robert H Cole. "Dispersion and absorption in dielectrics I. Alternating current characteristics". In: *The Journal of chemical physics* 9.4 (1941), pp. 341–351.
- [17] Yuri P Kalmykov et al. "Microscopic models for dielectric relaxation in disordered systems". In: *Physical Review E* 70.4 (2004), p. 041103.
- [18] James H Harlow. *Electric power transformer engineering*. CRC press, 2004.
- [19] *Making Spectrum Measurements with Rohde & Schwarz Network Analyzers*. Rohde & Schwarz. Mar. 2012. URL: https://cdn.rohde-schwarz.com/pws/dl_downloads/dl_application/application_notes/1ez62/1EZ62_0e.pdf.
- [20] Jose E Schutt-Aine and Raj Mittra. "Scattering parameter transient analysis of transmission lines loaded with nonlinear terminations". In: *IEEE Transactions on Microwave Theory and Techniques* 36.3 (1988), pp. 529–536.
- [21] Gregory Gajda and Stanislaw S Stuchly. "An equivalent circuit of an open-ended coaxial line". In: *IEEE transactions on instrumentation and measurement* 32.4 (1983), pp. 506–508.
- [22] Maria A Stuchly and Stanislaw S Stuchly. "Coaxial line reflection methods for measuring dielectric properties of biological substances at radio and microwave frequencies-A review". In: *IEEE Transactions on Instrumentation and Measurement* 29.3 (1980), pp. 176–183.
- [23] Jerzy Krupka and Claude Weil. "Recent advances in metrology for the electromagnetic characterization of materials at microwave frequencies". In: *Microwaves and Radar, 1998. MIKON'98., 12th International Conference on*. Vol. 4. IEEE. 1998, pp. 243–253.
- [24] Kjetil Folgerø. "Bilinear calibration of coaxial transmission/reflection cells for permittivity measurement of low-loss liquids". In: *Measurement Science and Technology* 7.9 (1996), p. 1260.
- [25] Kjetil Folgeroe. "Coaxial sensors for broad-band complex permittivity measurements of petroleum fluids". PhD thesis. University of Bergen, 1996.

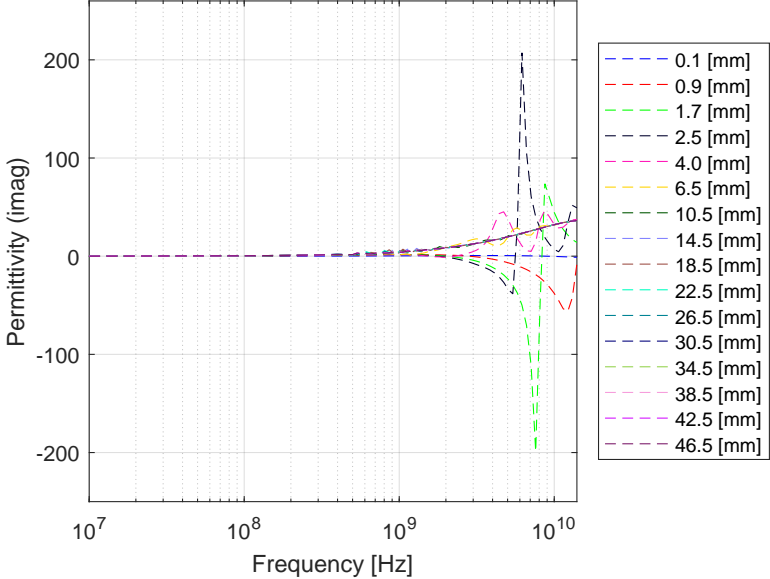
- [26] Jim Fitzpatrick. "Error models for systems measurement". In: *Microwave Journal* 21.5 (1978), pp. 63–66.
- [27] Erik Meijering. "A chronology of interpolation: From ancient astronomy to modern signal and image processing". In: *Proceedings of the IEEE* 90.3 (2002), pp. 319–342.
- [28] Siqi Fan, Katie Staebell, and Devendrá Misra. "Static analysis of an open-ended coaxial line terminated by layered media". In: *IEEE transactions on instrumentation and measurement* 39.2 (1990), pp. 435–437.
- [29] Kun-ming Liao et al. "An Accurate Equivalent Circuit Method of Open Ended Coaxial Probe for Measuring the Permittivity of Materials". In: *Electrical Power Systems and Computers* (2011), pp. 779–784.
- [30] Constantine A Ballanis. "Antenna theory analysis and design". In: *John Willey and Son's Inc., New York* (1997).
- [31] *Finite Element Analysis (FEA) Software*. Retrieved 18.09.2017. COMSOL Multiphysics., 2017. URL: <https://www.comsol.com/multiphysics/fea-software>.
- [32] BM Azizur Rahman and Arti Agrawal. *Finite element modeling methods for photonics*. Artech House, 2013.
- [33] Jean-Pierre Berenger. "A perfectly matched layer for the absorption of electromagnetic waves". In: *Journal of computational physics* 114.2 (1994), pp. 185–200.
- [34] David M Pozar. *Microwave engineering*. John Wiley & Sons, 2009.
- [35] *Using Perfectly Matched Layers and Scattering Boundary Conditions for Wave Electromagnetics Problems*. Retrieved 21.09.2017. COMSOL Multiphysics", 2017. URL: <https://www.comsol.com/blogs/using-perfectly-matched-layers-and-scattering-boundary-conditions-for-wave-electromagnetics-problems/>.
- [36] A Mohsen. "On the impedance boundary condition". In: *Applied Mathematical Modelling* 6.5 (1982), pp. 405–407.
- [37] Gui-Rong Liu and Siu Sin Quek. *The finite element method: a practical course*. Butterworth-Heinemann, 2013.
- [38] *What does degrees of freedom (DOFs) mean in COMSOL Multiphysics?* Retrieved 23.09.2017. COMSOL Multiphysics, 2017. URL: <https://www.comsol.com/support/knowledgebase/875/>.
- [39] *Introduction to Efficiently Modeling Antennas in COMSOL Multiphysics*. Retrieved 18.10.2017. COMSOL Multiphysics, 2017. URL: <https://www.comsol.com/blogs/introduction-to-efficiently-modeling-antennas-in-comsol-multiphysics/>.

-
- [40] William M Haynes. *CRC handbook of chemistry and physics*. CRC press, 2014.
- [41] P Petong, R Pottel, and U Kaatze. “Water- ethanol mixtures at different compositions and temperatures. A dielectric relaxation study”. In: *The Journal of Physical Chemistry A* 104.32 (2000), pp. 7420–7428.
- [42] *Vector Network Analyzer Calibration*. Retrieved 16.11.2017. National Instruments, Jan. 2013. URL: <http://www.ni.com/tutorial/14114/en/>.
- [43] Haukalid, Kjetil Folgerø, Kjetil Kocbach, Jan and Soto Peterson, Andreas. “Combined thickness and permittivity measurement of thin layers with open-ended coaxial probes”. In: *The 12th International Conference on Electromagnetic Wave Interaction with Water and Moist Substances, 2018 - ISEMA 2018*.
- [44] SO Nelson and PG Bartley. “Open-ended coaxial probe permittivity measurements on pulverized materials”. In: *Instrumentation and Measurement Technology Conference, 1997. IMTC/97. Proceedings. Sensing, Processing, Networking., IEEE*. Vol. 1. IEEE. 1997, pp. 653–657.
- [45] R Thorn, GA Johansen, and BT Hjertaker. “Three-phase flow measurement in the petroleum industry”. In: *Measurement Science and Technology* 24.1 (2012), p. 012003.

Due to a large number of responses in the simulation matrix, only a selected responses are shown here for each material. The layer chosen are indicated in the legend of each plot.

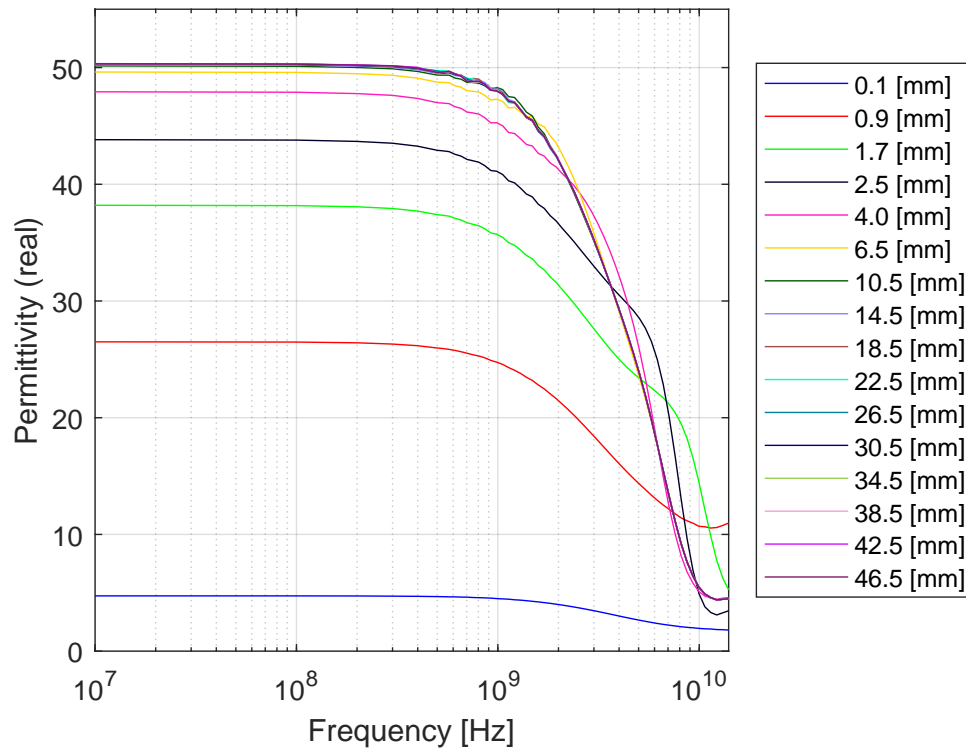


(a) Real part of permittivity

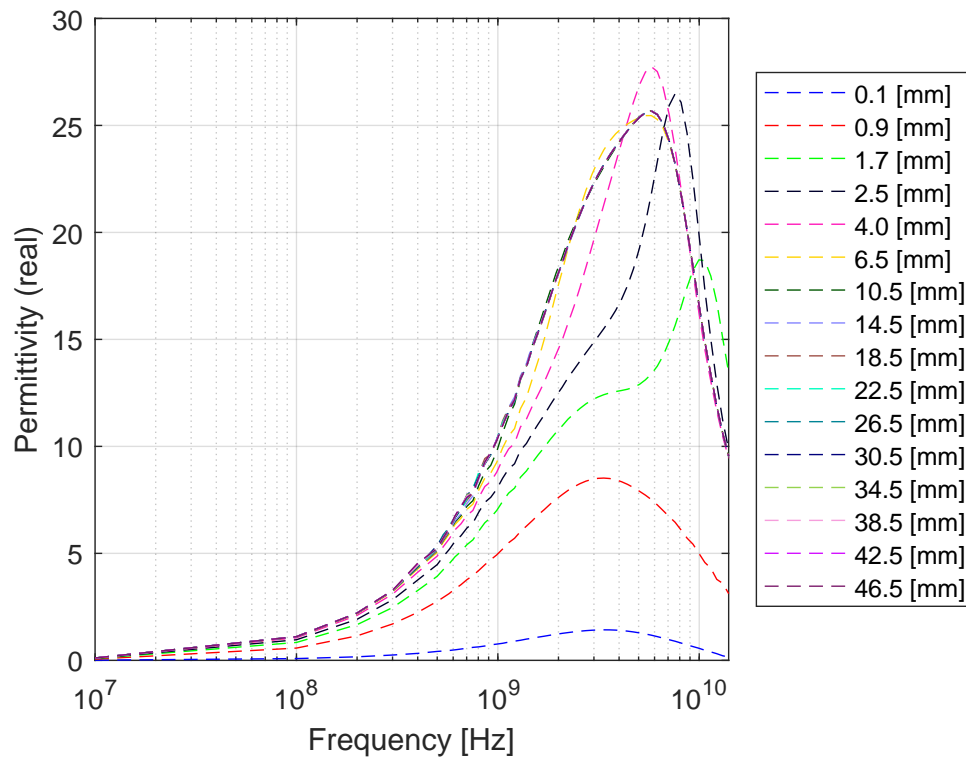


(b) Imaginary part of permittivity

FIGURE A.1: Real and imaginary permittivity of simulated ethanol/water mixture with mole fraction $\chi_e = 0$ and air as backing material

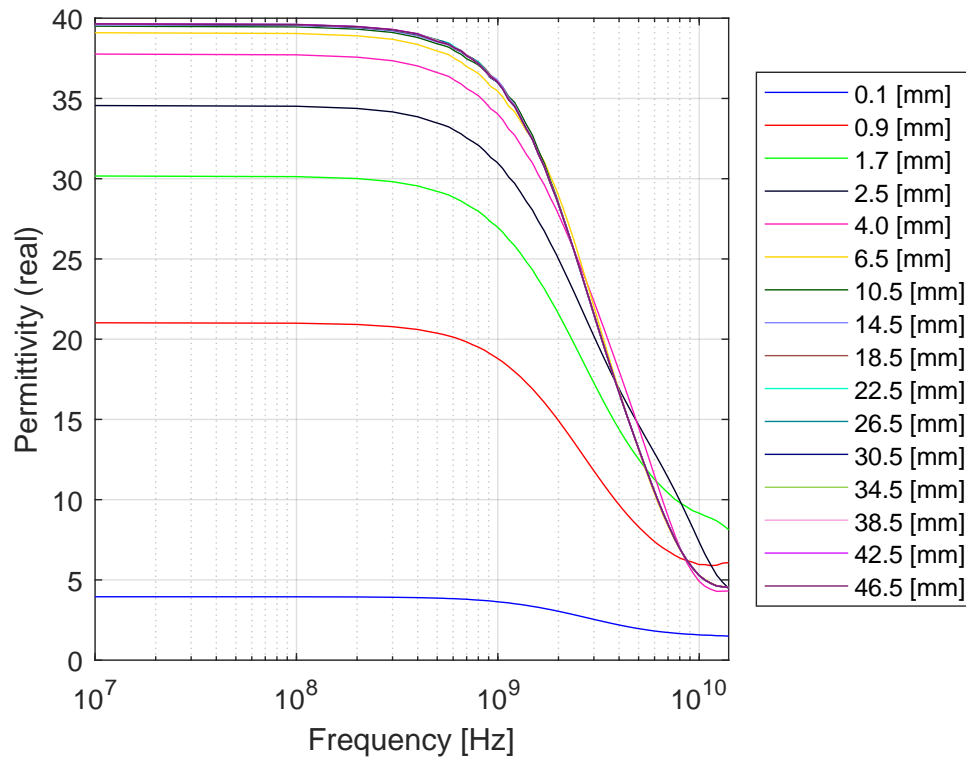


(a) Real part of permittivity

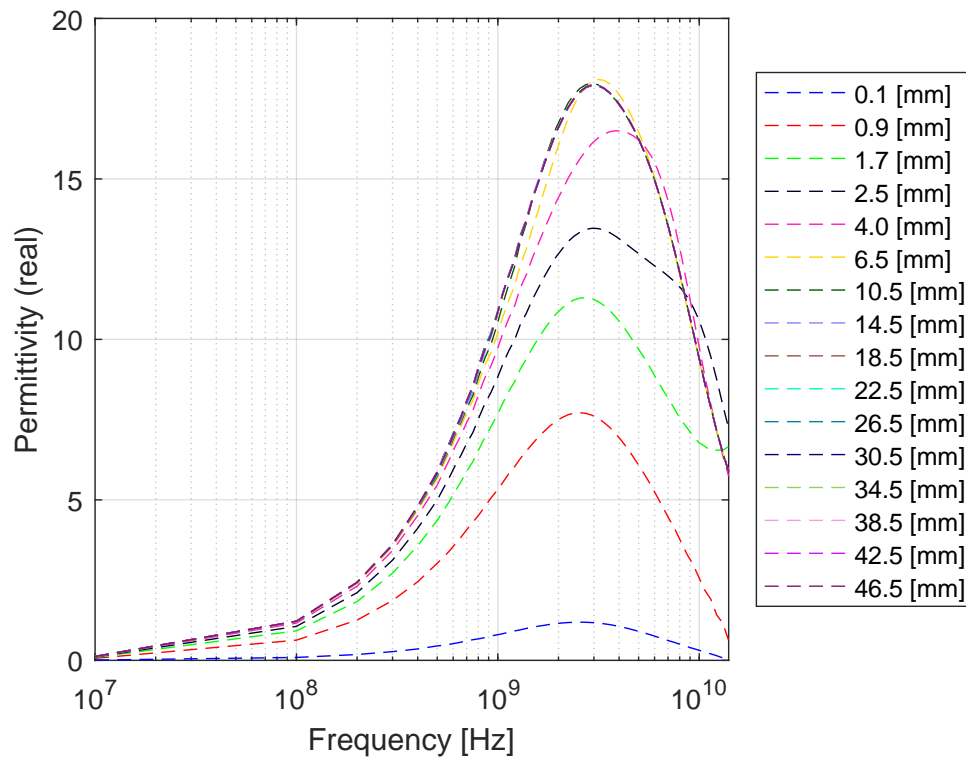


(b) Imaginary part of permittivity

FIGURE A.2: Real and imaginary permittivity of simulated ethanol/water mixture with mole fraction $\chi_e = 0.22$ and air as backing material

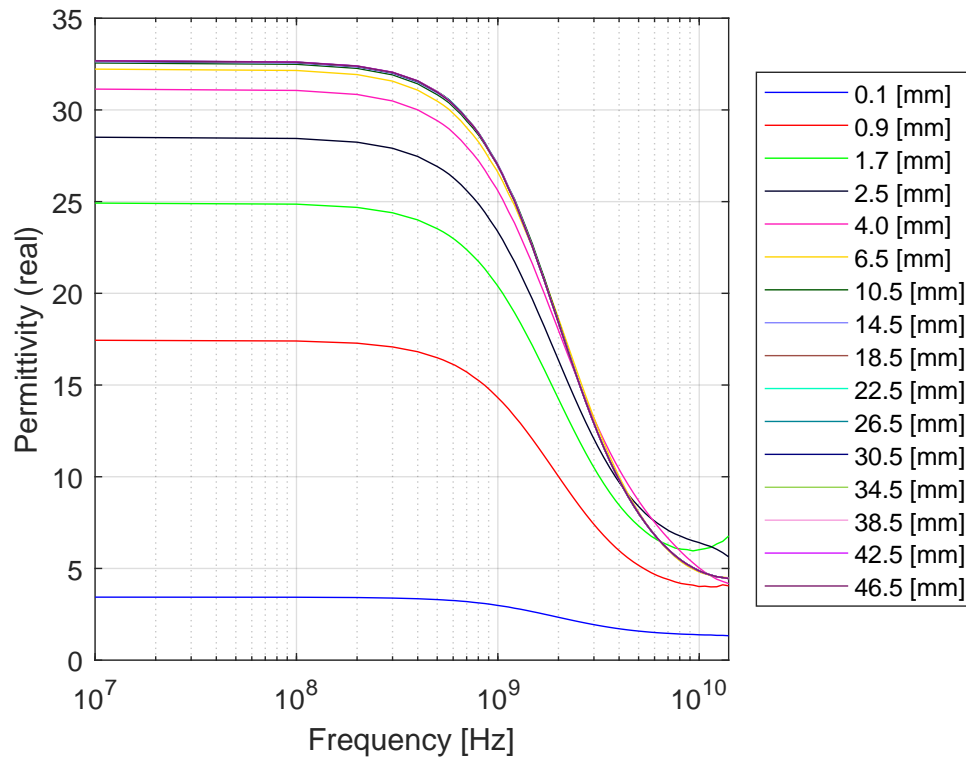


(a) Real part of permittivity

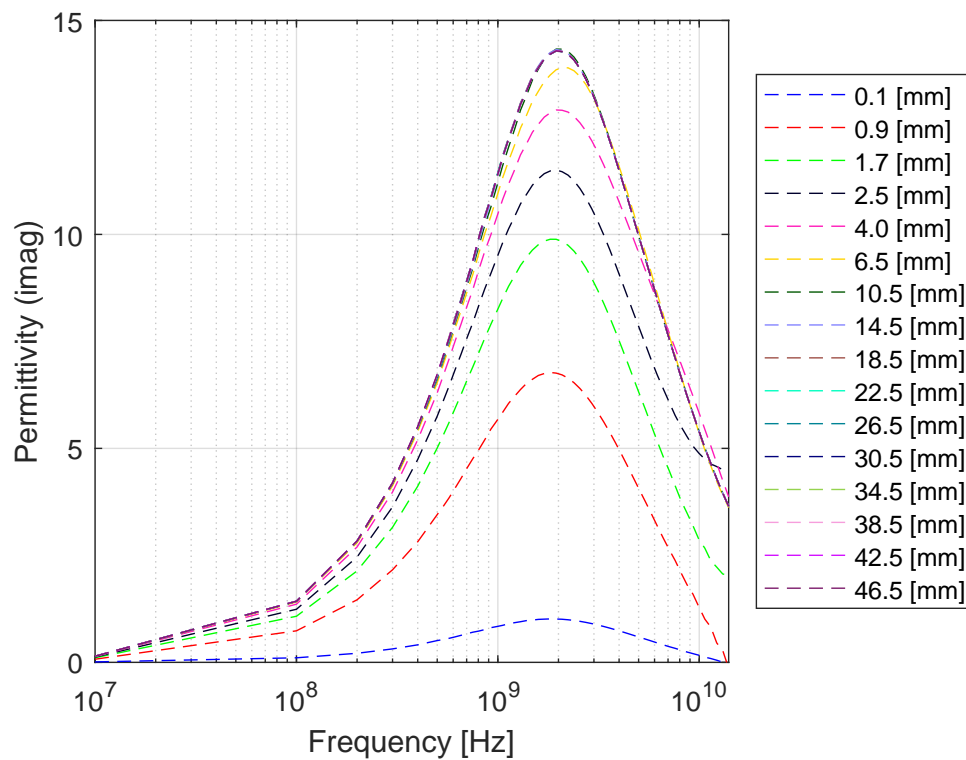


(b) Imaginary part of permittivity

FIGURE A.3: Real and imaginary permittivity of simulated ethanol/water mixture with mole fraction $\chi_e = 0.36$ and air as backing material

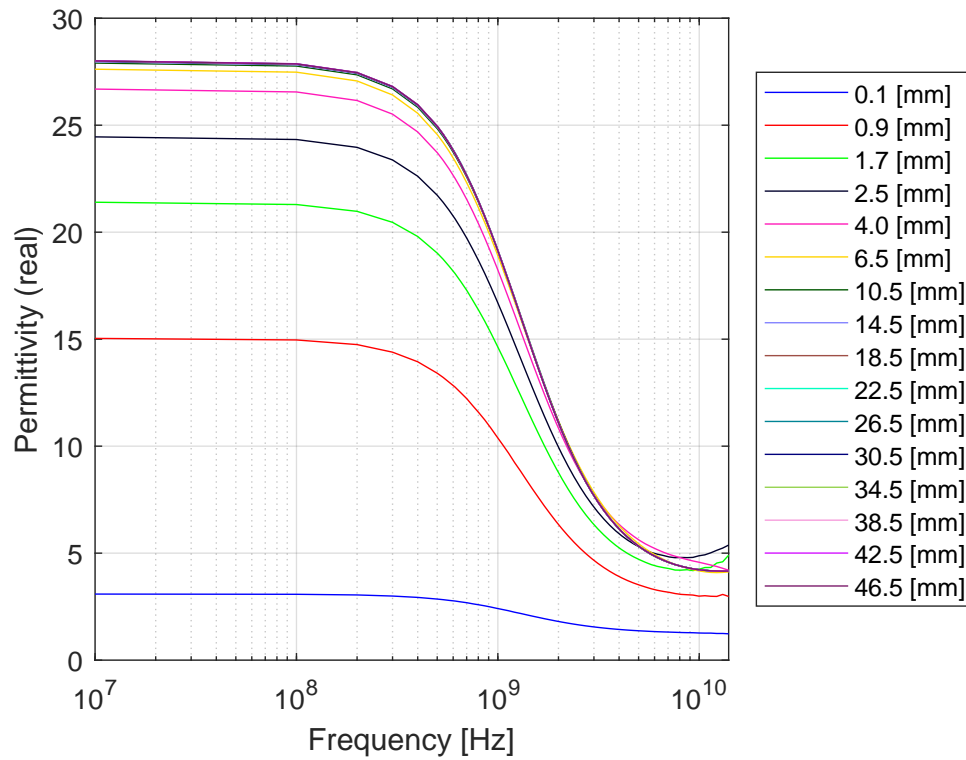


(a) Real part of permittivity

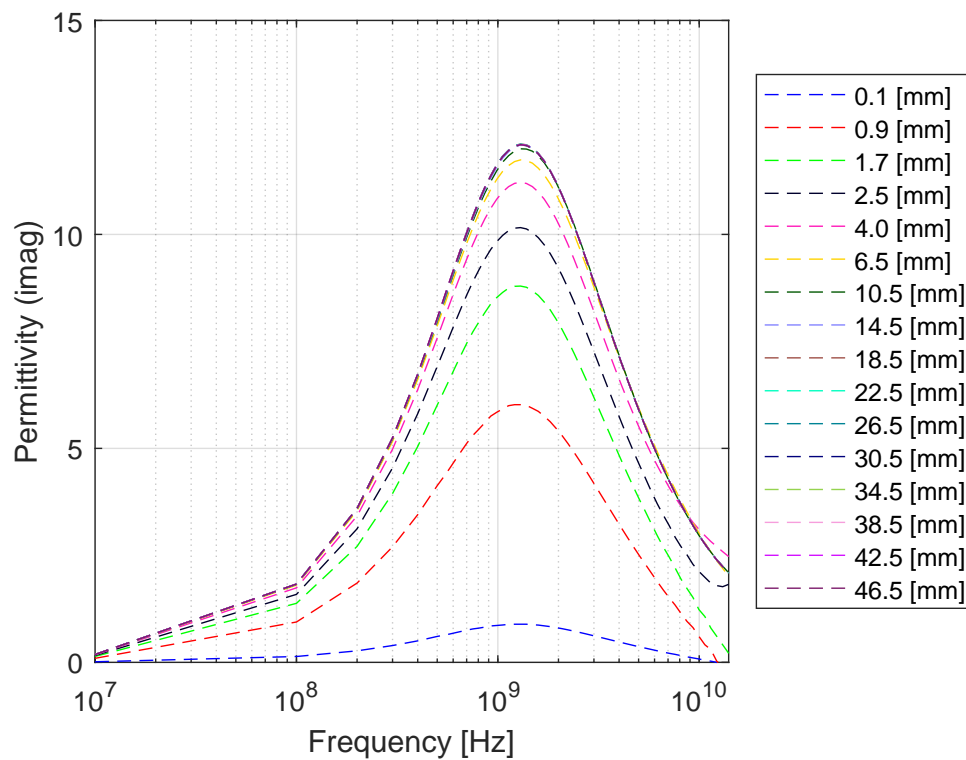


(b) Imaginary part of permittivity

FIGURE A.4: Real and imaginary permittivity of simulated ethanol/water mixture with mole fraction $\chi_e = 0.54$ and air as backing material

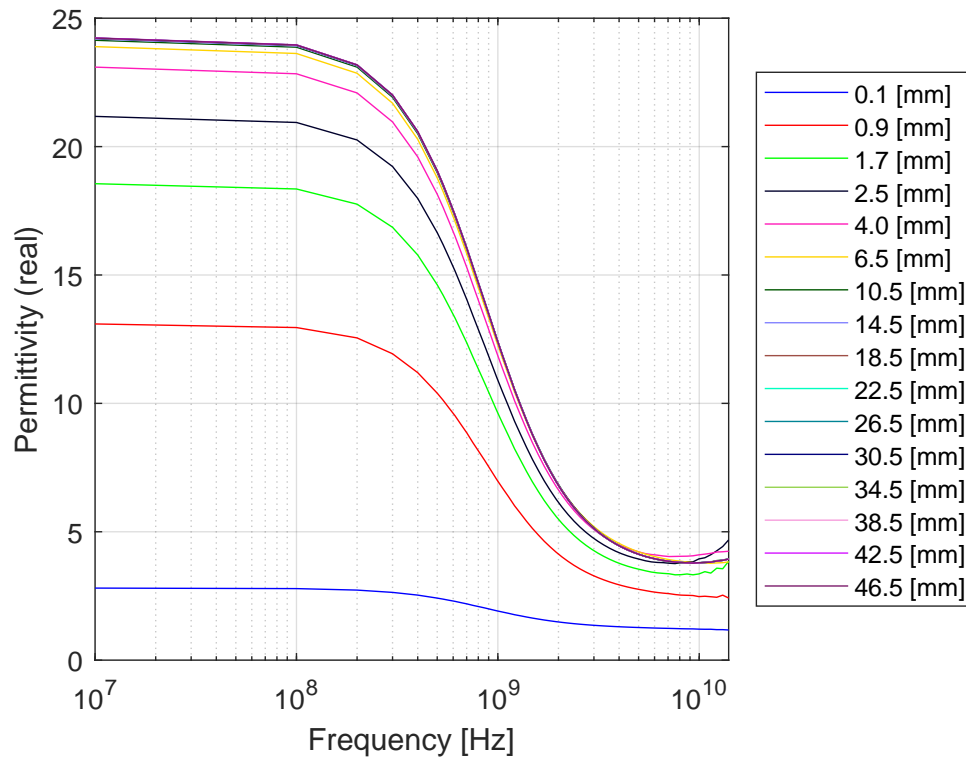


(a) Real part of permittivity

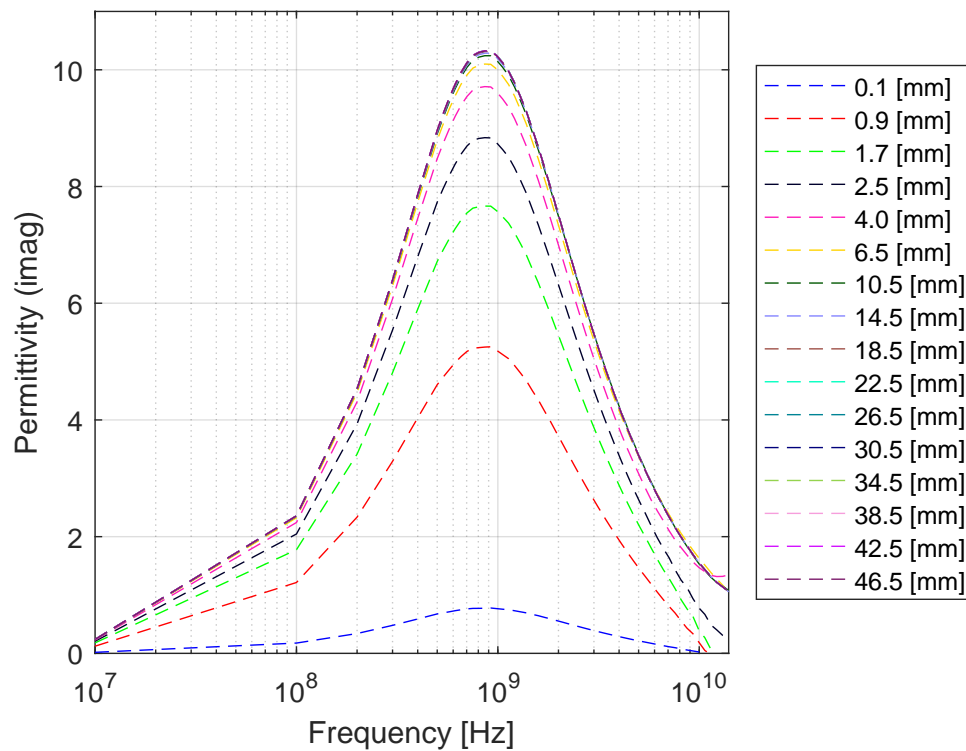


(b) Imaginary part of permittivity

FIGURE A.5: Real and imaginary permittivity of simulated ethanol/water mixture with mole fraction $\chi_e = 0.76$ and air as backing material



(a) Real part of permittivity



(b) Imaginary part of permittivity

FIGURE A.6: Real and imaginary permittivity of simulated ethanol/water mixture with mole fraction $\chi_e = 1.0$ and air as backing material

Appendix B: Paper

A paper accepted for presentation at the The 12th International Conference on Electromagnetic Wave Interaction with Water and Moist Substances (ISEMA).

Combined thickness and permittivity measurement of thin layers with open-ended coaxial probes

Kjetil Folgerø, Kjetil Haukalid and Jan Kocbach
Christian Michelsen Research AS
Norway
kjetil.folgero@cmr.no

Andreas Soto Peterson
Department of Physics and Technology
University of Bergen
Norway

Abstract— This paper presents a method to measure both the thickness and the permittivity of thin layers simultaneously with an open-ended coaxial probe. This is achieved by comparing complex permittivity measurements with finite element (FEM) simulations of the probe. The method necessitates a priori knowledge of the backing material permittivity and the frequency variation of the layer permittivity. A finite element model of the probe is made in the FEM simulation software Comsol Multiphysics, and a matrix of simulations spanning the relevant layer thickness and permittivity range is generated. The measured permittivity spectra can then be compared with the simulation matrix to estimate layer thickness and permittivity.

Keywords—open-ended coaxial probe, thickness measurement, finite element

I. INTRODUCTION

Permittivity measurements with the open-ended coaxial probe rely on analyzing the reflection from the probe-sample boundary. For samples thinner than (approximately) the probe outer conductor radius, the measured effective permittivity will be a function of the permittivity of the sample and the backing material, sample thickness and probe dimensions [1]. The open-ended coaxial probe is known to become radiating at high frequencies (when the probe dimensions are comparable to the wavelength in the material under test). When measuring on samples with finite thickness, this may result in additional reflections from the sample-backing boundary interfering with the main reflection from the probe-sample boundary. This is illustrated in Fig. 1. In Fig. 2, Comsol Multiphysics has been used to simulate the reflection coefficient for three different water layers: One infinite thick layer and two 5 mm thick layers, where one of the layers is modelled without dielectric loss. For the two thin layers, resonances appear in the simulated reflection coefficient due to the reflections from sample-backing boundary. In real measurements, the dielectric loss will dampen the reflections significantly, causing spectrum similar to the red spectrum in Fig. 2. Nevertheless, if the permittivity calculation model applied assumes an infinite sample thickness, the additional reflections may result in artifacts in the effective (measured) permittivity. Typically, the artifacts will be stronger at some frequencies due to resonance effects. The strength of these resonances and the resonance frequency depend on the sample thickness, the permittivity of

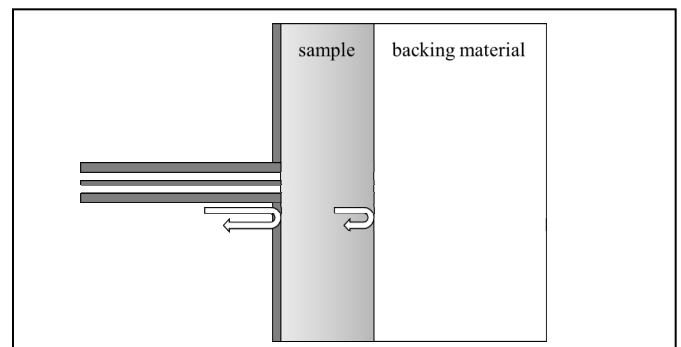


Fig. 1. Illustration of reflections from probe-sample boundary and from sample-backing boundary

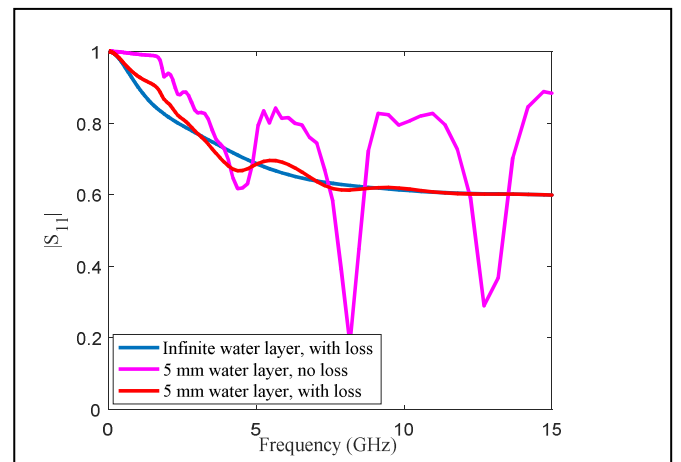


Fig. 2. Simulated reflection coefficient (absolute value) for three water layers. Blue: Infinite thick layer. Red: 5 mm thick layer. Magenta: 5 mm thick layer, with water loss factor set to zero in the simulations.

the sample, the permittivity of backing material and the dimensions of the probe. While such resonances most often represent an unwanted measurement error, they also contain information about the layer thickness and the layer permittivity. Hence, open-ended coaxial probes can be used for combined thickness and permittivity measurements. One possible range of applications is for detection and characterization of deposits inside pipelines, for example gas hydrate deposits in multiphase petroleum transportation [2-3]. The purpose of this

paper is to show that both layer permittivity and layer thickness of relatively thin dielectric layers can be measured with open-ended coaxial probes.

II. METHOD

The method presented in this paper is based on comparison of the measured permittivity spectra (or the measured reflection coefficient) with a matrix of FEM simulations. The FEM simulation software Comsol Multiphysics has been used in this work. A two-dimensional axisymmetric model of the open-ended coaxial probe used in the experiments is used to build the simulation matrix. The simulation matrix have to span the relevant layer thickness and layer permittivity ranges. The method necessitates a priori knowledge of the backing material permittivity and the frequency variation (dispersion frequencies) of the layer permittivity. The resonances occur in the GHz region. The density of simulated frequencies must therefore be relatively high in this region as compared to the MHz region.

After all simulations are completed, the matrix is transformed to the same frequency axis as the measured spectra, using interpolation techniques. The layer thickness and permittivity can then be estimated by direct comparison of a measured spectrum and the simulation matrix. Hence, by finding the layer thickness and layer permittivity whose simulated spectrum gives the best match to the measured spectrum. An iterative approach can also be used, by exploiting that resonance due to probe radiation only occurs at high frequencies:

- A. Extract the measured static permittivity from the measured permittivity spectrum.
- B. Assuming the layer static permittivity to equal the measured static permittivity from A: Find the layer thickness whose corresponding simulated permittivity spectrum gives the best match to the measured permittivity spectrum.
- C. Use the estimated layer thickness from B to update the estimated layer static permittivity.
- D. Assuming the layer static permittivity to equal the estimated value from C: Find the layer thickness whose simulated permittivity spectrum gives the best match to the measured permittivity spectrum.
- E. Repeat C and D until the solution stabilizes.

A. Spanning the layer permittivity

As mentioned above, the method necessitates a priori knowledge of the backing material permittivity and the frequency variation (dispersion frequencies) of the layer permittivity. For many possible applications, the layer will be a mixture of water and one or more materials with very low permittivity and very weak dielectric dispersions, as compared to water. For such applications, the layer permittivity can be reasonably simulated and spanned using a two-phase mixing formula with water and a low permittivity as input. If large temperature variations are expected, the simulation matrix should also span the expected temperature range, since the

permittivity of water shows large variations with temperature in the frequency range where the resonances occur.

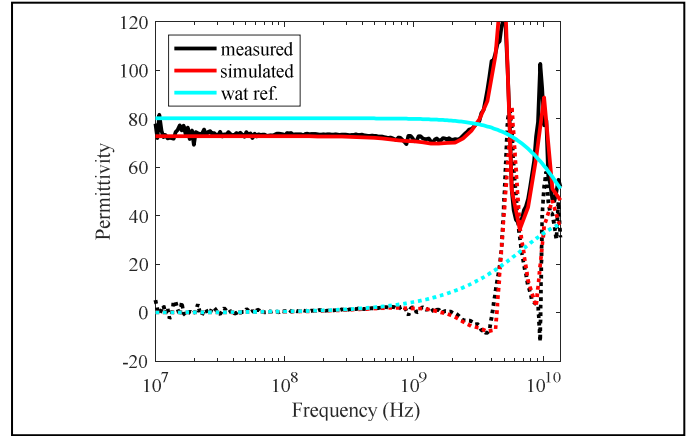


Fig. 3. Comparison of measured and simulated permittivity spectra for 3 mm thick water layer. Liquid water reference spectrum is included. The dielectric constant is plotted with solid lines and the loss factor with dotted lines.

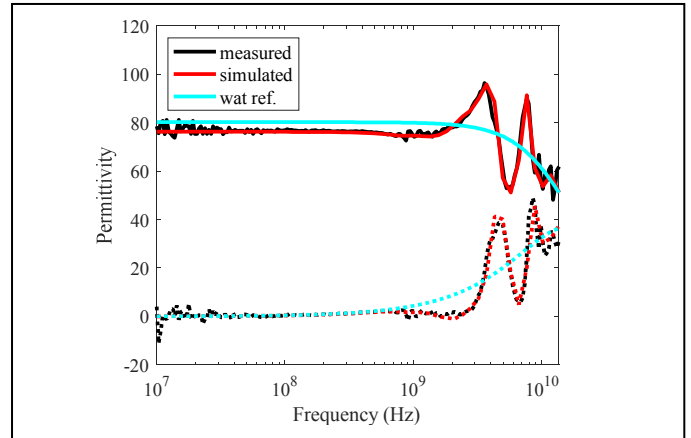


Fig. 4. Comparison of measured and simulated permittivity spectra for 4 mm thick water layer. Liquid water reference spectrum is included. The dielectric constant is plotted with solid lines and the loss factor with dotted lines.

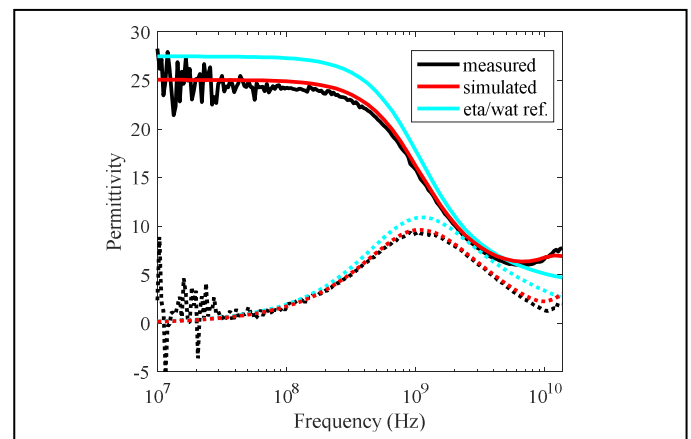


Fig. 5. Comparison of measured and simulated permittivity spectra for 3 mm thick layer with ethanol/water solution. Reference spectrum for the ethanol/water solution is included. The dielectric constant is plotted with solid lines and the loss factor with dotted lines.

B. Layer thickness limitation

The reflection from the sample boundary will decrease in strength with increasing layer thickness as the radiated wave is absorbed. For materials with significant dielectric loss in the GHz region, the radiated waves may be absorbed too quickly to give any resonances in the measured spectra, even for thin layers. Whether or not the resonances are strong enough to be detected for a given layer thickness depends on a number of factors such as the dielectric loss, probe dimensions and the contrast between the permittivity of the layer and the backing material.

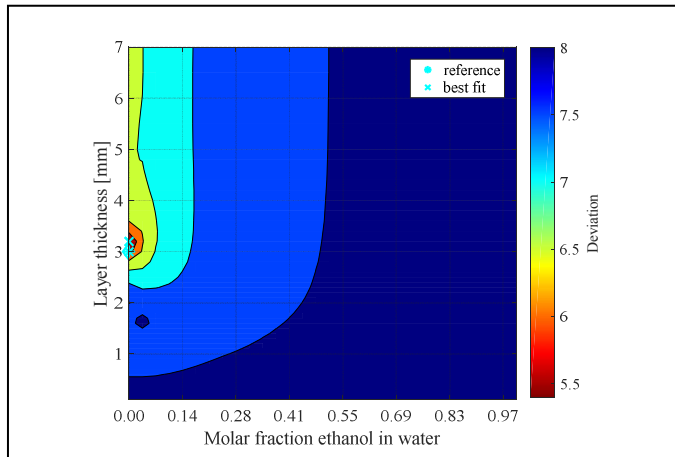


Fig. 6. Contour plot showing deviation between the simulation matrix and the measured spectrum in Fig. 3 (3 mm thick water layer) as function of layer thickness and molar fraction of ethanol in the solution. The cyan cross indicates the best fit, while the cyan asterisk indicates the reference values.

III. RESULTS

Fig. 3 and Fig. 4 compare measured and simulated permittivity spectra for thin water layers (3 and 4 mm thickness, respectively) backed by air. The artifacts in permittivity for the layers are clearly observed. The difference in response between the various layer thicknesses can also clearly be observed. The strength of the resonances decreases and the first resonance moves towards lower frequencies with increasing layer thickness. The simulated spectra in general fit well with the measured spectra. Fig 5 compare measured and simulated permittivity spectra for a 3 mm thick ethanol/water mixture layer (molar fraction of ethanol is 86.5 %). Dielectric relaxation parameters from [4] has been used in the simulations to model the ethanol/water mixture permittivity. Again, the simulated spectrum fits well with the measured spectrum, but the artifacts are much smaller as compared to the 3 mm water layer in Fig. 3. The reason for this is a combination of different factors: The probe radiation increases with increasing sample permittivity, hence less energy is radiated into the ethanol/water layer than into the water layer. The contrast between the layer and the backing material is weaker for the ethanol layer, causing a weaker reflection from the layer/backing boundary.

The inverse problem is to find the permittivity and layer thickness of an unknown sample from the measured

permittivity. A 3mm thick water layer and a 3 mm thick ethanol/water is used as examples, corresponding to the spectra in Fig. 3 and Fig. 5, respectively. Fig. 6 and Fig. 7 show contour plots of the deviation between measured and simulated spectra for the 3 mm water layer and the 3 mm ethanol/water layer, respectively. The contour plots spans layer thickness and molar fraction of ethanol in water. The best fit is close to the actual layer thickness and permittivity for both layers. For the water layer, the red colored area around the best fit (with low deviation from the simulated spectra) is much smaller than for the ethanol/water layer. This is due to weaker artifacts in the 3 mm ethanol/water spectrum as compared to the 3 mm water spectrum, giving lower uncertainty in the estimated layer thickness and permittivity for the water layer.

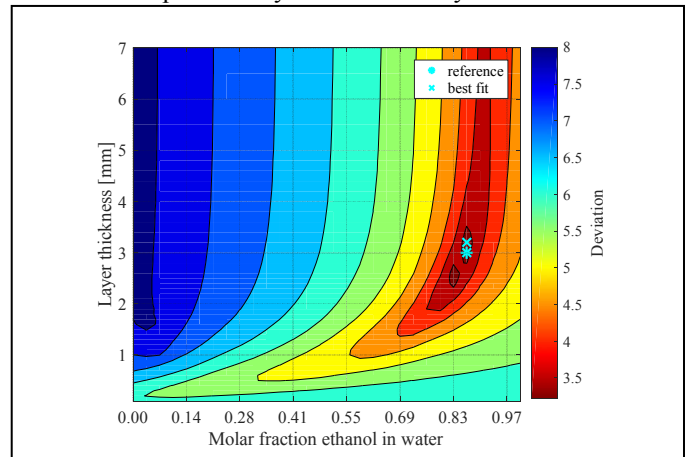


Fig. 7. Contour plot showing deviation between the simulation matrix and the measured spectrum in Fig. 5 (3 mm thick ethanol/water layer) as function of layer thickness and molar fraction of ethanol in the solution. The cyan cross indicates the best fit, while the cyan asterisk indicates the reference values.

IV. CONCLUSION

In this paper, it has been shown that both sample permittivity sample thickness can be estimated by comparing simulated and measured permittivity spectra obtained with an open-ended coaxial probe. The method was verified by measurement and simulations of liquid layers with known properties and thicknesses.

REFERENCES

- [1] K. Folgerø and T. Tjomsland, "Permittivity measurement of thin liquid layers using open-ended coaxial probes," *Measurement Science and Technology*, vol. 7, pp. 1164-1173, 1996.
- [2] K. Haukalid and K. Folgerø, "Broad-band permittivity measurements of formation of gas hydrate layers using open-ended coaxial probes," *Energy Fuels*, vol. 30, pp. 7196-7205, 2016.
- [3] K. Folgerø and K. Haukalid, "Characterization of gas hydrates using dielectric spectroscopy," *Proceedings of the 11th International Conference on Electromagnetic Wave Interaction with Water and Moist Substances*, Florence, Italy, May 23-27, 2016.
- [4] P. Petong, R. Pottel and U. Kaatze, "Water-Ethanol Mixtures at Different Compositions and Temperatures. A Dielectric Relaxation Study," *The Journal of Physical Chemistry A*, vol. 104, pp. 7420-7428, 2000.